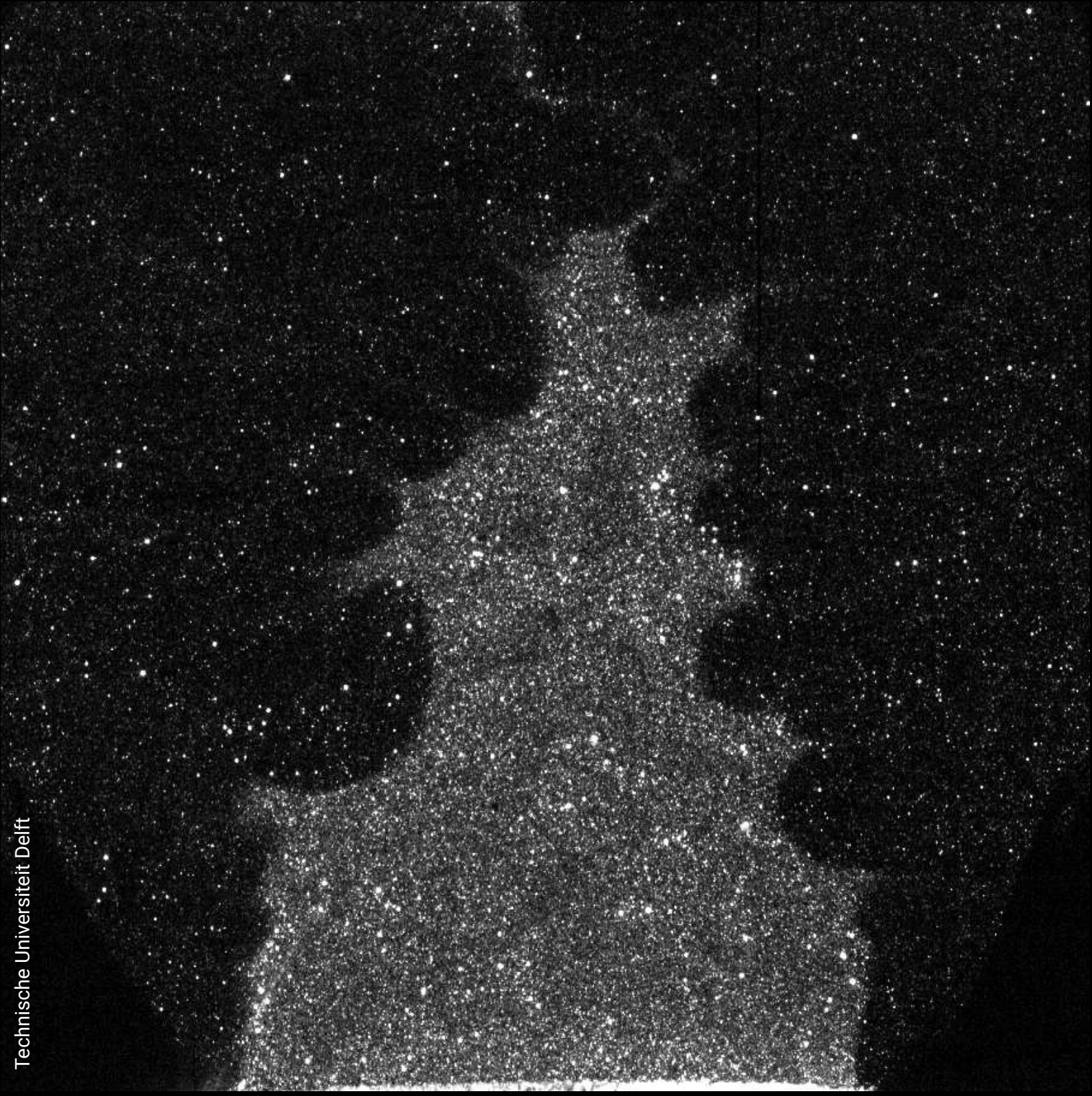

Technische Universiteit Delft

Experimental investigation of Boundary Layer Flashback in high H_2 concentration turbulent premixed jet flames

Filippo Faldella

TU Delft

Experimental investigation of Boundary Layer Flashback in high H_2 concentration turbulent premixed jet flames

by

Filippo Faldella

to obtain the degree of Master of Science
at the Delft University of Technology,
to be defended publicly on Friday 17 April, 2020 at 13:30 PM.

Student number:	4727568	
Project duration:	February 1, 2019 – April 17, 2020	
Thesis committee:	Prof. dr. ir. S.A. Klein,	TU Delft, supervisor
	Dr. ir. M.J. Tummers,	TU Delft, supervisor
	Prof. dr. D.J.E.M. Roekaerts,	TU Delft

Abstract

Hydrogen combustion in gas turbines could play an important role in the future energy transition. However, the design of flexible gas turbine combustors able to operate with a wide range of Dutch Natural Gas (DNG) and hydrogen fuels is accompanied by new complex challenges. Small quenching distance, high burning velocity and propensity to develop instabilities at leaner conditions makes hydrogen-rich fuels particularly prone to boundary layer flashback (BLF). Both academia and industry are currently involved in developing a better understanding of the BLF phenomenon, so that new generation combustors can be designed.
From recent experimental investigations carried out by the Technical University of Munich (TUM) research group, it has been noted that the configuration of the flame plays a crucial role in flashback propensity. In confined geometry, where the flame is partially or completely surrounded by walls, the boundary layer flashback propensity is much higher. Indeed, in the confined configuration the flame-flow interaction effects are very strong. However, even in the unconfined configuration it is not completely clear how the flame-flow interaction affects the boundary layer flashback onset.
In the present work, tube burners have been used to investigate different hydrogen/DNG turbulent flames. Particular attention was paid to the lean hydrogen premixed flames relevant for gas turbines combustors. In the first part of the investigation, flame regime maps have been used to characterize flashback propensity of different hydrogen/DNG mixtures at different equivalence ratios. Furthermore, the effect of tip temperature has been investigated by comparing flashback onset in both cooled and uncooled conditions. Particle image velocimetry (PIV) and Mie-scattering measurements have been used, both to obtain useful statistical data and to visualize the flashback transient phenomenon. Indeed, the lean hydrogen flame and DNG flame behaviour during flashback have been visualized and compared.
The results highlight that, the flame-flow interaction plays an important role. The interaction is related to the hydrodynamic or Darrius Landau instability which causes the presence of an adverse pressure gradient just downstream of the flame front. The adverse pressure gradient leads to a slowdown of the flow, which allows the flame front to propagate upstream. The coupling of this interaction with the velocity fluctuations of the turbulent field leads to flashback. The flashback location is outside of the viscus sublayer, but still in the proximity of the wall, where the velocity fluctuations are stronger and the distance between the average flame front and the burner exit is small. The distance between the burner tube outlet and the flame front directly affects the strength of the adverse pressure gradient on the approaching flow. The closer the flame front is to the burner exit, the more the incoming flow is deflected and retarded by the burner walls.
In these experiments the most significant difference between the DNG and hydrogen flame is not qualitative but quantitative. The mechanism itself is qualitatively the same, however, hydrogen flame flashback occurs much more abruptly. This is related to the response of hydrogen flame speed to stretch. Indeed, since the Lewis number is lower than one, the lean hydrogen flame speed increases with stretch leading to thermal-diffusive instability.

Acknowledgements

First of all I want to thank Mark and Sikke for the trust they gave me, by letting me develop the project autonomously. It has been very interesting to discuss the results and try to understand the dynamic of this phenomenon together.
I also want to thank Bart that, with his expertise, supported me during this project. Furthermore, he always tried to make feel comfortable in the work environment. I really appreciate that.
This research assignment lasted for slightly more than a year. During this period I had occasions to discuss my ideas and findings with students and researchers. A special thanks to Simone for listening to my ideas and critically pointing out when my observations were not on point. I would also like to thank Udhav, Ólafur, Luuk, Vilborg, Luis and Manas, they have always shown enthusiasm and interest for my research, trying to challenge me and providing me with new ideas and questions which definitely helped in the development of the thesis.
I also wan to thank other friends with whom I spent a great time. Thanks to the guys of Foulkeslaan, Andrea, Camilla, Daniele and Amina, it was nice to share this last year together. Thanks to my friends Vitto, Sidd, Marlinda and Kalyani for their kindness and support.
Finally, the biggest greetings are for my family. This achievement is as much yours as mine.

Filippo Faldella
Delft, April 2020

Contents

Nomenclature

Abbreviation

BLF	Boundary layer flashback
CCS	Carbon Capture and Storage
$CIVB$	Combustion induced vortex breakdown
CVG	Critical velocity gradient
DL	Darrius Landau instability
DNG	Dutch natural gas
DNS	Direct numerical simulation
$IPCC$	Intergovernmental Panel on Climate Change
NG	Natural gas
$RANS$	Reynolds averaged Navier Stokes
AFT	Adiabatic flame temperature

Greek symbols

α	Thermal diffusivity (m^2/s)
α_b	Refraction flame cone angle (°)
α_c	Flame cone angle (°)
α_t	Turbulent thermal diffusion coefficient (m^2/s)
δ_q	Quencing distance (m)
δ_r	Reaction zone thickness (m)
δ_f	Flame thickness (m)
δ_{ph}	Preheat zone thickness (m)
δ_p	Penetration distance (m)
ϵ	Turbulent kinetic dissipation (m^2/s^3)
κ	Flame stretch (s^{-1})
κ_c	Flame curvature (s^{-1})
κ_m	Mean flow flame strain (s^{-1})
κ_s	Flame strain (s^{-1})

κ_t Turbulence flame strain (s^{-1})

λ Thermal conductivity (W/(m·K))

μ_f Fluid Dynamyc viscosity (kg/(m·s))

ν Kinematic viscosity (m^2/s)

ϕ Equivalence ratio (-)

ρ Density (kg/m^3)

ρ_f Fluid density (kg/m^3)

ρ_b Burned gas density (kg/m^3)

ρ_u Unburned gas density (kg/m^3)

σ Burned to unburend gas density ratio (-)

σ_r Growth rate (-)

σ_s Statistical error (m^2/s^2)

τ_c Chemical time scale (s)

τ_0 Turbulent integral time scale (m)

τ_η Kolmogorov time scale (m)

Latin symbols

c_p Specific heat at constant desity (J/(kg·K))

d Diamter (m)

$\mathscr{D}_{i,j}$ Binary diffusion coefficient (m^2/s)

d_i Tube internal diameter (m)

d_p Particle diameter (m)

f Friction factor (-)

f_l Laminar burning flux ($kg/(s \cdot m^2)$)

g_c Critical velocity gradient (s^{-1})

h_i Species i specific enthalpy (J/kg)

k Turbulent kinetic energy (m^2/s^2)

k_w Wave number (m^{-1})

Ka Karlovitz number (-)

Ka_δ Karlovitz number based on reaction zone thickness (-)

$\mathscr{L}$ Markstein length (m)

l_0	Turbulent integral length scale (m)
l_η	Kolmogorov length scale (m)
Le	Lewis number (-)
Le_{eff}	Effective Lewis number (-)
$\dot{m}_l$	Laminar flame mass burning rate (kg/s)
$\dot{m}_t$	Turbulent flame mass burning rate (kg/s)
Ma	Markstein number (-)
N	Number of samples (-)
$\overline{n}$	Normal unit vector (m)
p_n	Pressure at normal conditions (mbar)
p_u	unburned gas pressure (Pa)
$\overline{q}$	Energy flux (J/(s·m^2))
Re	Reynolds number (-)
Re_p	Particle Reynolds number (-)
Re_t	Turbulent Reynolds number (-)
$\overline{\overline{S}}$	Flow strain tensor (s^{-1})
s_f	Flame speed (m/s)
s_l	Flame speed (m/s)
$s_{l,0}$	Unstretched laminar flame speed (m/s)
$s_{l,s}$	Stretched laminar flame speed (m/s)
s_t	Turbulent flame speed (m/s)
T	Experiment measuring time (s)
T_b	Burned gas temperature (K)
T_i	Ignition temeprature (K)
T_n	Temperature at nomal conditions (K)
T_u	Unburned gas temperature (K)
T_u	Unburned gas temperature (K)
T_{ad}	Adiabatic flame temperature (K)
T_{tip}	Burner tip temperature (K)
$u^{'}$	Velocity fluctuation in axial direction (-)

$\overline{u'u'}$	Normal Reynolds stress axial direction (m^2/s^2)
$\overline{u'v'}$	Reynolds shear stress (m^2/s^2)
$\overline{u}$	Mean axial velocity (m/s)
$\sqrt{u'^2}$	urms fluctuations (m^2/s^2)
$\vec{u}$	Velocity vector (m/s)
$u_0^{'}$	Turbulent integral velocity scale (m)
$u_\eta^{'}$	Kolmogorov velocity scale (m)
u^+	Normalized velcotiy (-)
U_b	Bulk velocity (m/s)
u_b	Burned gas velocity 1D (m/s)
u_f	Fluid velocity (m/s)
u_p	Particle velocity (m/s)
u_u	Unburned gas velocity 1D (m/s)
u_τ	Shear stress velocity (m/s)
$v^{'}$	Velocity fluctuation in radial direction (-)
$\overline{v'v'}$	Normal Reynolds stress radial direction (m^2/s^2)
$\overline{v}$	Mean radial velocity (m/s)
$w^{'}$	Velocity fluctuation in azimutal direction (-)
$\overline{w}$	Mean azimutal velocity (m/s)
y^+	Normalized wall distance (-)
Y_i	Species i mass fraction (-)
$Y_{F,u}$	Fuel mass fraction (-)
$Y_{O_2,u}$	Oxidaizer mass fraction (-)
Ze	Zeldovich number (-)

List of Figures

List of Tables

1 Introduction

Primary energy demand is continuously growing. Figure 1.1 shows a possible future prediction [56]. On the other hand, there is an urgent need for bringing down global emissions which are causing climate change. The Intergovernmental Panel on Climate Change (IPCC) reported that the 30-year period, since 1983 to 2012, has been the warmest of the last 1400 years in the Northern Hemisphere. Global warming is mainly due to the increase in greenhouse gas emission like carbon dioxide, methane and nitrus oxide, [41]. A large share of emissions is related to the use of fossil fuel [40], which are commonly employed in power plant for electricity production purposes. Among the fossil fuel, coal and natural gas are the main ones utilized for electricity production. Natural gas being preferable since it is the cleanest-burning and low CO_2 emission hydrocarbon [56]. However, carbon dioxide is a product of combustion so in order to meet emissions reduction other solutions are needed. Carbon Capture and Storage (CCS) techniques can play a role in reducing and eventually reaching negative carbon dioxide emissions. Indeed, CO_2 can be captured and separated before or after the combustion process [2]. Once separated, CO_2 can be stored underground or by mineral carbonation [46].

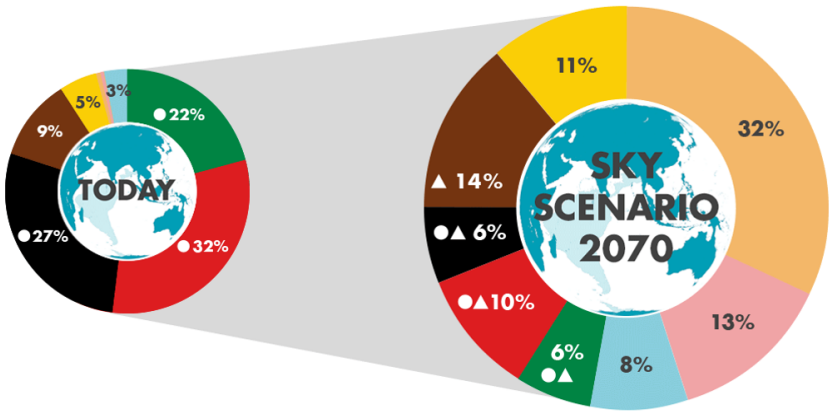

Figure 1.1: Shell Sky scenario of energy demand by source. [56]

Apart from the emission associated with the employment of fossil fuel, there are limited resources in a global scenario where energy demand is increasing. This further strengthens the need to extend the use of renewable energy sources,e.g. wind or solar. Thanks to their economic competitiveness, employment of renewable energy sources is growing, nevertheless it accounts for only 13.5

% (2017) of the world's Total Primary Energy Supply (TPES), as reported by the International Energy Agency [3]. One important drawback associated with renewable energy sources is their strong intermittency. Thus, in order to cope with demand peaks, it is necessary to store the energy when there is electricity production excess.
Hydrogen offers a solution, indeed, it can be employed as energy carrier and reconverted to electricity later. However the sustainability of hydrogen is strictly related to the way hydrogen is produced. In fact hydrogen can be classified as green, blue or grey. Green hydrogen is produced without any CO_2 emission, in grey hydrogen CO_2 is emitted and in blue hydrogen CO_2 is emitted and captured. Currently the share of green hydrogen produced is very low, however, since a significant increase is expected in the following decades [4], hydrogen can have an important role in world energy transition. Green hydrogen can be obtained via electrolysis [61], which allows to separate the water molecule into its constituent, and then reconverted to electricity by means of fuel cells or by burning it in gas turbines. The latter solution is attractive since relatively small investment cost would be necessary to the existing power plants. Furthermore gas turbines are suitable to balance intermittent power supply since they offer a fast start-up time, high efficiency and high turn-down ratio [28, 51]. Most importantly hydrogen combustion is carbon free, so, as long as green hydrogen is employed this solution is suitable to achieve the carbon signature reduction.
Hydrogen combustion however, introduces new significant challenges, hydrogen is very reactive, difficult to quench and when employed in lean premixed combustion it is characterized by inherently unstable processes [27]. Furthermore, the higher adiabatic flame temperature that a hydrogen air mixture has, at given equivalence ratio, compared to a Dutch Natural Gas (DNG) one, also poses the problem of NO_x production. As a consequence of hydrogen behaviour and features, flashback, in particular boundary layer flashback (BLF) is one of the main issues in gas turbine combustors. The flashback phenomenon causes the flame to move from the designed anchored location and to travel upstream in the combustor, reaching sections which are not meant to be at such high temperature. As a consequence life, reliability and performance of combustion systems are drastically reduced. Therefore BLF of hydrogen and rich hydrogen fuels, is currently a topic of interest of both academia and industry.

1.0.1. Research question

In this thesis boundary layer flashback of premixed turbulent jet flames has been investigated. The focus of the present work is to gain insight into the flashback mechanism of hydrogen turbulent jet flames using Particle Image Velocimetry (PIV) and Mie-scattering measurements. These measurement techniques have been used to visualize the phenomenon with high spatial and temporal resolution. The thesis also aim to obtain flame regime maps to asses the flashback propensity of a wide DNG/H_2 flames compositions range at different equivalence ratios and burner configurations, e.g. cooled/uncooled burner tip.

1.0.2. Thesis outline

In chapter 2 some general theoretical background about combustion and turbulence is provided. In particular the chapter starts with the description of a laminar premixed flame structure. Then flame stretch and instability mechanisms relevant to flame flow interaction are presented. In doing so particular attention is posed on the characteristics of hydrogen fuel behaviour. A basic description of turbulent flows and turbulent premixed combustion generalities end the chapter.
Chapter 3 deals with the flashback and, in particular, boundary layer flashback literature study. The classic critical velocity gradient model is presented, together with experimental results that show how different parameters and configurations affect the instability. Some recent advancement focusing particularly on hydrogen flame flashback are also presented.
Chapter 4 introduces the experimental setup, the measurement technique and the experiments car-

ried out in this study.
In chapter 5 the results are presented and discussed.
Finally, conclusions and recommendations for further investigations are provided in chapter 6.

2

General theory background

In this chapter some important topics related to combustion and turbulence will be covered. The topics selection presented is meant to be propaedeutic for the next chapters of the thesis. In particular we will deal with the basics of laminar premixed combustion, flame speed specifically for a Bunsen flame, the effect of flame stretch on flame speed, the Darrius Landau or hydrodynamic instability and the thermal diffusive instability, some basics of turbulent flow and turbulent premixed combustion.
If not differently indicated all the content in this chapter refers to [34], [36], [62], [47], [45].

2.1. Laminar premixed flames

2.1.1. Flame structure

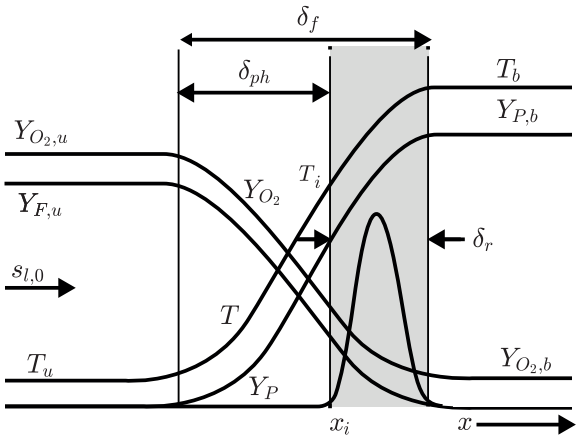

Figure 2.1: One-dimensional laminar premixed flame structure, based on the single one-step reaction asymptotic analysis

Figure 2.1 shows a laminar premixed flame structure. This representation assumes the flame to be one-dimensional, stationary, in the low Mach number limit and single-step large activation energy chemistry. Based on these assumptions, the combustion process can be considered isobaric and that no reaction occurs until a sufficiently high temperature is reached, ignition temperature (T_i) . Once the ignition conditions are met, the reaction occurs very quickly until the deficient reactant is consumed (under these hypothesis the reaction zone is referred as a sheet). Figure 2.1 shows three zones: (1) unburned side, (2) reaction zone, (3) burned side.
Unburned side. Fuel and oxidizer, perfectly mixed, are convected from left to right with a velocity equal to the burning velocity or laminar flame speed, s_l, they are characterized by a certain equiva-

lence ratio ϕ, pressure p_u and temperature T_u, and enter the preheat zone which has a characteristic thickness δ_{ph}. Under these assumptions, in the preheat zone there is not heat release. In this region, convection and diffusion dominates and balance. As approaching the reaction zone, reactants start to diffuse into it and their mass fraction reduce $Y_{O_2,u}, Y_{F,u}$ (subscript "u" stands for unburned). At the same time, the incoming gas are heated by conduction by the burnt gases.
The Lewis number is a very important non-dimensional transport quantity, especially when lean hydrogen mixtures are employed, see equation 2.1.

$$Le_{i,j} = \frac{\alpha}{\mathscr{D}_{i,j}} = \frac{\lambda}{c_p \rho \mathscr{D}_{i,j}} \tag{2.1}$$

The Lewis number is the ratio between the thermal and mass diffusivity, it indicates which, between the heat or mass diffusion processes is prominent. In lean hydrogen combustion the Lewis number is smaller than one, thus hydrogen diffusion towards the reaction zone outbalance heat back diffusion. A smaller then one Lewis number leads to a local non conservation of total enthalpy, which causes superadiabatic or subadiabatic flame temperatures. This results in changes in the flame speed (through the Arrhenius type reaction rate) that can have important consequences that will be analysed in the thermal diffusive instability and flame stretch sections 2.3 and 2.2. On the other hand, for mixtures characterized by Le $\simeq$ 1, (most hydrocarbons), the two transport phenomena balance each other out and the flame speed remains almost unaltered.
Going back to figure 2.1, when the temperature reaches T_i the reactions start, we have entered the **reaction zone** which is characterized by a certain thickness δ_r . In this zone the fuel is consumed, radicals are initially produced in chain-branching reaction and then oxidized in chain-breaking reactions. These phenomena are accompanied by heat release and consequent temperature gradients. Reactions end when the deficient reactant is depleted (in this lean premixed flame case fuel). it can be noticed that, due to a very steep concentration gradient, some products, as well as some radicals, diffuse upstream the reaction zone into the preheat zone. Finally, reaction products and leftover air coexist in the so called equilibrium region or burned side. This region is characterized by the maximum value of burned gas temperature, T_b . When assuming no heat loss T_b equals the adiabatic flame temperature, T_{ad}, which can be calculated starting from the first law of thermodynamics for an adiabatic isobaric process and considering the initial unburned gas temperature T_u, the enthalpy of reaction or heating value of the fuel, specific heat at constant pressure and the amount of a fuel reacting.
The flame can be considered made of two zones, the preheat zone, where the phenomenon is dominated by a convection-diffusion balance and the reaction zone in which the diffusion-reaction balance has the prominent role. Since $\delta_{ph} >> \delta_r$ the flame thickness is $\delta_f \simeq \delta_{ph}$. The flame thickness δ_f can be defined as the temperature difference between burned and unburned gases, divided by the maximum temperature gradient in the stream wise direction,

$$\delta_f = (T_b - T_u) / \frac{dT}{dx}|_{max}. \tag{2.2}$$

This definition is based on the simplification of a linear temperature increase.
The continuity equation holds across the flame front, in this one dimensional case it reads,

$$d(\rho u)/dx = 0. \tag{2.3}$$

We can thus define a quantity, the laminar burning flux f_l that characterizes the rate of flame propagation,

$$f_l = \rho_u u_u = \rho_u s_l = \rho_b u_b. \tag{2.4}$$

From f_l we can do some simple considerations about the velocity increase across the flame front. Indeed, the velocity of the burned gases can be estimated from the ratio of the unburned and burned

gas $u_b/u_u = \rho_u/\rho_b$ (methane/air flame ρ_u/ρ_b ratio ~ 7). In particular by means of the ideal gas law and assuming an isobaric process, the ratio between densities can also be written as temperature ratio, $\rho_u/\rho_b = T_b/T_u$.
The content presented in this section refer to

2.1.2. Bunsen laminar flame speed

The Bunsen burner is a very widely used burner. It consists of simple tube. The fuel and the oxidizer enters the burner from one side and start mixing, such that at the tube outlet an evenly premixed mixture is obtained and a flame can be established. Under steady and laminar flow conditions the flame has a characteristic conical shape. Since we have used this kind of burner in our investigation, we want to describe the kinematic balance between the unburned and burned gas velocity across the flame front. The following description applies to laminar flames. However it can also be used to describe important aspects of turbulent flames which have been considered in the present work. In particular, when the average flame is considered its cone angle can be determined, as it will be shown in 5.3, and this parameter can be related to some extent to features that characterize the statistics of the turbulent jet flame. In figure 2.2, the kinematic balance for a steady oblique

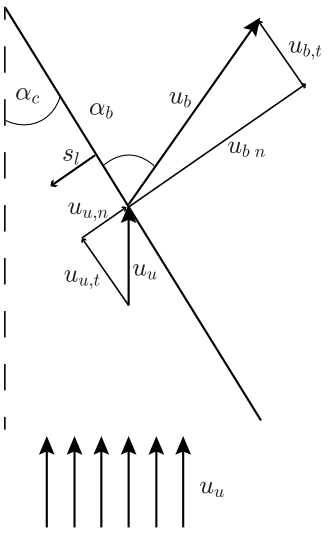

Figure 2.2: Kinematic balance for a steady premixed Bunsen flame

premixed Bunsen burner flame is described. The reactants incoming flow, characterized by a constant velocity u_u, approaches the flame front at an angle α_c. Once the flow has crossed the flame front it is refracted and it leaves the flame front with a certain angle α_b and velocity u_b. The kinematics of a velocity vector across the flame can be described by assuming tangential velocity continuity and burning flux continuity in the direction normal to the flame front, equation 2.4. The laminar flame speed here is then defined as the normal component of u_u. Accordingly with what discussed in the previous section, the magnitude increase of velocity normal component is equal the burned/unburned gas density ratio σ. It follows that, knowing the flame cone angle α_c, the laminar flame speed can be determined, see equation 2.5.

$$s_l = u_u \sin\alpha_c \tag{2.5}$$

It is interesting to observe that, at the tip of the cone there is no angle between the incoming flow and the flame front. As a consequence the flame speed has to be the same as the flow velocity. So the flame speed at the cone tip is larger by a factor equal to $1/sin(\alpha)$. The explanation for this is the flame curvature at the tip. Considering as an example a DNG flame, the velocity at the tip is higher

because in addition of the heat conduction normal to the flame front, also the lateral part of the flame preheats the incoming reacting mixture. On the other hand in the case of non-equidiffusive flames ($Le \neq 1$), like the lean H_2 air flames considered in this work, the behaviour is different. If the Le number is smaller then one the tip results to be less 'energetic' since there is a defocusing effect on the concentration of the deficient reactant. This leads to a phenomenon called tip opening effect. This is further addressed in section 2.2.
Since in this thesis we will investigate the flashback phenomenon, another relevant feature of Bunsen flames is their stabilization mechanism. A Bunsen flame is stable for a considerable range of flow velocity and mixture concentrations. The flame is locally stabilized within the burner rim. At this location the two main mechanisms affecting the laminar flame speed, which in the stable regime is locally in balance with the flow velocity (flame anchoring), are heat loss caused by the combustor rim and the change in mixture concentration due to diffusion and entrainment of ambient air. Further is the flame edge location and stronger are diffusion and air entrainment effects on flame speed, on the other hand, heat loss to the rim diminishes. The distance at which the flame holds is then defined by a trade off between this two effects.
The effect of flame curvature at the flame tip was explained in this paragraph, in the next section the concept of flame stretch and its influence on premixed flames will be shown more in general.

2.2. Flame stretch

Flame-flow interaction, flow non uniformity and flame curvature characterize a real flame. These combined effects are strongly related to the concept of stretch rate. In general, the stretch rate, κ, can be defined as the Lagrangian time derivative of the logarithm of the area of an infinitesimal surface element and it has the dimensions of s^{-1}, [34].

$$\kappa = \frac{1}{A}\frac{dA}{dt} \tag{2.6}$$

The flame stretch can also be written as follow, [36],

$$\kappa = \underbrace{-\overline{n}\cdot\overline{\overline{S}}\cdot\overline{n} + \nabla\cdot\vec{u}}_{\kappa_s} \underbrace{- s_f\left(\nabla\cdot\overline{n}\right)}_{\kappa_c} = \kappa_s - \kappa_c \tag{2.7}$$

The advantage to visualize flame stretch as in equation 2.7, is that we can distinguish two contributions, namely, κ_s, related to flow non-uniformity (strain) and κ_c to flame curvature. Furthermore, the effects of strain can be further divided in the combined effect of κ_m, related to the mean flow, and κ_t, related to turbulence, [59]. In particular, since our investigation focuses on an incompressible fully developed pipe flow of the near field of turbulent free jets, flow divergence and thus κ_m are negligible, the flame stretch associated with strain is then mainly related to κ_t [27].

2.2.1. Flame stretch phenomenology

In this section it is explained how stretch affects the flame structure and response. Mixtures with different thermal and species diffusivities show a very strong sensitivity to stretch as it can modify the local flame temperature and flame speed. In order to explain the physics mechanisms introduced by stretch, consider figure 2.3. The right side of the picture shows a situation in which the flow is strained and the flame front is flat, while the left shows a curved flame front and uniform flow. In figure 2.3 the reaction zone and a control volume which has the size of the preheat zone are indicated. Furthermore, the reaction zone is assumed to be a sheet (high activation energy and one-step kinetic). Let us consider the left side of figure 2.3. Note that both the diffusive fluxes, heat and species, occur normal to the their respective iso-surface. The heat diffuses from the reaction zone to the preheat zone, while the species diffuse in the opposite direction. Moreover, there is a convective flux through the front and the back of the control volume, but not through the sides. From the figure

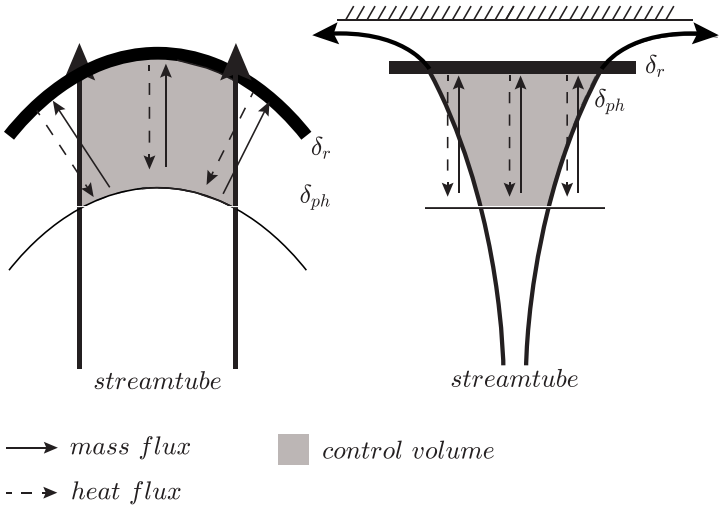

Figure 2.3: Effects of flame stretch on the flame structure in case of nonequidiffusion. On the left side of the figure a curved flame front and a uniform flow are shown. In particular, the grey area is the considered control volume and coincides with the thickness of the preheat zone δ_{ph}. The thick black line represents the reaction zone δ_r. On the right side a stagnation flame is shown. This flame is characterized by flat flame front and strained flow [36].

it is clear that, when the flame has a negative curvature with respect to the flow direction, there is a focusing of thermal energy into the control volume and a defocusing of reactant species diffusion. When the heat and mass fluxes are equal and heat loss is neglected, the control volume is adiabatic. On the other hand, if one exceeds the other, there is some total enthalpy loss or gain through the control volume.

$$\overline{q} = \underbrace{-\lambda \nabla T}_{\text{Heat flux}} - \underbrace{\rho \sum_{i=1}^{N} h_i \mathscr{D} \nabla Y_i}_{\text{Mass flux}} \tag{2.8}$$

The gain or loss of energy can be estimated by considering the energy fluxes, equation 2.8, [36]. Where radiative heat transfer, DuFour effect are neglected and Fickian diffusion is assumed. λ is the thermal conductivity, h_i is the species specific enthalpy, and Y_i is the species i fraction. Now, since before we said that the convective flux is only entering and leaving the control volume through the front and the back, a net flux of energy through the sides, would lead to some energy loss or gain. Whether or not there is a net gain or loss depends on the Lewis number. If Le = 1, in weakly curved flames, the energy in the control volume does not change. On the other hand, for a negative curvature (left side figure 2.3) and for a mixture with Le < 1, (lean H_2-air mixture) the chemical energy loss through mass diffusion is higher than the energy gained through heat conduction. The control volume is then characterized by lower energy than the mixture average, resulting in sub-adiabatic flame temperature and lower flame speed. The opposite effect occurs when the same flame but positive curvature are considered. The right side of figure 2.3 shows the effect of stretch related to flow straining, this configuration is equivalent to the one of a positively curved flame. Considering the lean H_2-air mixture, the control volume gains energy. Burning rate increases together with flame speed.

Another effect that has to be considered is the differential diffusion effect, that can be expressed as the ratio between the fuel and the oxidizer diffusivity coefficients, e.g. $\mathscr{D}_{fuel}/\mathscr{D}_{O_2}$. In the case of positive curvature (right side figure 2.3) it can be seen that both the reactants diffuse towards the reaction zone, entering the control volume. However the net gain of H_2 through the control volume is greater than the one of O_2. As H_2 is lighter and much more diffusive then O_2. Thus, the control volume equivalence ratio (ϕ) is higher than the one characterizing the incoming reactive mixture. This leads to higher flame speed, flame temperature and burning rate. Conversely under rich con-

ditions, differential diffusion effect leads to a leaner mixture. The opposite situation occurs when the fuel is less diffusive and heavier then O_2.

2.2.2. Effect of stretch on flame speed

Under the assumption of weakly stretched flames, valid when the Karlovitz number is much smaller than one (Ka«1), the dependency of the flame on the different stretch mechanisms (strain and curvature) can be assumed to be the same, [36]. The Karlovitz number is defined later in turbulent premixed combustion section 2.6. In this case, the flame speed functional relation with stretch can be expressed by means of one coefficient only, and the stretched laminar flame speed can be defined, see equation 2.9.

$$s_{l,s} = s_{l,0} - \mathscr{L}\kappa \tag{2.9}$$

Where subscript 's' and '0' indicates stretched and unstretched respectively and $\mathscr{L}$ is the Markstein length. The Markstein length is a coefficient which linearly relates the flame speed sensitivity to stretch. This result has been obtained by asymptotic analysis based on high activation energy, one-step kinetics. In particular a negative Markstein length causes the flame speed to increase while a positive one to decrease. By dividing this quantity with the flame thickness δ_f we get a non dimensional parameter, called Markstein number Ma. Matalon and Matkowsky derived this equation by means of asymptotic analysis [38], which is when the entire flame, preheat and reaction zone together, are treated as a surface.

$$Ma = \frac{\mathscr{L}}{\delta_f} = \frac{\sigma}{\sigma-1}\int_1^\sigma \frac{\lambda(x)}{x}dx + \frac{Ze\left(Le_{eff}-1\right)}{2(\sigma-1)}\int_1^\sigma \frac{\lambda(x)}{x} ln\left(\frac{\sigma-1}{x-1}\right)dx \tag{2.10}$$

In equation 2.10 we find the Zelodovich number (Ze), non-dimensional activation energy times the non-dimensional heat release, the thermal conductivity of the mixture $\lambda = \lambda(T)$, function of T only, x is the one-dimensional flame coordinate, and the effective Lewis number. Le_{eff} is defined as the weighted average of the individual Lewis numbers of the fuel Le_F and the oxidizer Le_O, respectively. We want to emphasize that, if the effective Lewis number equals one, the second term on the right hand side goes to zero. This indicating that the Markstein length and consequently the dependence of a flame to stretch is highly affected by its heat and mass diffusivity. In equation 2.10, both the laminar flame speed and the Markstein length are defined with respect to the unburnt gas.

2.3. Thermal-diffusive flame instability

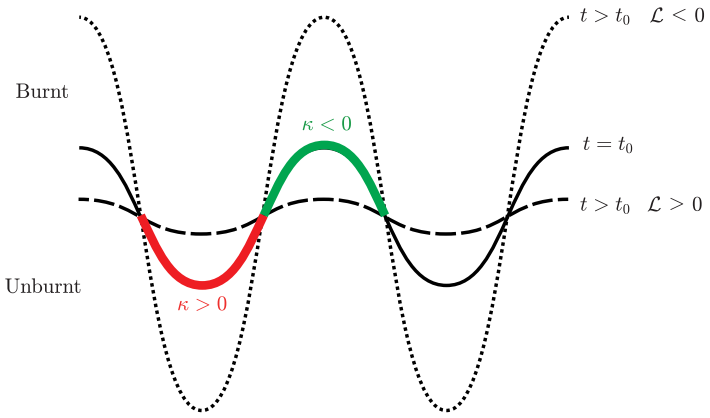

Figure 2.4: Schematic illustration of the thermal diffusive instability. An initially perturbed flame front (t = t_0) can evolve in two ways: (1) disturbance is damped out ($\mathscr{L} > 0$), (2) the disturbance grows ($\mathscr{L} < 0$).

With thermal-diffusive instability we mean the combined effect of non unity Lewis number and differential diffusion effects. In brief, the first mechanism is related to unbalanced thermal and

species diffusion, while the latter occurs when the fuel and oxidized have different species diffusion, leading to locally different equivalence ratio. Lean hydrogen combustion is characterized by both these mechanisms. Here we want to describe the thermal-diffusive instability development. In order to do so consider figure 2.4. Assume that the flame front is perturbed by an harmonic wave at the instant $t = t_0$, some bulges of the flame will have a positive curvature while some a negative one with respect to the flow direction. We also assume that the flow is uniform, and that the only effect of stretch on flame speed is related to flame curvature. If a mixture characterized by negative markstein length $\mathscr{L}$ is considered (lean H_2-air), at the instant $t > t_0$, the perturbations will both grow. Indeed the negative Markstein length which characterizes these flames, will cause the flame speed to increase when κ is negative, while the flame speed will decrease for $\kappa > 0$. The flame bulge negatively oriented will then be able to further develop upstream, while the negative bulge will be pushed downstream. This mechanism will then repeat more drastically since the curvature of the flame will be even higher, as it can be seen in equation 2.11. This feedback process will continue until the flame surface, suffering to much stretch will extinguish. Consider a DNG flame, which is characterized by positive Markstein length, at $t > t_0$, the amplitude of the initial disturbance will decrease, see figure 2.4. Indeed it can be seen from equation 2.11 that, the positively curved flame bulge burning velocity will decreases and the flame front will be pushed downstream. On the other hand, the negatively curved flame bulge burning velocity will increase and the flame front will move upstream. As a result, for flames characterized by positive Markstein length the thermal-diffusive mechanism has a stabilizing effect.

$$s_f(\kappa) = s_{l,0} - s_{l,0}\mathscr{L}\kappa_c \tag{2.11}$$

2.4. Hydrodynamic flame instability

The hydrodynamic instability, also called Darrius-Landau instability is due to heat release associated with the combustion exothermic reaction, which causes the gas acceleration across the flame front. The velocity component normal to the flame front, in fact, accelerates of a factor similar to the density ratio between the burned and unburned gas, see section 2.1.2.
Figure 2.5 shows two streamtubes A approaching and leaving a perturbed flame front. The following assumptions hold: (1) the flame is infinitely thin (density jump across flame front), (2) the flame propagates with constant flame speed (equal to the laminar flame speed), (3) σ across the flame is constant.

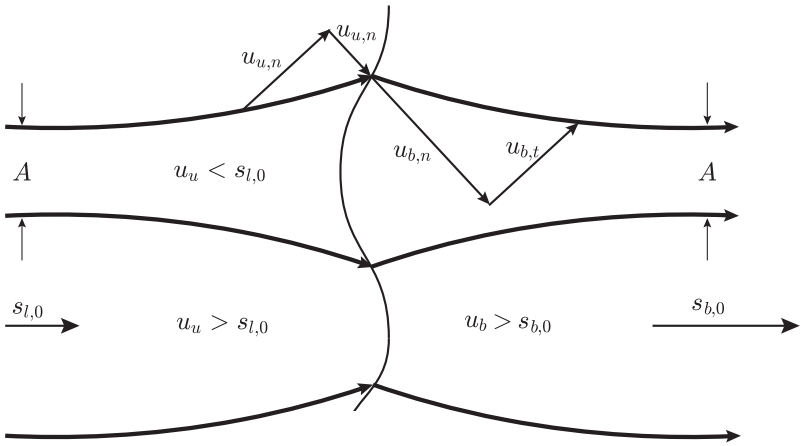

Figure 2.5: Schematic illustration of the Darrius Landau or hydrodynamic instability. A perturbed flame front convex towards the unburned gas causes a streamtube to diverge, the flow velocity decreases. As a consequence at this location the flame speed is greater then the flow velocity and the flame front moves upstream. Conversely if the flame front is concave the flow accelerates just upstream the flame front, pushing the flame front downstream.

An explanation to this instability can be given using a mass conservation argument, see Law [34]. The flame surface is perturbed by a small disturbance. Sufficiently upstream and downstream the flame front the area of streamtubes are the same since any disturbances is present at these locations. However, because of thermal expansion, the normal component downstream the flame front is larger than the normal component upstream the flame front. Furthermore, the tangential component upstream and downstream the flame front is continuous. From these two considerations it follows that the streamlines must respectively diverge and converge in approaching the positive and negative curved segment of the flame. In other words, when the streamtube approaches the convex segment of the flame it widens and the velocity has to decrease. Since the flame speed was assumed to remain constant, the flow velocity becomes locally slower than the flame speed and consequently the flame front moves upstream. Conversely, the opposite situation occurs when the flame front is concave, the flow accelerates and pushes the flame front downstream. This phenomenon is inherently unstable. Moreover, no wavelength has been considered in the explanation and therefore the phenomenon is unstable for all wavelengths, [34]. The main point that has to be noticed is that the flame bulges cause the approaching flow to decelerate if they are positively curved, this is due to an adverse pressure gradient. The opposite occurs when the flame bulges are negatively curved.
Matalon [38] in his studies about intrinsic flame instabilities shows the result of the linear stability analysis for a planar flame, see equation 2.12. He considered the same assumptions presented before in the paragraph.

$$\sigma_r = s_{l,0} k_w \frac{-\sigma + \sqrt{\sigma^3 + \sigma^2 - \sigma}}{\sigma + 1} \tag{2.12}$$

σ_r is the non-dimensional growth rate of the perturbation, σ is the density ratio, k_w is the wave number. The red line in figure 2.6 ($\mathscr{L} = 0$) shows that the Darrius-Landau instability is inherently unstable for all wave numbers.
Matalon [38] also performed a linear stability analysis taking into account the effect of flame sensitivity to stretch κ. In particular, the assumptions are the following: (1)viscosity, gravity and compressibility in both the burnt and unburnt gas are negligible, (2) the density is discontinuous at the flame front, (3) only the stretch effect related to curvature are retained. The following dispersion re-

lation, equation 2.13, shows the results of the linear stability for a planar flame, where the combined effects of the Darrius-Landau and thermal-diffusive instability have been considered.

$$\sigma_r = \frac{s_{l,0} k_w}{1+\sigma} \left[\sqrt{1 + k_w^2 \mathscr{L}^2 - \frac{2 k_w \mathscr{L}}{\sigma} + \frac{1-\sigma^2}{\sigma}} - (1 + k_w \mathscr{L}) \right] \tag{2.13}$$

The results can be visualized in figure 2.6 as a function of the wave number. It is shown how the growth rate changes with the Markstein length $\mathscr{L}$. As the Markstein length grows, more wave numbers get stabilized and the instability region decreases.
The wave number is the inverse of wave length, when large wave number disturbances have a negative growth rate, it means that small wavelength disturbances are dumped out. This shows that the stretch effects, are stronger at small length scale. Indeed, larger is the flame front radius of curvature and weaker are the effects of stretch, [38]. Following the same reasoning line, the big length scale disturbances, small k_w, are the more hydrodynamically unstable, since no stabilizing effect is available at such big scale, [38]. A conclusive and crucially important remark is that for mixtures characterized by a negative Markstein length, such as lean hydrogen-air mixtures, all wave number disturbances are unstable, see figure 2.6.
The hydrodynamic instability and the thermal diffusive instability combined effect is of primary importance in the flashback event.

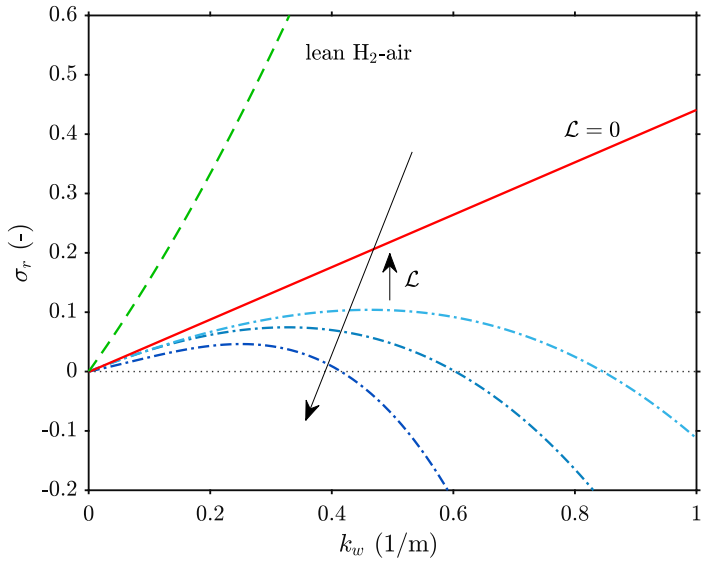

Figure 2.6: Dispersion relation resulting from the linear stability analysis of a planar flame, see equation 2.13. The plot shows the growth rate of a disturbance as a function of the wave number. In particular the green curve shows that for a lean H_2-air mixture, characterized by negative Markstein length, the growth rate is positive. The same can be said for the red line that show the solution to the Darrius-Landau instability when no effect of stretch are considered. The three blue curves show how for increasing Markstein length the region of positive disturbance growth rate decreases.

2.5. Turbulent flow

Turbulent flows are characterized by high Reynolds number (Re), which is defined as the ratio between inertia and viscous forces in the flow, and by the presence of eddies. Their size differs, largest eddies scale with characteristic length of the geometry. They tend to break up into smaller ones until the minimum length scale is reached. This process is the way through which the kinetic energy is transferred from large to small scales, where finally it is dissipated by viscous forces. A turbulent flow can be described by means of the so called Reynold's decomposition. An instantaneous velocity can be written as the sum of ensemble mean and a fluctuating component. The instantaneous axial

velocity u, radial velocity v and azimuthal velocity w can be written in the following way, equation 2.14.

$$u(\mathbf{x},t) = \overline{u} + u^{'}, \qquad v(\mathbf{x},t) = \overline{v} + v^{'} \qquad \text{and} \qquad w(\mathbf{x},t) = \overline{w} + w^{'} \tag{2.14}$$

The Reynold's decomposition is then substituted in the Navier Stokes equations which are then averaged in time yielding to the Reynolds averaged Navier Stokes equations (RANS). When the equations are averaged, some terms in the form of $\overline{u^{'}v^{'}}$ appear. Since they have the same effect as stresses acting on a surface these terms are named Reynolds stresses [43]. Considering the two dimensional form of the Reynolds stress tensor, it has the so called normal stresses on the diagonal, in axial direction $\overline{u^{'}u^{'}}$ and radial direction $\overline{v^{'}v^{'}}$, and the shear stresses off diagonal $\overline{u^{'}v^{'}}$.

2.5.1. Turbulent scales

A turbulent flow is characterized by a spectrum of eddies. Each eddy rotational velocity and diameter characterize its velocity and length scale. By means of a normalized space correlation based on the velocity of two adjacent points is possible to estimate the eddies length scale. Large scale eddies can be characterized by the integral length scale l_0. The largest concentration of turbulent kinetic energy occurs in the neighbourhood of l_0. The integral length scale is typically set by the size of the device or phenomenon, or confinement of the flow field. By defining the characteristic velocity fluctuation at integral length scale $u_0^{'} = \overline{\left(u^{'2}\right)}^{1/2}$ and assuming isotropy, the turbulent kinetic energy of the flow can be expressed, equation 2.15, see [34].

$$k \simeq \frac{3}{2}u_0^{'2} \qquad \text{, in general,} \qquad k = \frac{1}{2}\left(\overline{u^{'2}} + \overline{v^{'2}} + \overline{w^{'2}}\right) \tag{2.15}$$

The turbulent Reynolds number can then be defined. It is based on the characteristic velocity fluctuations at integral length scale and on the integral length scale eddies.

$$Re_t = \frac{u_0^{'} l_0}{\nu} \tag{2.16}$$

Each different size eddy is characterized by a certain amount of kinetic energy, which depends on the velocity fluctuation at the same eddy length scale. The kinetic energy is then transferred from large to small scale eddies through various modes. This is the so called energy cascade concept. It is based on the Kolmogorov's postulate, which says that at sufficiently high Reynolds number, it exist a range of scales through which the energy transfer rate is independent of molecular viscosity. This universal range of scales through which the energy cascade occurs is called the inertial subrange. Dimensional consideration yields the rate of energy transfer in this range to be as follow [34],

$$\epsilon \approx \frac{u_0^{'3}}{l_0} \approx \frac{k^{\frac{3}{2}}}{l_0}. \tag{2.17}$$

The turbulent integral time scale or the turnover time of the integral scale eddies, is then

$$\tau_0 \approx \frac{l_0}{u_0^{'}} \approx \frac{k}{\epsilon} \tag{2.18}$$

Under this hypothesis the turbulent kinetic energy is transferred continuously to smaller size eddies at a constant rate (ϵ), until at the eddies smallest length scale, it is dissipated through viscosity. The minimum scale is called Kolmogorov scale. For energy conservation, the rate at which energy is dissipated at the Kolmogorv scale has to be the same at which kinetic energy is transferred from an eddy to another in the inertia subrange (ϵ). Thus, by dimensional analysis argument, using ν and ϵ we can define Kolmogorov time scale, length scale and velocity scale.

$$\tau_\eta \approx \left(\frac{\nu}{\epsilon}\right)^{\frac{1}{2}}, \qquad l_\eta \approx \left(\frac{\nu^3}{\epsilon}\right)^{\frac{1}{4}}, \qquad u_\eta^{'} \approx \left(\nu^3\epsilon\right)^{\frac{1}{4}} \tag{2.19}$$

Using definition of ϵ, see equation 2.17, the integral length and time scales can be related to the Kolmogorov ones.

$$\frac{l_0}{l_\eta} \approx Re_t^{\frac{3}{4}}, \qquad \text{and} \qquad \frac{\tau_0}{\tau_\eta} \approx Re_t^{\frac{1}{2}} \tag{2.20}$$

the difference between l_0 and l_η grows as Reynolds increases.

2.5.2. RANS equation for Jet flow in cylindrical coordinates

In the experiments we have used tubes burners with inner diameter d_i. This leading, in case of isothermal flow, to a jet flow, characterized by a certain Re number. The bulk velocity has been used to characterize the Reynolds number, equation 2.21.

$$U_b = \frac{2\pi \int_0^{d_i/2} \overline{u}(r) r dr}{\pi d_i^2/4}, \qquad Re = \frac{U_b d_i}{\nu} \tag{2.21}$$

Considering the flow still inside the tube, a turbulent flow characterized by a sufficiently big length over diameter ratio will get fully developed. This meaning that the mean flow gradients along the axial direction are zero. We assumed non-swirling, statistically stationary and axisymmetric turbulent flow. This leads to the following RANS equation in cylindrical coordinates,

$$\frac{\partial \overline{u}}{\partial x} + \frac{1}{r}\frac{\partial \left(r\overline{v}\right)}{\partial r} = 0 \tag{2.22}$$

$$\frac{\partial \overline{u}}{\partial t} + \overline{u}\frac{\partial \overline{u}}{\partial x} + \overline{v}\frac{\partial \overline{u}}{\partial r} = -\frac{1}{\rho}\frac{\partial \overline{p}}{\partial x} - \frac{\partial \overline{u'u'}}{\partial x} - \frac{1}{r}\frac{\partial \left(r\overline{u'v'}\right)}{\partial r} + \nu\nabla^2\overline{u} \tag{2.23}$$

$$\frac{\partial \overline{v}}{\partial t} + \overline{u}\frac{\partial \overline{v}}{\partial x} + \overline{v}\frac{\partial \overline{v}}{\partial r} = -\frac{1}{\rho}\frac{\partial \overline{p}}{\partial r} - \frac{\partial \overline{u'v'}}{\partial x} - \frac{1}{r}\frac{\partial \left(r\overline{v'v'}\right)}{\partial r} + \frac{\overline{w'w'}}{r} + \nu\left(\nabla^2\overline{v} - \frac{\overline{v}}{r^2}\right) \tag{2.24}$$

where equation 2.22 is the continuity equation, 2.23 is the momentum balance in axial direction and 2.24 is the momentum balance in radial direction.
These equations will be used in the last part of the result chapter, 5.5.2, in particular the momentum balance in axial direction, 2.23. However even in the previous sections of the results chapters the normal and shear Reynolds stresses, as well as the velocity components will be extensively used to characterize both the isothermal and reactive turbulent flows.

2.5.3. Boundary layer flow

When there is interaction between a solid wall, for instance a flat plate, and fluid flowing the no-slip boundary condition at the wall causes the development of a boundary layer.
The boundary layer flow can be divided into three zones: (1) inner layer, (2) overlap region, (3) outer layer. The velocity profile can be expressed by means of normalized quantities, the normalized velocity profile (u^+) and normalized wall normal distance (y^+),

$$u^+\left(y^+\right) = \frac{u\left(x,y\right)}{u_\tau\left(x\right)} \quad \text{and} \quad y^+ = \frac{u_\tau\left(x\right) y}{\nu}, \tag{2.25}$$

where the shear stress velocity $u_\tau = \sqrt{\tau_w/\rho}$ depends on the density ρ and on the wall shear stress τ_w. Expressing the mean velocity profile by means of these two non-dimensional quantities allows to classify the flow regions in the following way ,see figure 2.7: (1) **viscous sublayer** $\left(y^+\right) < 5$, where the velocity profile is linear and shear stress plays the prominent role; (2) **buffer layer** $5 < \left(y^+\right) < 30$, which is a transition region between the viscous sublayer and the logarithmic layer; (3) **logarithmic region** $\left(y^+\right) > 30$, where the velocity profile is described by a logarithmic law of the wall, [47].

In the viscous sublayer or laminar region the velocity profile is linear and the normalized velocity equals the normalized wall normal distance $u^+ = y^+$. The logarithmic region is considered to begin at a certain normalized wall normal distance, where the logarithmic law of the wall holds. The viscous sublayer and the buffer layer are part of the inner region, where viscous shear is dominating. The logarithmic region, where both turbulent and viscous shear are important belongs to the overlap region. Finally there is the outer region, where turbulent shear dominates.

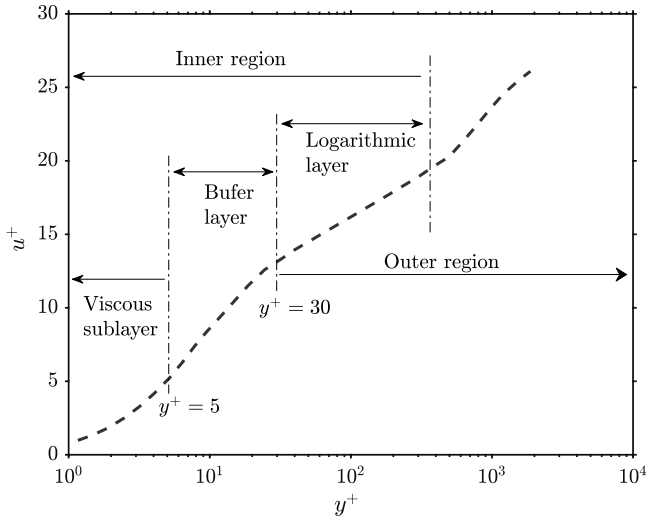

Figure 2.7: A sketch of the developed turbulent boundary layer in dimensionless coordinates.

2.6. Turbulent premixed combustion

In turbulent premixed combustion the turbulent flow interacts with a premixed flame. A laminar premixed flame front has well defined location and is stationary in time, in contrast, the turbulent flow velocity fluctuations curve and wrinkle the flame front of a turbulent premixed flame. As a consequence, turbulent premixed flame are characterized by higher flame surface and burning velocity, [62].

Different modes of turbulent premixed combustion can be classified based on the scale and intensity of the flame thickness, flame speed of the mixture and turbulent eddies. The turbulent premixed combustion modes can be classified by means of the Borghi diagram. In particular in the present work the flames that have been investigated belong to the wrinkled flame regime.

The characteristic length and time scales of the flow have been defined in section 2.5.1. For what concerns the flame, we can defined two different length scales, one related to the flame thickness (convection/diffusion), (δ_f), and one to the inner layer thickness (diffusion/reaction), (δ_r) which is much smaller than the flame thickness.

The turbulent Reynolds number can be written as the ratio between turbulent flow and flame scales. Assuming that the Schmidt number is equal to one (Sc = ν/α, viscosity, thermal diffusivity ratio), we can write the turbulent Reynolds number in the following way,

$$Re_t = \frac{l_0 u_0'}{\nu} = \frac{l_0 u_0'}{\alpha} = \frac{l_0 u_0'}{s_l \delta_f}. \tag{2.26}$$

Another important non-dimensional parameter is the Karlovitz number. It represents the ratio between the chemical time scale ($\tau_c \approx \alpha/s_l^2$) and the Kolmogorov time scale, e.g. if the fastest flame timescale is much smaller the turbulence timescale, the turbulence is not able to affect the flame structure. An alternative interpretation of the Karlovits number can also be done considering the

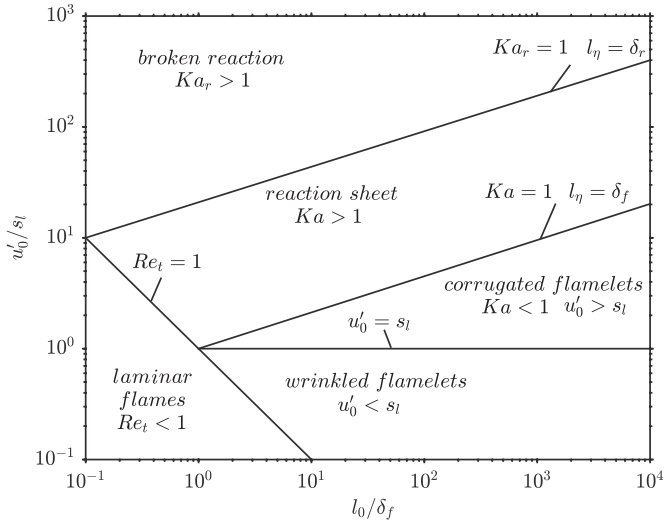

Figure 2.8: Borghi diagram, modes of turbulent premixed combustion

length scales. If the smallest turbulence length scale is bigger than the flame thickness, then turbulent mixing will not occur inside the flame and turbulence will not be able to affect the combustion process. The flame front will then result wrinkled because of the large turbulent length scales. On the other hand, when the Karlovitz number is small, the inner structure of the flame will be affected by small length scale eddies that will enhance the transport in the flame.

$$Ka = \frac{\tau_c}{\tau_\eta} = \frac{\delta_f^2}{l_\eta^2} = \sqrt{\frac{\delta_f}{l_0}\left(\frac{u'_0}{s_l}\right)} \tag{2.27}$$

It useful to define another Karlovitz number based on the thickness of the reaction zone or inner layer.

$$Ka_r = \left(\frac{\delta_f}{l_\eta}\right)^2 \left(\frac{\delta_r}{\delta_r}\right)^2 = Ze^{-2}Ka \tag{2.28}$$

Having defined these quantity, we can classify the different premixed combustion modes from the Borghi diagram, see figure 2.8.

- **Wrinkled flamelets** $u'_0 < s_l$ and $Ka < 1$. The flame thickness is much smaller then the Kolmogorov scale, the flame structure remains the same as a laminar flame but is embodied in a turbulent flow. This is known as laminar flamelet. Furthermore u'_0 can be seen as the turnover velocity of the large eddies, $u'_0 < s_l$ implies that the flamelet surface is only weakly wrinkled.

- **Corrugated flamelets** $u'_0 > s_l$ and $Ka < 1$. The flame still retain a laminar flame structure. However, being $u'_0 > s_l$ the extent of wrinkling is strong. More precisely it is of the same order of the eddy and the flamelets start folding. Eventually the folding of flamelets might break the flame front, leading to pockets of burned and unburned mixtures.

- **Thin reaction zone** $Ka > 1$, $\delta_f \simeq l_\eta$. The turbulent eddies are smaller than the flame thickness but still bigger than the reaction zone thickness. This causes the flame structure to be affected by turbulence only in the preheat zone. The smallest eddies in fact, penetrate the preheat zone of the flame and enhance heat and mass transfer rates. Indeed the the phenomenon is not only diffusion driven any more, turbulent mixing also plays a role. As a consequence the flame is broadened.

- **Broken reaction zone** $Ka_r > 1$. The smallest turbulent eddies are able to penetrate the reaction zone structure. This affecting both the diffusion and reaction processes. The temperature drastically drop and the flame extinguishes. Indeed the flame inner layer results is destructed by the small scales turbulent eddies. The flow now behaves like a well-stirred reactor and local flame structures are not present any more.

The above classification of regimes of combustion modes is based mostly on comparison of characteristic length and time scales. The boundaries, however, can be significantly modified by considering additional physics. The classification given by the Borghi diagram is made with many simplification. For instance in the discussion about wrinkled and corrugated flame, the vortex structure modification that can occur downstream of the flame front because fo thermal expansion has been neglected. Furthermore, regardless of its size, a vortex represent a disturbance to the flame and can trigger instability phenomena, such that hydrodynamic and thermo-diffusive instability. Triggering of these instability is length scale dependent, so the propensity to develop wrinkles is also a function of the characteristic size of an eddy. The discussion also assumed the flamelet to be stationary and passively distorted by the vortex. For these reasons figure 2.8 should only be seed as an attempt to capture the different premixed combustion regime and considered in its asymptotic limits, [34].

2.6.1. Turbulent flame speed

The turbulent flame speed is a very complicated quantity to measure. Considerable effort has been put in its experimental determination and it has been found that it can be drastically higher then the laminar burning velocity. Indeed it was explained in the previous section, section 2.6, that turbulence increase the flame surface and can also enhance the transport phenomena in the flame inner layer.
The laminar burning velocity has been defined through the continuity equation for a one-dimensional flame, see equation 2.4. We can also write the laminar mass burning rate of a flame as,

$$\dot{m}_l = \rho_u s_l A, \tag{2.29}$$

where A is the area. Before defining the turbulent flame speed we need to do a distinction based on the combustion modes considered in the Borghi diagram, see figure 2.8. We can, in fact, distinguish two regimes. In the first the flame is infinitely thin and just corrugated by turbulence (corrugated flamelets and wrinkled flamelets regimes). In the second one the inner layer or reaction zone is still very thin compared to the smallest eddies, it still basically retain a laminar structure, but the mixing in the preheat zone is highly affected by the vortex structure and is therefore turbulent mixing (thin reaction zone). We will consider this two regimes individually. In the first regime we can define the turbulent flame speed in analogy as it has been done with the laminar one.

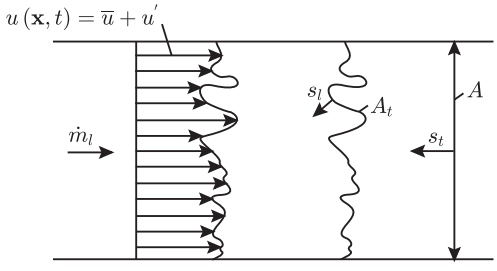

Figure 2.9: Turbulent flame front used to define the turbulent flame speed.

Let us consider figure 2.9, we can see an instantaneous velocity profile where the flame front propagates in the normal direction with a burning velocity equal to the laminar burning velocity.

The turbulent flame speed can be defined as the flame speed that an average flat flame front should have in order to have the same mass burning rate as the turbulent flame front, see figure 2.9.

$$\dot{m}_l = \dot{m}_t = \rho_u s_l A_t = \rho_u s_t A \qquad \rightarrow \frac{s_t}{s_l} = \frac{A_t}{A} \tag{2.30}$$

Where constant density in the unburned gas has been considered. From equation 2.30, is shown that the ratio of turbulent and laminar flame speed is the same as the ratio between the areas of the respective flame fronts. Wrinkling of the flame increases A_t and consequently it increases s_t. In order to asses the area ratio, Damkholer made an analogy with the laminar Bunsen flame. He noted that in a laminar Bunsen flame the burning rate is larger than the one that would characterize a corresponding flat flame. Higher burning rate means that the area of the flame cone angle has to be bigger and consequently, the flame cone angle is narrower. So the assumption is that the area ratio between a laminar and turbulent flame is related to the velocity turbulent fluctuations in the following way,

$$\frac{s_t}{s_l} = \frac{A_t}{A} = 1 + \frac{u^{'}}{s_l}. \tag{2.31}$$

In this regimes (corrugated and wrinkled) the chemistry does not play a role in modifying the turbulent flame speed.
The situation is different in the case of the thin reaction zone regime. Based on scaling argument the flame speed is depending both on the diffusion process in the preheat zone and on the chemistry in the reaction zone. The thermal diffusion in this case is not laminar any more but is driven by turbulence, α_t, while the chemical time scale τ_c remains the same, since the inner layer retains the same structure of a laminar flame, [45].

$$s_l \sim \sqrt{\alpha/\tau_c} \rightarrow \frac{s_t}{s_l} \approx \sqrt{\frac{\alpha_t}{\alpha}} \tag{2.32}$$

From dimensional analysis also emerges that, in this thin flame regime, turbulent diffusion scales with turbulence fluctuations and flame thickness. As a consequence the turbulent burning velocity can be expressed as $s_t \approx \sqrt{u^{'}\delta_f}$. This relation captures the effect of length scale.

3

Literature review

In this section of the thesis, after a brief introduction about the different flashback phenomena, boundary layer flashback (BLF) will be considered in detail. In particular the main parameters affecting this instability onset, will be considered. Recent experimental advancement and more classic approaches like the critical velocity gradient model will be discussed.

3.1. Flashback Phenomenon

A flame in premixed conditions is said to be stable when the velocity at which fresh mixture is fed to the flame is in balance with the kinetics of the flame. In contrast to a stable configuration, there are limiting flow and flame conditions below or above which a stable flame can not exist. When the incoming fresh mixture is too fast with compare to the kinetics of the flame there is not enough time for the combustion to take place and blow-off occurs. On the other hand, flashback occurs when the characteristic velocity at which combustion happens is quicker than the rate at which the fresh charge is supplied. As a consequence, the flame propagates upstream. When this phenomenon happens in a combustor for instance, the flame travels upstream from the combustion zone, where is designed to be anchored, into the premixing section advecting heat that can cause severe damages. The main flashback mechanisms are core flow flashback, combustion instability induced flashback, combustion induced vortex breakdown and boundary layer flashback, Kalantari et al. [31].

3.1.1. Core flow flashback

This flashback mechanism occurs when the axial flow velocity is smaller than the laminar or turbulent burning velocity. The turbulent velocity is a function of chemical kinetics and turbulent flame-flow interaction [12, 31]. In a combustor, core flashback can be prevented by increasing the axial flow velocity. In order to stabilize the flame in a wide operational range, aerodynamics stabilization techniques, such as recirculation zones, are commonly employed in a typical combustor design. Swirl adoption to stabilize the flame has two effect, both enhancing core flashback tendency. The first is that the swirl causes higher flame front wrinkling and consequently the turbulent flame speed increases [12], while the second is that high swirl also reduces the local axial velocity.

3.1.2. Combustion induced vortex breakdown (CIVB)

This flashback mechanism is often encountered in gas turbine combustor and is specific to swirl-stabilized burners, Benim et al. [8]. Flames in gas turbines combustor are often stabilized by means of swirled flows. As a consequence of swirled-flow, vortex breakdown occurs and a recirculation zone arises on the burner axis. Thanks to this effect it is possible to anchor the flame slightly up-

stream of the stagnation point, where the turbulent flame speed equal the axial velocity. At flashback onset, the combustion process alters the combustor flow field in such a way that the vortex breakdown bubble is able to move upstream from the outlet region into the premixing section of the combustor.

3.1.3. Combustion instability induced flashback

Combustion instabilities produce fluctuations in the flow field that can lead to flashback [31, 53]. Instabilities can be driven by unsteady heat release, acoustic mode interaction and change in the flow field. In premixed systems we can distinguish two main mechanism for instabilities generation, equivalence ratio fluctuations and the vortex shedding. In the former mechanism, acoustic mode interactions in the premixer can cause equivalence ratio fluctuations, which then leads to a change in the flame composition, flame temperature, flame speed and heat release. The vortex shedding mechanism is related to the large scale interaction of vortical structures that can distort the flame front and lead to heat release variation [8].

3.1.4. Boundary Layer Flashback (BLF)

Boundary layer flashback mechanism is typical flashback mechanism of jet-Bunsen flames. During normal operating conditions, the unburned gas velocity is higher than the flame speed, so core flashback cannot occur in these burners. However, moving from the axis of the burner to the wall the velocity decreases approaching the boundary layer, and it reaches zero at the wall, where the no slip boundary condition is imposed. Also the burning velocity is affected by the wall and at a certain distance from it, called quenching distance, the flame is not able to sustain itself and the burning velocity goes to zero. This happens because of radicals quenching and heat loss to the wall, [7, 23].

3.2. Boundary layer flashback

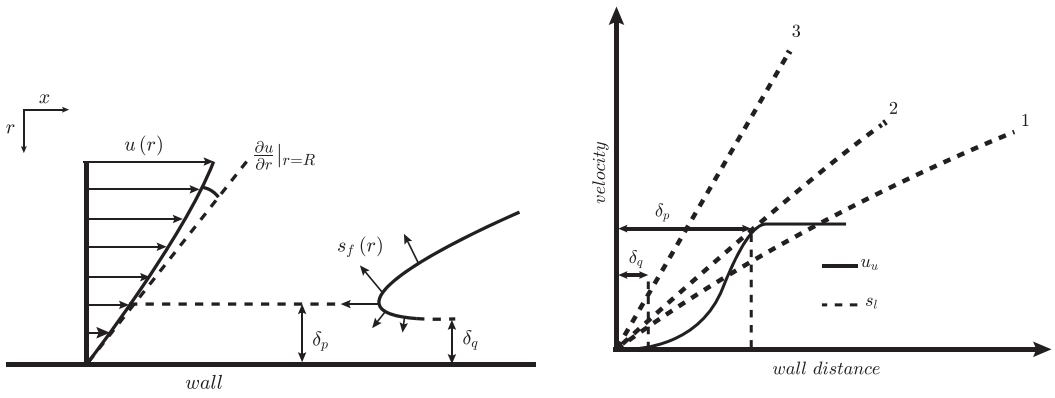

(a) Schematic of the critical velocity gradient model, reproduced from [31].

(b) Flow velocities and flame speed profiles at flashback conditions.

Figure 3.1: (a) Schematic of the critical velocity gradient model, reproduced from [31]. (b) Flow velocities and flame speed profiles at flashback conditions, reproduced from [31].

In the 40s and 50s many studied about boundary layer flashback (see figure 3.1a) have been carried out, the critical boundary gradient model was proposed by Lewis and Von Elbe in 1943, [35]. Some flashback experiments about turbulent boundary layer flashback were performed by Edse [14], preheat temperature and tip temperature were investigated by Grumer and Harris [25] and [9]. More recent developments, related to the energy transition challenge, renewed the interest for boundary layer flashback. In particular, the focus has moved to H_2 and H_2/DNG mixtures. Predictions models for both confined and unconfined flame configurations, as well as some detailed

PIV and OH chemiluminescence experiments have been carried out by the Technical University of Munich (TUM) research group, in particular these papaers provide detailed information about their findings, [28], [17], [5]. A research group at the Paul Scherrer Institute in Switzerland investigated turbulent flames flashback at gas turbines conditions, and proposed a model where flame speed is used as a flashback propensity indicator [37]. Hydrogen boundary layer flashback has also been investigated at the University of California, Irvine (UCI). Kalantary developed an experimental correlation to include the effects of preheat temperature, operating pressure and tip temperature, [32].

3.2.1. Critical velocity gradient model

This model is the first attempt to describe the boundary layer flashback event of laminar flames, [35]. The main assumption of the model is that the flame and the flow do not interact. As a result, the laminar flow velocity profile is undisturbed and known from the analytical solution. Furthermore, to describe the flame characteristics the one-dimensional flame propagation is considered.
Figure 3.1a shows a scheme of the critical velocity gradient model. The laminar flow velocity profile $u(r)$ is approaching the flame front that is represented by the flame speed profile $s_f(r)$. The burning velocity profile $s_f(r)$ is decreasing approaching the wall because of heat loss and quenching of radicals [7]. At a certain distance from the wall, quenching distance (δ_q), the combustion reaction is not able to sustain itself any more and the flame extinguishes. Figure 3.1a also shows the penetration distance (δ_p) that is defined as the distance from the wall at which the local unburned gas velocity equals in magnitude the flame speed. Line (2) in figure 3.1b shows the conditions at which flashback can occur. Indeed, if the flow velocity drops, at the distance δ_p form the wall, the flame speed outbalance the flow velocity and the flame flashes back, see curve (1) figure 3.1b. On the contrary, if at δ_p the flow velocity increases the flame is pushed downstream out of the tube, see curve (3).
The model predicts flashback event by comparing the flow velocity gradient at wall with the ratio between laminar flame speed and penetration distance. Under the assumption of laminar and fully developed pipe flow, the velocity profile can be analytically described by equation:

$$u(r) = 2U_b\left(1-\left(\frac{r}{R}\right)^2\right). \tag{3.1}$$

Computing the derivative of the velocity profile at the wall equation 3.2 is obtained.

$$g_c = \left|\frac{\partial u}{\partial r}\right|_{r=R} \tag{3.2}$$

Assuming that in the wall proximity the velocity profile is linear, we can write g_c as the ratio between the flow velocity and the penetration distance, equation 3.3.

$$g_c = \frac{u|_{y=\delta_p}}{\delta_p} \tag{3.3}$$

Under flashback onset critical conditions, at the penetration distance the velocity profile and flame speed are the same. Furthermore the flame speed value can be assumed equal to the unstreched laminar flame speed, $s_{l,0}$ [35], which can be computed under one-dimensional steady flow assumption. Equation 3.3 can then be written as:

$$g_c = \frac{s_{l,0}}{\delta_p}, \tag{3.4}$$

it follows then

$$g_c = \frac{s_{l,0}}{\delta_p} = \frac{4U_b}{R}. \tag{3.5}$$

From equation 3.5, we can see that the impact of the fuel on flashback propensity is included in its flame speed and penetration distance. The penetration distance is not fully described in the model

and needs indeed to be determined in order to predict flashback propensity of different fuel compositions, see Kalantari et al [31]. The penetration distance, according to Wohl [65], which studied the characteristics distances relevant to flashback and blow off in nozzles and tubes, is proportional to the quenching distance δ_q and the flame thickness δ_f. Different approach to select the right penetration distance have been proposed, [31]. For instance one of them is based on the conclusion of Wohl [65] and express the critical velocity gradient as a function of the quenching distance δ_q:

$$g_c = C\frac{s_{l,0}}{\delta_q} \quad . \tag{3.6}$$

The critical velocity gradient for laminar flames, developed by Lewis and Von Elbe [35], has also been extensively employed to characterize turbulent flames flashback. The use of this model has been justified by the assumption that the turbulent flame flashback occurs in the viscous sublayer ($y^+ < 5$) where the velocity profile is linear, [31]. The critical velocity gradient for turbulent flames, as for the laminar case, is based on the equality of the burning flame speed and the flow velocity at a distance from the wall identified by the penetration distance (δ_p). The flame speed, $s(f)$, is still considered to be similar to the unstreched laminar flame speed $s_{l,0}$ and calculated considering the one-dimensional steady flow assumption.

$$g_c = \frac{u|_{y=\delta_p}}{\delta_p} = \frac{s_{l,0}}{\delta_p} \tag{3.7}$$

For what concerns the unburned gas velocity profile the Bluausis correlations for fully developed turbulent flow in smooth pipe is used, [64].

$$f = \frac{0.3164}{Re^{0.25}} \quad ; \qquad 4000 < Re < 10^5 \tag{3.8}$$

$$g_c = \frac{1}{8}\frac{fU_b}{\nu} \tag{3.9}$$

$$g_c = 0.03955\, Re^{0.75}\frac{U_b}{d} \tag{3.10}$$

where f is the friction factor and ν the kinematic viscosity. Combining equation 3.7 and 3.10 the flashback criteria for turbulent flames follows:

$$\frac{s_{l,0}}{\delta_p} = 0.03955\, Re^{0.75}\frac{U_b}{d}. \tag{3.11}$$

Similarly, as for laminar flames, the undetermined penetration distance is considered proportional to the flame thickness $\delta_p \simeq \delta_f$.
The critical velocity gradient model is capable of correlating the flashback propensity for laminar flames and, under certain conditions also the flashback propensity of turbulent flames, [31]. However it has been experimentally shown by Baumgartner et al. [5], that flashback is not occurring in the viscous sublayer of the inner flow, as a consequence, to consider the velocity profile linear at the flashback location is a wrong assumption. Furthermore the critical velocity gradient model neglects the flame-flow interaction and the flame speed dependency on other effects, e.g. flame stretch. As a consequence of these simplifications, the model is not able to explain how the flashback phenomenon occurs.

3.3. Parameters affecting boundary layer flashback

Boundary layer flashback is a complex phenomenon affected by many parameters which are coupled one another. In order to explain the interaction of these parameters and review some experimental results, they have been divided in three main groups:

- Confined, unconfined flames and boundary layer heating
- Burner material, tip temperature and diameter
- Operating pressure and temperature

This classification is based on the work of Kalantary et al. in their boundary layer flashback review paper, [31].

3.3.1. Confined and unconfined flames

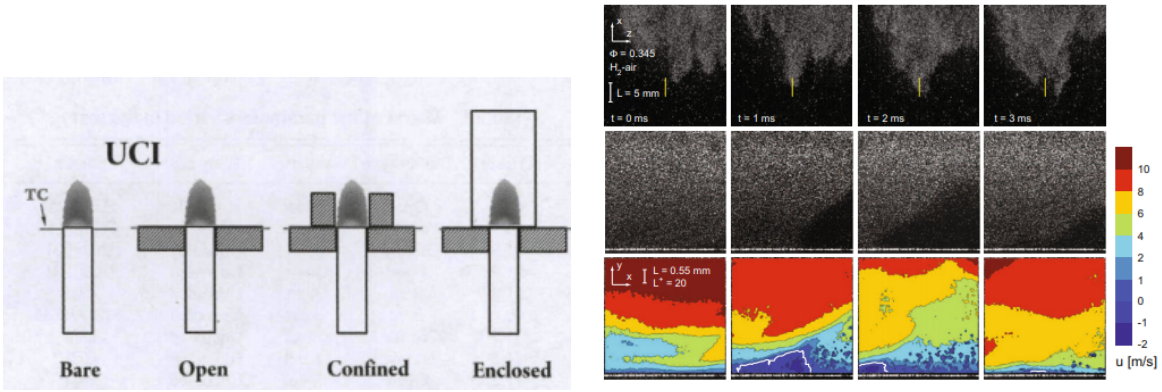

(a) Different flame configurations, image taken form [55]

(b) Micro-PIV, Mie-scattering and velocity contour of hydrogen flame flashback in the wall region in a confined channel burner configuration, image taken from [16]

Figure 3.2: (a) Different flame configurations, image taken from Shaffer et al. [55]. (b) Micro-PIV, Mie-Scattering and velocity contour of a lean hydrogen flame in a confined channel burner, image taken from Eichler et al. [16].

Figure 3.2a shows different flames configurations. In an enclosed or confined configuration the flame also interacts with the surrounding walls. Moreover when the flame is confined it already exists in the boundary layer. In particular in this thesis turbulent boundary layer flashback in bare tube burner configuration has been investigated.

Unconfined flames. An unconfined flame configuration is the one in which there is the free injection of the reactants mixture in ambient air, like for instance the case of jet flames. An experimental investigation has been carried out by Baumgartner et al. [6]. They tried to asses how flame-flow interaction affects hydrogen flame boundary layer flashback in the case of unconfined flame. To do so they have considered a high aspect ratio channel flow to resemble a 2-D flow. Furthermore, the experiments have been carried out at atmospheric pressure and utilizing PIV, Mie-scattering and OH* chemiluminescence. Figure 3.3b shows the axial velocity contours in correspondence of flashback onset and propagation. Streamlines are shown in white, while the black dotted curve represented the approximate location of the flame front extracted from the Mie-scattering images. As the flashback phenomenon is approached the leading edge of the flame starts to propagate upstream. While travelling upstream, the flame leading edge decelerates the approaching flow. This feedback process allows the leading edge to slowly travel upstream until its able to flashback inside the burner. Figure 3.3a shows the schematic time evolution of the transient phenomenon. In particular, the distance through which the streamline passes by is in the range between $y^+ = 13$ and $y^+ = 21$, which does not coincides with the viscous sublayer region where the critical velocity gradient holds, but instead is localized in the buffer layer. The conclusions of this investigation is that however there is an interaction between the flame and the flow, it is weak. This is the reason why even though the critical velocity gradient model is not able to explain the physical process through which the phenomenon happens it is still able to predict some data in literature.

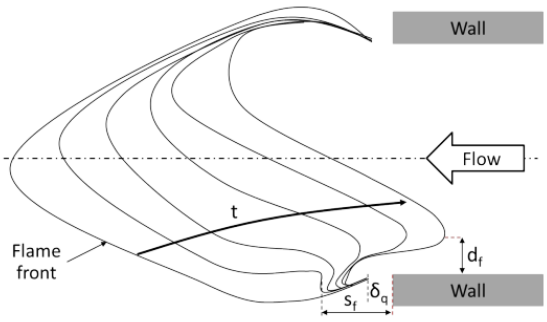

(a) Schematic illustration of the transient mechanism, from stable to unstable flame, image taken form Baumgartner et al. [6]

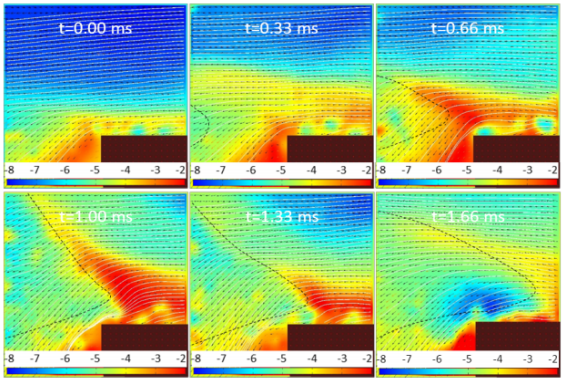

(b) Time evolution of the axial velocity field during upstream flame propagation, the black dashed line indicates the approximate shape of the flame leading edge, image taken form Baumbartner et al. [6]

Figure 3.3: (a) Schematic illustration of the transient mechanism, from stable to unstable flame, image taken form Baumgartner et al. [6]. (b) Time evolution of the axial velocity field during upstream flame propagation, image taken form Baumbartner et al. [6].

Confined flames. Eichler and Sattelmayer [16] investigated confined flames boundary layer flashback by means of micro-PIV, Mie-scattering and OH* chemiluminescence. This investigation was done since in a previous work, [17], was found the important role of flame-wall interaction and the inability of the critical velocity gradient model to capture the phenomenon dynamics. Thus, focus of the investigation was the flame-flow interaction in the near wall region at flashback onset conditions. Figure 3.2b shows OH* chemiluminescence on the first row, Mie-scattering along the second and velocity contour images on the third. It shows how, flames wrinkles turn into cusps. They then can either travel upstream, downstream or stay at the same location. Furthermore some of these cusps divided into smaller ones. The bulges able to travel upstream are the ones responsible for flashback. In the confined flame configuration the flame-flow interaction is very strong. Indeed the adverse pressure gradient related to thermal expansion strongly affects the approaching flow, that

is retarded and deflected. Furthermore, this effect coupled with the low velocity streaks in the turbulent flow field enhance the flame flashback.
Gruber et al. [24] performed a direct numerical simulation (DNS) of boundary layer flashback in a fully developed turbulent channel flow. They observe the creation of flame cusps. In particular Gruber et al. [24] observed that high speed sweeps lead to the convex flame region towards the products, while low speed ejections lead to bulges formation which are convex towards the reactants. This mechanism is caused by the Darrius-Landau instability, which was presented in section 2.4 in the previous chapter. The Darrius Landau instability lead to an adverse pressure gradient in correspondence of the flame front which then is responsible for the flame flow interaction.

3.3.2. Burner material, tip temperature and diameter

In this paragraph, unless explicitly indicated, the presented results are related to the unconfined flame configuration.

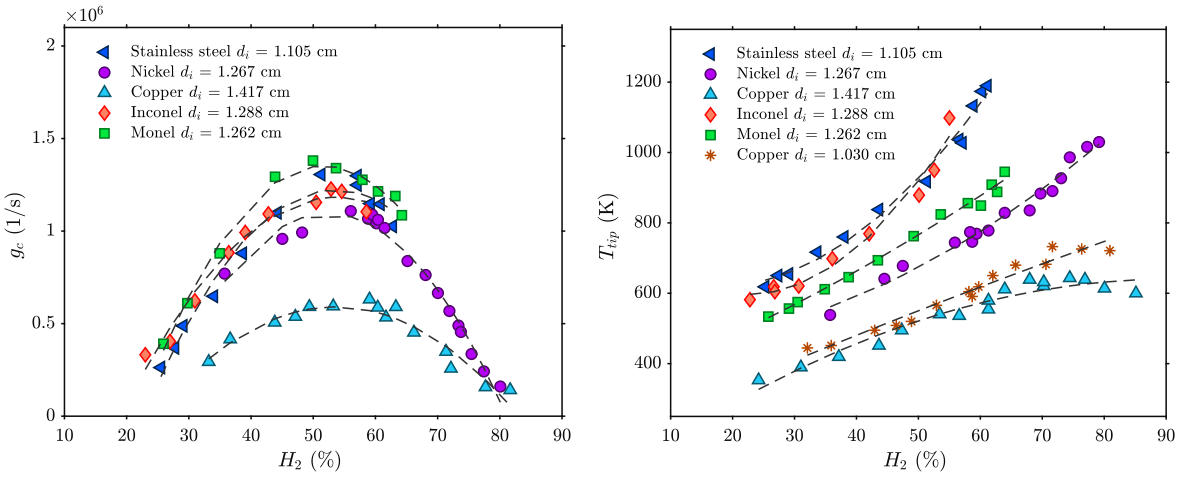

(a) Critical velocity gradient as a function of hydrogen concentration for burners made of different materials, reproduced form [9]

(b) Tip temperature as a function of hydrogen concentration for burners made of different materials, reproduced form [9]

Figure 3.4: (a) Critical velocity gradient as a function of hydrogen concentration for burners made of different materials. (b) Tip temperature as a function of hydrogen concentration for burners made of different materials.

Bollinger and Edse [9], investigated the effect tip temperature burner material, burner diameter, tube and wall thickness on turbulent boundary layer flashback of hydrogen/oxygen flames at atmospheric pressure. Flashback conditions are approached in a quasi-steady process. Indeed, it has been observed that if flashback is not approached sufficiently slow to ensure thermal equilibrium between the burner tip and the flame front, the event propensity can be significantly different. Figures 3.4a and 3.4b show the effect of the burner material and of the tip temperature on critical velocity gradient, for a constant burner thickness. The lower flashback propensity associated with the copper burner can be related to its lower tip temperature. Burner tip temperature depends on the heat balance between the flame, the burner, the heat loss to the surrounding air and the incoming reactants flow. Higher is the thermal conductivity of the burner, higher is the heat conduction across the the tube walls cross sectional area and lower is the tip temperature. Different thermal conductivity and tip temperature, however, are not enough to explain the difference in critical velocity gradients in the case of stainless steel, Monel and Inconel which are characterized by similar thermal conductivity.
Shaffer et al. [54] and Duan et. al [13] performed experiments to asses the fuel composition, burner material, tip temperature effects on flashback for confined tube combustors at turbulent flow con-

ditions. Different mixtures of hydrogen, carbon monoxide and methane have been considered. The flow was fully developed and the flashback event was induced at two constant adiabatic flame temperatures, 1700 and 1900 K respectively. Furthermore the experimental conditions were ambient pressure and room temperature. Shaffer et al. [54] in accordance with Duan et. al [13], shown that high hydrogen concentration fuels are more prone to flashback. It also noted that adding CO to H_2 reduces linearly the laminar flame speed, while when CH_4 is added to H_2 it diminishes exponentially in accordance with the findings of Huang et al. [30].
Duan et al. [13] studied flashback limits for hydrogen/air unconfined jet flames. Experiments, conduced at atmospheric pressure and ambient air temperature, addressed burner material and tip temperature, flame confinement and burner diameter effects. It was found that burner material,tip temperature, flame confinement, have strong effect on flashback propensity, while burner diameter effects are negligible. The proposed explanations refer mainly to the tip temperature and different thermal conductivity of the considered burners. In particular when the difference in flashback propensity between an enclosed and open configuration of quartz and stainless steel tube are compared, emerges that the quartz burner shows a bigger difference in flashback propensity. This is mainly related to how quartz, characterized by lower thermal conductivity, affects the boundary layer heating. For what concerns confined flame configuration, figure 3.5b shows that, regardless of burner size and material, flashback propensity is drastically higher. These findings are in agreement with [17]. Furthermore flashback mechanism has been observed to be different for confined flames, being the flame-flow interaction strongly affecting the instability event, [16]. From figure 3.5b also emerges that active cooling of the combustor reduced flashback propensity. Finally effect of the diameter on turbulent boundary layer flashback has been found to be weak, also this observation is consistent with some previous finding from Khitrin et al. [33], see figure 3.5a.

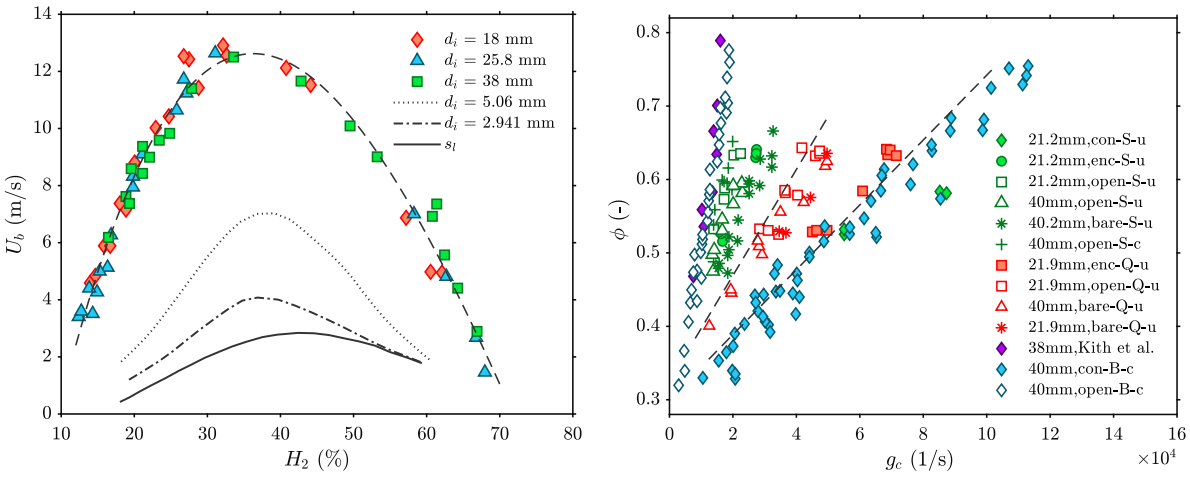

(a) Turbulent (solid curve), reproduced from [33], and laminar (dashed curves) hydrogen flames flashback propensity.

(b) Critical velocity gradient results summary for different burner configurations, materials and diameters, reproduced form [13].

Figure 3.5: (a) Turbulent and laminar hydrogen flames flashback propensity. (b) Critical velocity gradient results summary for different burner configurations, materials and diameters.

Eichler and Sattelmayer studied boundary layer flashback of methane/hydrogen air in a channel, [15]. Results were presented in terms of critical velocity gradient and compared literature data available for tubes. The comparison shows significantly different results, mainly related to the different flame configurations for both channel and tubes burners. To further investigate these differences, Eichler [17] performed some more experiments with both a setup similar to the channel (confined) and tubes (confined and unconfined). Form the results the main differences in flashback propensity seems again to be related to flame configuration and not to the geometry of the two con-

sidered combustors.
To summarize, thermal coupling between burner tip temperature and the flame front is crucially important. The burner rim temperature and more in general the combustor temperature are affected by the material thermal conductivity, they might lead to boundary layer heating and consequently increase flashback propensity. The presence of an enclosure increases tip temperature. Furthermore, if the enclosure size is reduced, tip temperature gets even higher since heat loss to ambient air and the entrainment of the fresh oxidizer are both reduced.

3.3.3. Operating pressure and temperature

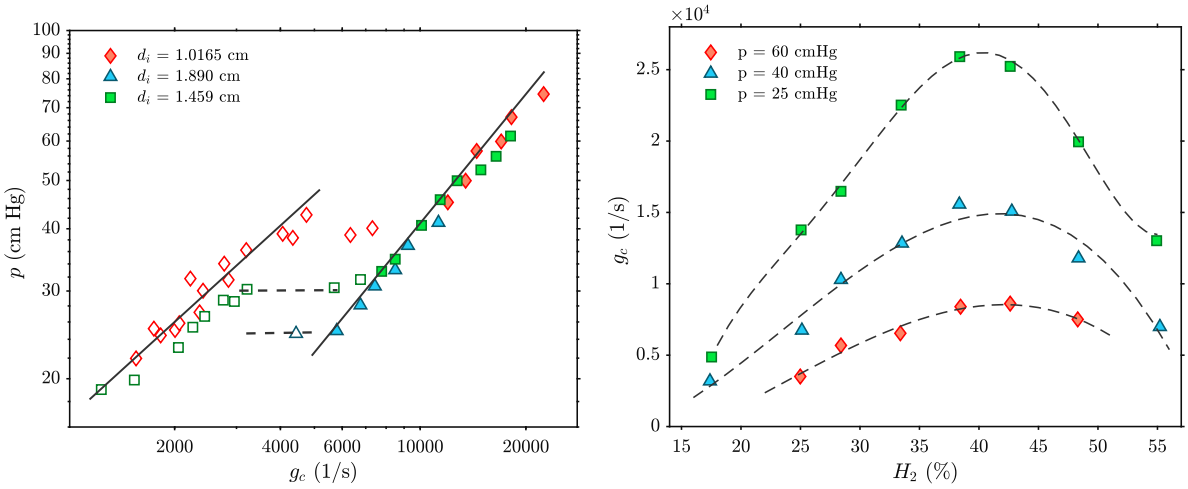

(a) Critical velocity gradient of hydrogen/air mixture as a function of pressure at ϕ =0.95, reproduced from [19].

(b) Critical velocity gradient of turbulent hydrogen/air flame as a function of fuel percentage at different pressures, reproduced from [19].

Figure 3.6: Critical velocity gradient of hydrogen/air mixture as a function of pressure (a) and as a function of fuel percentage at different pressures (b), reproduced by [19].

Fine [18, 19] investigated the effect of sub-atmospheric pressure on flashback propensity of hydrogen flames for laminar, transitional and turbulent conditions. Figure 3.6a shows the critical velocity gradient variation, for hydrogen air mixtures, as a function of pressure at a fixed equivalence ratio (ϕ = 0.95). The critical velocity gradient changes exponentially with increasing pressure. Furthermore, its rate of change is almost constant for both the laminar and turbulent flames and it is independent of the burner diameter. Since the ratio between laminar and turbulent burning velocity is not big, Fine [18, 19] proposed that the change in critical velocity gradient it is not only due to the change in burning velocity due to pressure but also to the change in penetration distance. Figure 3.6b shows the change in critical velocity gradient for different hydrogen concentration in the fuel-air mixture. As the pressure is increased the velocity gradient curve shifts to higher value showing an increased propensity to flashback. Furthermore, the rate of change of the critical velocity gradient as we move from lean conditions to rich conditions is bigger at higher pressures. Finally, the peak for each curve shown in figure 3.6a remains similar at the same equivalence ratio, emphasizing that the critical velocity gradient is related to the reaction rate.
Fine,[20], analysed the effect of preheat temperature and sub-atmospheric pressure on flashback propensity of an air hydrogen mixture at a constant equivalence ratio. Figure 3.7 shows the results. It can be seen that the rate of change of critical velocity gradient with preheat temperature is independent of pressure. Indeed the angular coefficients of the two lines in figure 3.7 have almost the same value.

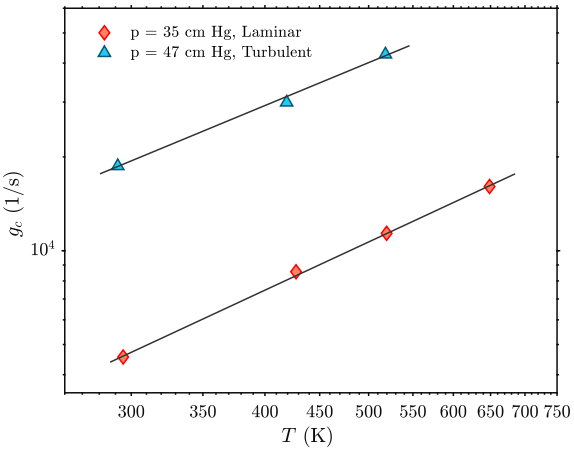

Figure 3.7: Critical velocity gradient as a function of preheat temperature at two different pressures, reproduced from [20]

4

Experimental set-up and methodology

This chapter starts with a description of the TU Delft combustion facility used to carry out this research. Subsequently, the flow measurement technique is presented. Finally, the different experiments conditions, settings and procedure are defined and explained.

4.1. Experimental Combustion facility

Figure 4.1 shows a schematic of the experimental facility. The combustion lab is equipped with several gas lines, that can be connected to the burner. In this research the air, hydrogen and DNG lines are used and, each line is equipped with theirs mass flow controller. A UV safety sensor is also highlighted in the schematic. This device acts as flame detector inhibiting the fuel flow when combustion is not taking place.

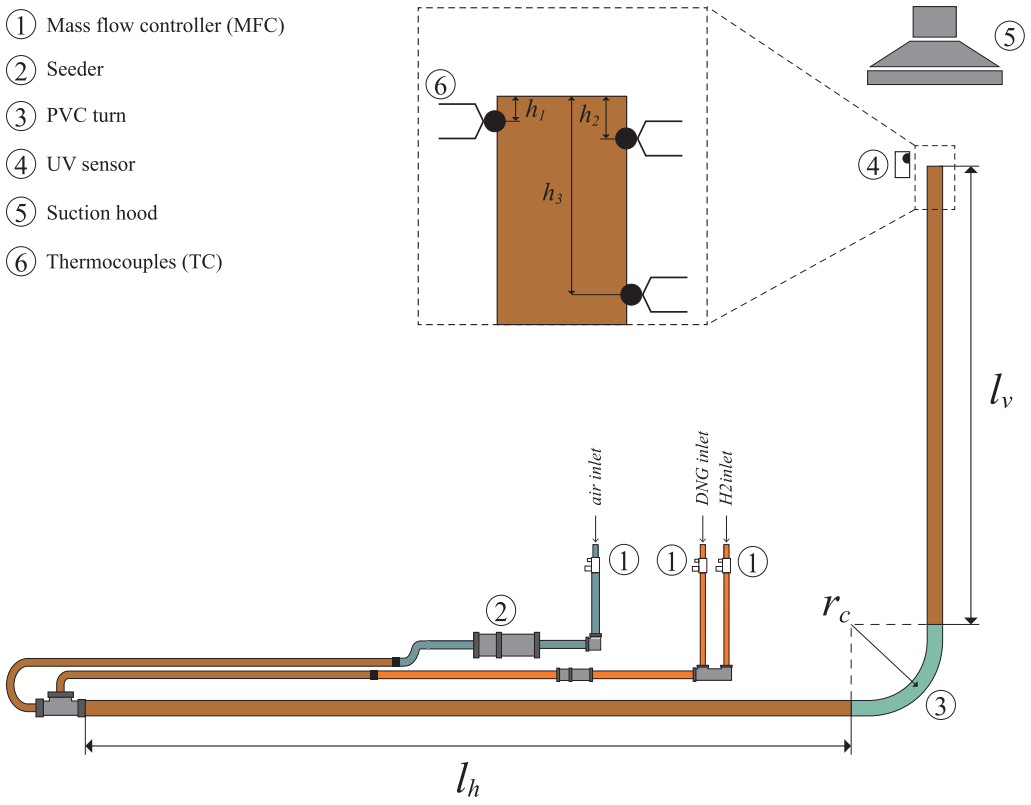

Figure 4.1: Schematic of the combustion facility with tube burner.

4.1.1. Burner geometry

Experiments have been carried out on simple copper tube burners. Three different tubes have been used in order to obtain a fully developed turbulent flow, characterized by a Reynolds number of about 10^4. As illustrated in figure 4.1 each tube burner consists of three sections: one horizontal with length l_h, a 90 ° bend with radius r_c and a vertical section of length l_v. Except for the turn, which consist of PVC, the burners are made of copper. Initially, the burners consisted of the vertical part only, but later the horizontal section and the turn were added to increase the effective length over diameter ratio. Further information on the fully developed flow conditions and their characterization are given in the 'flow validation' section 5.2. Table 4.1 lists the tube internal diameters d_i, lengths of the horizontal and vertical sections l_h and l_v, wall thicknesses t_h, radii of the bends r_c, material and length over internal diameter ratio l/d_i. The burner tubes inner diameters have been measured by means of a three point inner micrometer. Moreover all the three burners are characterized by a flat tip.

Burner tube 1	Vertical tube	Horizontal tube	Turn
Internal diameter, d_i (mm)	20.06 ± 0.04	20.06 ± 0.04	
Thickness, th (mm)	1	1	
Length, l (mm)	1250	1450	
Length to diameter ratio, l/d_i (-)	62.3	72.3	
Radius of curvature, r_c (mm)			85
Material	copper	copper	PVC
Burner tube 2	Vertical tube	Horizontal tube	Turn
Internal diameter, d_i (mm)	25.67 ± 0.01	25.67 ± 0.01	
Thickness, th (mm)	1.1	1.1	
Length, l (mm)	1260	2400	
Length to diameter ratio, l/d_i (-)	49	93.5	
Radius of curvature, r_c (mm)			88
Material	copper	copper	PVC
Burner tube 3	Vertical tube	Horizontal tube	Turn
Internal diameter, d_i (mm)	39.20 ± 0.01	39.20 ± 0.01	
Thickness, th (mm)	1.4	1.4	
Length, l (mm)	1270	2110	
Length to diameter ratio, l/d_i (-)	32.5	54	
Radius of curvature, r_c (mm)			177
Material	copper	copper	PVC

Table 4.1: Specification of the tube burners employed in the experiments.

4.1.2. Cooling jacket and thermocouples

The most downstream part of the tube burner is equipped with a cooling jacket as illustrated in figure 4.2. Thermocouples of type J and K were used to monitor the burner tip temperature. The insert in figure 4.1 shows the location of the thermocouples on the tube. The type K thermocouple is a self-adhesive polyimide sensor, with an operating temperature range of -40°C to 250 °C. It has been selected because, thanks to its small size (6.7 mm wide × 0.13 mm thick × 107 mm long), it can be placed close to the burner rim without affecting the flow field. Type J thermocouples were used to check that the temperature distribution in the burners was steady. Their operating range is between -40°C to 750 °C. Figure 4.1 shows where the thermocouples (denoted by TC1, TC2 and TC3) were

located. TC1 is at distance h_1 = 2 mm, TC2 at h_2 = 10 mm and TC3 at h_3 = 90 mm from the burner tip. TC1 (type K) has been used to measure the tip temperature, TC2 (type K) to see the temperature distribution in the tube and check for TC1 measurement. Finally, TC3 (type J) was used to check the correct execution of the experiment. This is explained in more detail in the next section about experimental program and methodology 4.3.
Each tube burner is equipped with a cooling jacket. Since flashback propensity is strongly dependent on the rim temperature, these water cooling jackets allowed to compare flashback propensity of flames characterized by different adiabatic flame temperatures, flow rates and thermal power. Figure 4.2 shows one of the employed jackets. The jackets have a cylindrical shape and have been installed by scrolling them from the top of the burner. Tap water at a temperature of about 15 °C has been used for cooling.

Figure 4.2: One of the cooling jackets installed on a tube burner. Tap water enters from the bottom and leaves from the top to avoid air accumulation in the device.

4.1.3. Mass flow controller (MFC)

Hydrogen, air, and DNG mass flow controllers, manufactured by Bronkhorst were used, see figure 4.1. They consist of a flow meter and a control valve, Bronkhorst provides detailed MFC datasheet, e.g. the hydrogen one can be found here [1]. The manufacturer declares an uncertainty of 0.1% with to respect to the full scale (FS), plus an uncertainty of 0.5 % of the flow rate reading (RD). When the mass flow controllers are used in a lower range of their capacity the uncertainties is in percentage higher.
The flow is measured in normal liters per minute which is actually a mass flow unit even though it looks like a volumetric flow unit. The reference normal conditions are a pressure of p_n = 1013.25 mbar and a temperature of T_n = 0 °C. All the experiments have been conducted at atmospheric pressure and a correction to obtain the actual flow rate from the normal liter per minute to liter per minute has been done on the temperature only, by means of the ideal gas law. The actual flow rate Q_{actual} (in liter per minute) is then given by

$$Q_{actual} = Q_{reading}\left(\frac{p_n}{p}\right)\left(\frac{T}{T_n}\right) \tag{4.1}$$

where $Q_{reading}$ is the flow rate reading measured in normal liter per minute, p is the lab pressure, T is the lab temperature while p_n and T_n are the pressure and temperature at normal conditions.

4.2. Flow measurement technique

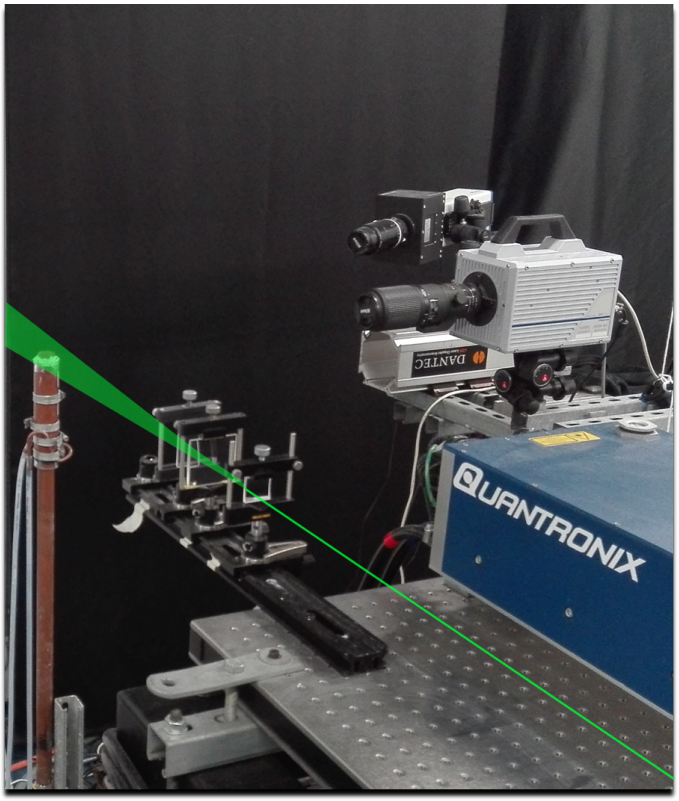

Figure 4.3: Photograph depicting the main components of the PIV system, i.e., the camera (1), the laser light source (2) and the light sheet optics (3). The tube burner is visible on the left and the laser light sheet is also drawn in the photo.

4.2.1. Planar Particle Image Velocimetry

Particle Image Velocimetry (PIV) was used to obtain quantitative and qualitative data on the velocity fields. PIV is a non-intrusive technique that measures the instantaneous velocity field in a planar cross section of the flow. Figure 4.3 shows the main components of the PIV setup. The laser beam with green light at 527 nm wavelength passes through a series of lenses which create a vertical light sheet (with a thickness of approximately 1 mm) that finally cuts the tube burner outlet along a plane. The camera is located perpendicular to the laser sheet.

The flows of air and fuel were seeded separately with a dedicated cyclone seeder. Once seeded, the flows are mixed before entering the burner. The seeding consists of Aluminum-oxide particles (Al_2O_3), with a mean diameter of about 1 μm and a density of 3200 kg/m^3. The dynamical characteristic of a particle determine its ability to follow fluid velocity fluctuations. A simplified equation that describes the motion of a spherical rigid particle in a viscous flow is given by Somerscales [57], equation 4.2. It has been obtained by assuming high particle to fluid density ratio.

$$\rho_p \frac{\pi d_p^3}{6} \frac{du_p}{dt} = 3\pi\nu\rho_f d_p \left(u_f - u_p\right) \quad , \tag{4.2}$$

where ν is the fluid kinematic viscosity, d_p is the particle diameter, u_f and u_p are the fluid and particle velocity, and ρ_f and ρ_p are the densities of the fluid and particle respectively. The equation

describes the balance between the force which accelerates the particle (left-hand side) and the viscous drag (right-hand side), expressed by Stokes' drag law. Equation 4.2 is valid under the following assumptions. (1) low particle Reynolds number, $\mathrm{Re}_p = V d_p/\nu_f < 1$, where V is the relative velocity between the particle and the fluid, i.e., $(V = u_p - u_f)$. (2) the fluid is incompressible and of infinite extent. (3) there is no slip between the particle and the fluid at the particle's surface. (4) the particle is spherical, infinitely rigid.Equation 4.2 can then be integrated to yield rewritten as 4.3 and integrated.

$$u_p = u_f e^{-\frac{18\mu_f}{\rho_p d_p^2} t} = u_f e^{-\frac{t}{t_0}} \quad \text{where} \quad t_0 = \frac{\rho_p d_p^2}{18\mu_f}. \tag{4.3}$$

The quantity t_0 is known as particle relaxation time. It indicates the time required for a particle to adjust to change in the velocity of the surrounding fluid. In order to evaluate the seeding particles tracers behaviour the Stokes number (Stk) has to be considered. According to Tropea [11] a particle behaves like a tracer when the Stokes number Stk << 0.1. Stk is defined as

$$Stk = t_0 \cdot \frac{u_0}{l_0}. \tag{4.4}$$

It relates the particle relaxation time to a flow time scale. In order to follow the smallest eddies which characterize the flow, the Stokes number should be computed considering the particle relaxation time and the Kolmogorv time scale η_K. Considering a simplification of the integral flow time scale d/U_b a typical Stokes number which characterizes the investigated flow has been calculated Stk = 0.0046. This is indeed much smaller then 1, however the fact that a particle is able to follow the large-eddy turnover time does not guarantee that it is also able to follow the small-eddy one.
The PIV system uses a Quantronix Nd:YLF dual-cavity laser type Darwin-Duo Pro527-80-M. The 527 nm wavelength laser beam generated by the laser is transformed into a laser sheet by passing the Gaussian beam through a series of optical components, specifically three plano-concave cylindrical lenses. The laser sheet illuminates the seeding particles just above the burner exit from the side, as illustrated in figure 4.3.
Images are taken with a Phroton Fastcam SA1.1 camera, that view the light scattered by the seeding particles in a direction perpendicular to the laser sheet, see figure 4.3. The CMOS sensor has 1024 x 1024 pixels each with size of 20×20 μm. We carried out some experiments using the full size of the chip, while for the high frame rate measurements it was necessary to crop its size. In particular, at 4.5 kHz and 7.5 kHz in the double frame mode, only part of the chip was used since the remaining part it is employed to speed up the data transfer process. The selected size of the cropped sensor are 768 x 768 pixels and 640 x 512 pixels, respectively.
A Nikon AF Micro-NIKKOR 200 mm f/4D IF-ED lens is fitted on the camera. Furthermore, a typical field of view size was 40mm × 40mm, resulting in a typical magnification factor of M = ~ 0.25.
A programmable timing unit (PTU) is used to synchronize the laser pulses and the high speed camera. The time interval Δt, separating two consecutive pulses of the laser, is an important parameter and has been selected to obtain an average particle image displacement of around 8-15 pixels (over the image), [50]. The image acquisition frequency is set to 50Hz and 5000 image pairs are taken in all the experiments which required statistical robustness. On the other hand, in the transient phenomenon visualization, the acquisition rate were 4.5 kHz or, 7.5 kHz and only 500 image pairs were taken.
The amount of seeding is also an important parameter. In order to have enough light scattered by the seeding particles, high density is desired, at least 10 particles in an interrogation window. However, seeding affect the flame chemistry. Therefore, a trade off is necessary and the amount of seeding required has to be the minimum that allows to achieve a good signal and consequently good cross-correlation in the post processing while affecting the flame behaviour the least possible.
The commercial software DaVis 8.4 was used for both the acquisition and the data processing. Image processing operations to enhance the raw data quality and the processing steps have been used

and are now listed. (1) Image preprocessing, sliding background subtraction with scale 4 pixels and min-max filter for particle intensity normalization over 3 pixels. (2) Cross-correlation with multi-pass, one pass with an interrogation window of 32 x 32 pixels and four passes with an interrogation window of 16 x 16 pixels both with 50 % overlap. In the flashback visualization measurement one pass with an interrogation window of 48 x 48 pixels and four passes with 16 x 16, both with 50% have been applied. (3) Vector post-processing, median filtering with universal outlier detection [63], is applied to the vector field to remove the spurious vectors. Once this filter is adopted, the missing vectors are linearly interpolated. About 95 % of the vectors are first and second choice. Figure 4.4a shows an instantaneous Mie-scattering image for one of the considered turbulent jet flames with the tube burner outlet just visible at the bottom of the image. Figure 4.4b shows the corresponding instantaneous velocity field obtained after the application of the PIV data processing.

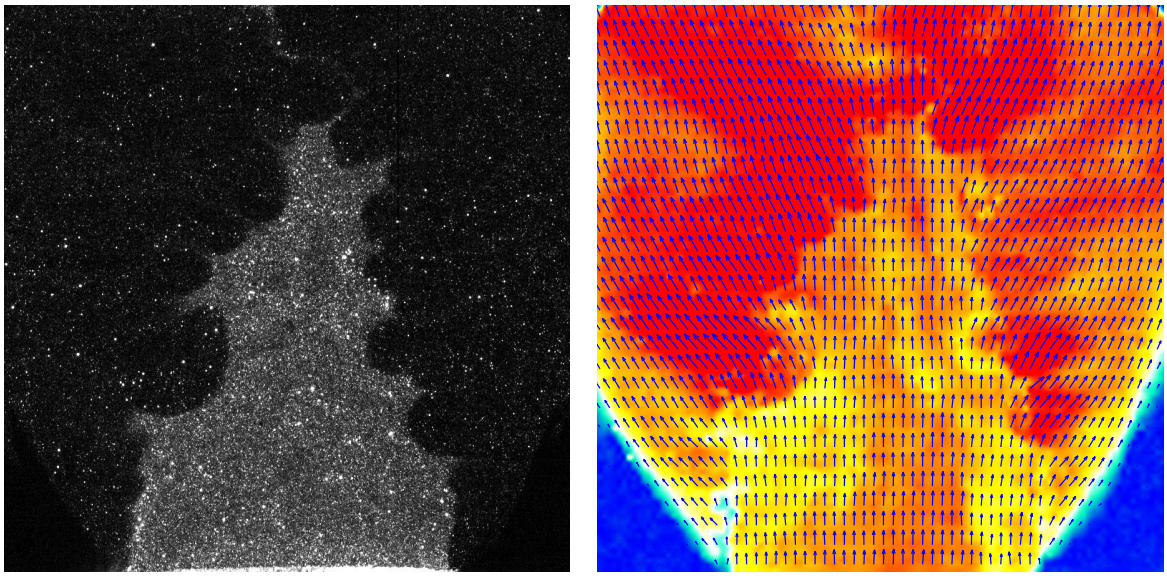

(a) Mie-scattering images of a premixed turbulent jet flame at the tube burner outlet.The laser sheet illuminates the Alumina seeding particles. A pair of these images are then use to apply PIV.

(b) Instantaneous PIV velocity field of a premixed turbulent jet flame.

Figure 4.4: (a) Mie-scattering images of a premixed turbulent jet flame at the tube burner outlet. (b) Instantaneous PIV velocity field of a premixed turbulent jet flame.

4.2.2. Planar Mie-Scattering visualization

Mie-scattering visualization is a technique which uses the particles (seeding) to measure a flow velocity. The signal is produced by elastic scattered light of the particles which need to have a diameter larger or similar to the wavelength of the incident light. In combustion particle Mie-scattering can be use to visualize the shape and position of the flame front. Indeed, the seeded flow experiences a drastic acceleration across the flame front due to heat release induced by combustion. As a consequence of the drastic gas density reduction across the flame front, the seeding particle density (in terms of number of particles per unit volume) also decreases downstream of the flame front. This leads to a reduction of Mie-scattering intensity. Figure 4.4a shows that the seeding density is high in the unburned fuel/air mixture issuing from the pipe exit, while it is low in the post combustion region. The relatively sharp interface between these two regions is defined as the flame front.

4.3. Experimental program and methodology

The experimental program can be divided in four main experiments. The experiments focused on the flashback propensity of flames with different hydrogen/DNG fuel mixtures and different equiv-

alence ratios, the DNG composition considered in the calculation is given in appendix A.
The first experiment investigates different hydrogen/DNG fuel compositions, equivalence ratios and burner conditions, i.e. cooled/uncooled burner tips. The results of the experiments are reported in the form of flame regime maps which show the flashback propensity.
In the second experiment, the unreacting turbulent jet flow that issues from the burner exit (cold flow) has been characterized by means of PIV.
In the third experiment, mean flow fields of flames characterized by different Reynolds number, equivalence ratio and hydrogen concentration in the fuel have been measured and compared to each other.
Finally, in the fourth experiments, the flashback transient phenomenon has been visualized for both a hydrogen and a DNG flame using high speed PIV.
In this section the conditions and methodology, as well as the equipment and sensors used in each of the four experiments are presented.

4.3.1. Experiment 1: producing flame regime maps

The objective of this experiment is to produce flame regime maps in which flashback propensity (indicated by critical velocity gradient and bulk velocity) is shown as function of equivalence ratio for different concentration of hydrogen in the DNG/hydrogen mixtures. Furthermore, the tip temperature at flashback conditions and the effect of cooling on the phenomenon have been measured.
A secondary objective of this experiment is to qualitatively reproduce, literature results on how the flashback propensity is affected by hydrogen addition in DNG/hydrogen mixture and the burner tip temperature.
Table 4.2 shows the experimental conditions and flame cases considered in this experiment. In particular, the fuel composition has been varied to investigate the effect of hydrogen addition. The equivalence ratio ranges from 0.8 to 1.4. In cases 1, 2 and 3 the lower limit of the equivalence ratio is 0.8 since was not possible to obtain a stable jet flame for leaner conditions. The higher hydrogen concentration in cases 4, 5, 6 allows to establish leaner flames. Furthermore, in case 6, the hydrogen mass flow controller capacity limited the equivalence ratio to 1.3. All six cases were investigated with uncooled burners. In order to guarantee that the tube temperature distribution was steady it has been measured at three tube locations, see figure 4.1. The tip temperature was also recorded. Active cooling was applied to cases 4, 5 and 6 only. Under these conditions only one thermocouple was used to check the temperature values at the burner tip, and typical values of TC1 ranged from 35°C - 55 °C. Finally, in each case, the burner tube size was chosen to achieve the highest Reynolds number possible. The flashback conditions are in fact related to the fuel/air mixture composition. In other words, to achieve a high Reynolds number with a mixture characterized by low laminar flame speed, it is necessary to use a burner with a large diameter.
Flashback is an instability phenomenon that can be induced in different ways. In this experiment

	Fuel composition	**Equivalence ratio ϕ (-)**	**Burner tube internal diameter ID (mm)**	**Re**	**Cooled/ uncooled**
Case 1	100 % DNG	0.8 - 1.4	39.20	600 - 5650	Uncooled
Case 2	80% DNG - 20% H2	0.8 - 1.4	39.20	900 - 7230	Uncooled
Case 3	60% DNG - 40% H2	0.8 - 1.4	39.20	2670 - 9404	Uncooled
Case 4	40% DNG - 60% H2	0.7 -1.4	39.20	5690 - 12800	Both
Case 5	20% DNG - 80% H2	0.6 - 1.4	25.67	7980 -12770	Both
Case 6	100% H2	0.6 - 1.3	20.06	10300 - 14440	Both

Table 4.2: Characterization of the premixed flames investigated in experiment 1 to produce the flame regime maps.

it was decided to induce flashback by changing the flow conditions. In particular, air and fuel mass flow rates have been simultaneously lowered in small steps in such a way that the equivalence ra-

tio, and consequently the flame reactivity, was kept constant. In other words through this procedure flashback is approached at a constant adiabatic flame temperature. In practise, the response time of the air, DNG and hydrogen mass flow controllers is slightly different. Therefore, to keep the equivalence ratio as much constant as possible, the steps at which the flow rates were decreased were very small. The equivalence ratio confidence during the experiment was approximately 2.5 % in the most critical cases, that are the ones at lower flow rates where mass flow controller fluctuations affect more the uncertainty. However, these flow rates and linked equivalence ratio variations are always within the uncertainty of the mass flow controller. The procedure to conduct the experiments was as follows: (1) obtain a stable flame,(2) wait long enough to reach a steady temperature value at the three measurement points where the thermocouples were placed,(3) lower the air and fuel mass flow rate,(4) repeat steps (2) and (3) until flashback occurs. Flashback was induced three times for each equivalence ratio. In fact, with the first measurement the approximate bulk velocity at which the flame was unstable was found. In the second and third measurements the burner is ignited close to instability conditions and the procedure is repeated more precisely by taking smaller flow rates reduction steps.

4.3.2. Experiment 2: validation of non-reacting flow field at the pipe exit

In this experiment, the mean flow and turbulence statistics of three non-reacting jets were measured.

The Reynolds number of the non-reacting jets that were considered were close to the Reynolds number of the flames investigated in experiments 3 and 4. The main objective is to characterize the jet flows and to determine weather the flows can be considered as fully developed flows. Table 4.4 lists details of the experimental conditions. The indicated bulk velocities have been computed in two different ways: (1) by considering the total volumetric flow rate Q_{actual}, and the cross sectional area of the tube burners (determined from the diameter measured by Mie-scattering) $U_b = Q_{actual}/A$, and (2) by integrating the mean axial velocity profile $\overline{u}(r)$, obtained from the PIV measurement, according to

$$U_b = \frac{2\pi \int_0^{d_i/2} \overline{u}(r) r dr}{\pi d_i^2/4}. \tag{4.5}$$

Using two methods to compute the bulk velocity enabled a check on the consistency of the experimental data. In the remainder of this thesis the bulk velocity computed with method (1) has been considered. Table 4.4 shows the selected PIV settings.

	Burner internal diameter (mm)	**Bulk velocity (1) (ms^{-1})**	**Bulk velocity (2) (ms^{-1})**	**Deviation % (-)**
Jet 1	20.06	7.52	7.18	4.7
Jet 2	25.67	6.08	5.85	4.0
Jet 3	39.20	4.16	3.98	4.6

Table 4.3: Deviations of the bulk velocities computed with method (1) and (2).

Equation 4.6 can be used to determine the statistical scatter of the mean velocities that have been determined from the PIV data, thus gives an indication about the statistical convergence of the data [22].

$$\sigma_s^2 = \overline{u'^2}\left(\frac{2\tau_0}{T} + \frac{1}{N}\right) \tag{4.6}$$

In equation 4.6, σ_s is the statistical error of the mean velocity, $\overline{u'^2}$ is the variance of turbulence velocity fluctuations, τ_0 is the integral timescale of the velocity, T is the measurement time and N is the number of samples. The terms within brackets in equation 4.6 tells us that in order to minimize the

statistical error in a measurement two requirements have to be met. The duration of the experiment has to be sufficiently large with respect to the integral time scale of the phenomenon, and secondly the number of samples has to be sufficiently large. Both terms within the brackets have to be small. If the ratio of the diameter and the bulk velocity, i.e. d_i/U_b is considered as a rough estimate of the integral time scale, it is found that a typical value of the sum of the two terms in our measurements is $2.36{\cdot}10^{-4}$.
A fully developed flow can be achieved if the ratio between the effective length l and the inner diameter d_i of the tube is sufficiently large, typically l/d_i = 40-50, see [26]. In the current setup the ratios for the three burner tubes are l/d_i = 134.6, 142.6 and 86 for the 20.06 mm, 25.67 mm and 39.20 mm internal diameter tubes respectively. Due to size constraints of the lab it is not possible to install sufficiently long straight pipes. The problem was solved by using a vertical and horizontal tube section and connecting these with a 90 ° bend, as sketched in figure 4.1.

	Burner internal diameter (mm)	**Re** (-)	**Lab T** (°)	**Bulk velocity (ms^{-1})**	**Air flow rate (nl/min)**	**Images #** (-)	**Image rate rate (Hz)**	**Pulses ΔT (μs)**
Jet 1	20.06	9650	21.5	7.39	130	5000	50	40
Jet 2	25.67	9850	21.5	5.90	170	5000	50	45
Jet 3	39.20	10 040	22	3.95	265	5000	50	110

Table 4.4: Characterization of the non reacting flows utilized to validate the velocity field at the pipe outlet in experiment 2.

4.3.3. Experiment 3: measurement of the time-averaged statistics of the reacting flow field

Once the turbulent jet flows has been characterized and validated we can move forward with a more detail study on some turbulent premixed flame cases. In this experiment quantitative and qualitative data are obtained by means of planar PIV.
The objective of this experiment is to assess the effect of different parameters on the flame. Namely, equivalence ratio, hydrogen concentration in the fuel and Reynolds number. Trying to find out which effects can reveal insights about the transition from a stable flame to flashback. Moreover, from the flame statistics, the cone angle will first be defined and then computed for each of the considered flames.
Table 4.5 shows the considered flame cases, experimental conditions, and PIV settings. The Reynolds number is based on the bulk velocity and computed by considering the corrected mass flow rate measurement form the MFCs and the tube diameter measured by Mie-scattering (method (1) 4.3.2). Moreover, for a different mixture the flame speed strongly changes. Therefore to obtain the desired pixels displacement which provides a good correlation the laser pulses Δt are very different. The burner tips were cooled in all the measurements.

4.3.4. Experiment 4: Visualization of the flashback

In the last experiment the flashback was visualized for two selected flames, i.e. a pure DNG flame and a pure hydrogen flame. In these experiments both Mie scattering and PIV measurements were performed at high image acquisition rate.
The objective is to visualize the flashback development in time. Trying to understand how the event occurs, and, in particular, what are the main reasons causing it. A comparison of the results from the two flames may give insight into the physical mechanism inducing this instability.
In this experiment a lean hydrogen flame and an almost stoichiometric DNG flame were selected. In the case of the lean hydrogen flame the 25.67 mm inner diameter tube was used, the equivalence ratio was 0.6 and the flashback instability occurred at a Reynolds number of about 11800,

	Burner internal diameter, d_i **(mm)**	**Re (-)**	**Equivalence ratio,** ϕ **(-)**	**Lab T (°)**	**Bulk velocity** u_b **(ms**$^{-1}$**)**	**Air flow rate,** Q_{air} **(nl/min)**	**Fuel flow rate,** Q_{fuel} **(nl/min)**	**Fuel** H_2 **% (-)**	**Pulses** ΔT **(**μs**)**
Flame 1	20.06	11310	0.8	22	11.24	144.9	48.7	100	27
Flame 2	20.06	13315	0.8	22	13.24	170.5	57.3	100	24
Flame 3	25.67	13310	0.6	21	9.91	217.3	54.7	100	31
Flame 4	25.67	12005	0.6	21.5	8.94	195.9	49.4	100	34
Flame 5	25.67	16139	0.6	22.5	12.02	263.4	66.4	100	26
Flame 6	39.20	10557	0.8	22.5	4.47	258.3	43.1	60	94
Flame 7	39.20	13353	0.8	22	5.65	326.8	54.5	60	74
Flame 8	39.20	11310	0.6	22	4.91	284.1	47.5	80	87
Flame 9	39.20	13805	0.6	22	6.00	346.1	58	80	70

Table 4.5: Characterization of the premixed flames investigated in experiment 3 to study the flame statistics at different conditions.

corresponding to a bulk velocity of 8.8 m/s. In the case of the DNG flame the 39.20 mm inner diameter tube burner was used, ϕ was 0.9 and the Reynolds number was about 5000, corresponding to a bulk velocity of about 2 m/s. The DNG flame was selected close to stoichiometry so that the highest flame speed and, consequently, the highest Reynolds number was obtained. Both burners were cooled during the experiment. The nature of the measurement required very different PIV settings from the ones employed in the previous experiment. In this case the focus is on studying a rapid transient phenomenon and so the image acquisition rate is set to very high values, namely 7.5 kHz for the H_2 flame and 4.5 kHz for the DNG flame, both in double frame mode. To obtain both the Mie-scattering visualization and PIV data, the time between pulses Δt was chosen in such a way that the sequenced frames were equidistant in time. In particular, consider the acquisition rate of 7.5 kHz used for the H_2 flame. It means that each 133.33 μs a pair of images is taken. The Δt between the first and second frame of each pair was selected to be 66.6 μs. This was done so that the phenomenon was effectively visualized at an acquisition rate of 15 kHz. This PIV setting lead to an average pixel displacement of 15 pixels. For the DNG flame the time between the pulses Δt was 111.1 μs leading to a pixel displacement of 8-10 pixel and an effective acquisition frame rate of 9 kHz. For both measurements, the sensor size of the camera was cropped. The lower acquisition rate required for the DNG flame allowed us to use a chip size of 768 × 768 pixels, while for the H_2 flame the chip size was 640 × 512 pixels.

5

Results and discussion

This section presents and discusses the results of four different experiments on flashback that have been explained in detail in the previous chapter.

1. Flames regime maps.
2. Validation of the non-reacting flow fields at pipe exit.
3. Measurement of the time-average statistics of the reacting flow field.
4. Visualization of the flashback.

5.1. Results for experiment 1: Flame regime map

First the flame regime maps will be presented for the uncooled configuration. This is followed by results of the tip temperature and finally a comparison between the cooled and uncooled burners is shown. The results from the present investigation are also compared to some results from literature. Table 4.2, presented in the previous chapter, is here shown to recall the experimental conditions.

	Fuel composition	**Equivalence ratio ϕ (-)**	**Burner tube internal diameter ID (mm)**	**Re**	**Cooled and uncooled**
Case 1	100 % DNG	0.8 - 1.4	39.20	600 - 5650	Uncooled
Case 2	80% DNG - 20% H2	0.8 - 1.4	39.20	900 - 7230	Uncooled
Case 3	60% DNG - 40% H2	0.8 - 1.4	39.20	2670 - 9404	Uncooled
Case 4	40% DNG - 60% H2	0.7 -1.4	39.20	5690 - 12800	Both
Case 5	20% DNG - 80% H2	0.6 - 1.4	25.67	7980 -12770	Both
Case 6	100% H2	0.6 - 1.3	20.06	10300 - 14440	Both

Table 4.2, repeated. Experiment 1, flames investigated

5.1.1. Flashback propensity of uncooled burner tube combustors

Figures 5.1a and 5.1b show how bulk velocity and critical velocity gradient at flashback conditions change as a function of equivalence ratio. The different symbols in the graph refer to different fuel mixture composition. The fuel mixture ranges from 100% DNG, to 100% H_2 with the hydrogen concentration increasing step of 20%. We first consider the effect of increasing hydrogen concentration for a given equivalence ratio. When the hydrogen concentration in the fuel increases the flashback propensity increases. High hydrogen concentration fuels are characterized by high flame speed, small quenching distance and, if sufficiently lean, by less than unity Lewis number which leads to

the thermal diffusive instability described in section 2.3. Therefore when these fuels are employed the flame's ability to travel upstream increases. If we then consider the effect of equivalence ratio on flashback propensity, it can be seen that for H_2 concentration of 0,20,40,60 and 80%, for constant fuel composition, both the critical velocity gradient and bulk velocity have a maximum value at about $\phi \simeq 1$. These peaks in flashback propensity, at $\phi \simeq 1$, qualitatively follow the peak in flame speed, which in turns is related to the adiabatic flame temperature. (The peak in flame speed pretty much coincides with the one in adiabatic flame temperature). The maximum in adiabatic flame temperature is not precisely at stoichiometry because CO_2 dissociates in CO when $\phi \simeq 1.05$ and, as a consequence, the mixture specific heat is lower, leading to higher sensible temperature. This is not

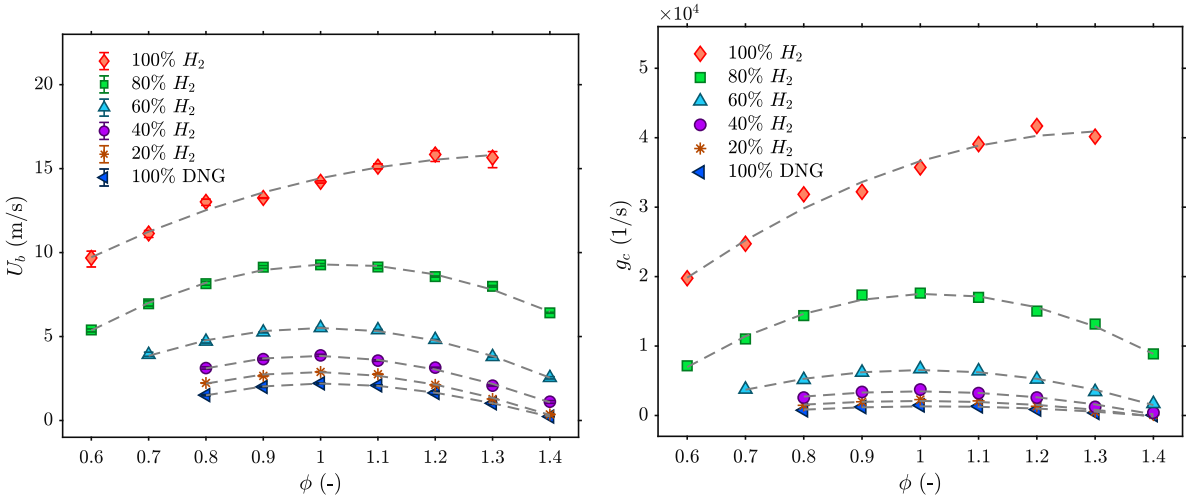

(a) Bulk velocity as function of equivalence ratio at flashback conditions, for different fuel composition mixtures.

(b) Critical velocity gradient as a function of equivalence ratio for different fuel compositions mixtures.

Figure 5.1: Flashback stability maps in terms of (a) the bulk velocity and (b) the critical velocity gradient as a function of equivalence ratio for different H_2/DNG mixtures.

the case when the 100% concentration fuel is considered. In fact, when hydrogen is employed as a fuel, the peak in adiabatic flame temperature is found at $\phi \simeq 1.05$ as for the other mixtures, while the peak in unstretched laminar flame speed shifts towards richer conditions, i.e. $\phi \simeq 1.7$. This shows the connection between the flame speed and flashback propensity. As suggested by Sanchez et al. [52] the peak in hydrogen burning velocity, both for experimental and computational data is at fuel rich conditions because of the high effect of thermal diffusivity and the fuel-rich stoichiometry of the first step of the H_2 reaction mechanism ($3H_2 + O_2 \leftrightarrow 2H_2O + 2H$). Finally, we can observe both in figures 5.1a and 5.1b that an increase in 20% of hydrogen concentration does not cause the same increase in flashback propensity. In fact, the flame speed increase is highly non linear with H_2 addition, Huang et al. [30]. The behaviour for the 20% and 40% hydrogen concentration resemble the behaviour of 100 % DNG. Also, when the fuel is made of 60% H_2 the change in flashback propensity is not very strong. However at 80%, and in particular at 100% hydrogen content in the fuel, the propensity changes drastically.

5.1.2. Burner tip temperature at flashback conditions

Figure 5.2a shows the measured tip temperature at flashback conditions as a function of equivalence ratio for different DNG/H_2 mixture. Consider first the change of the tip temperature with hydrogen concentration in the fuel, for a fixed equivalence ratio. For the fuel air 0,20,40,60% hydrogen concentration, the tip temperature increases with increasing hydrogen content. The reason for this is that, at a given equivalence ratio, the adiabatic flame temperature increases with H_2 concentration. For these mixtures the burner with an inner diameter of 39.2 mm was used. However, for the 80%

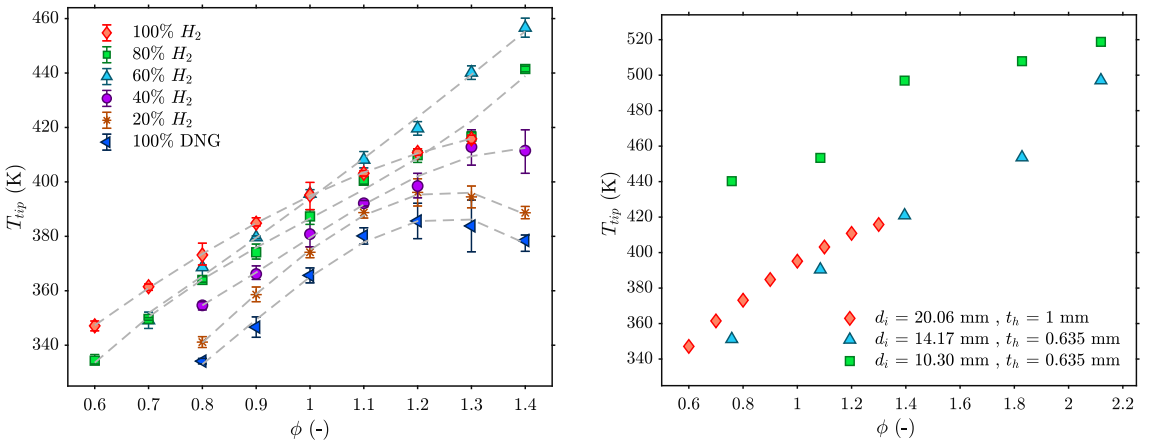

(a) Tube burner tip temperatures as a function of equivalence ratio for different fuel mixture composition.

(b) Tip temperature at flashback conditions for different sizes of tube copper tube burner. The curves relative to d_i = 14.17 and 10.30 are taken from [9], while the curve d_i = 20.06. is form the present work.

Figure 5.2: (a)Tube burner tip temperatures as a function of equivalence ratio for different fuel mixture composition. (b) Tip temperature at flashback conditions for different sizes of tube copper tube combustors.

and 100% H_2, the burners used had a diameter of 25.67 mm and 20.06 mm. The smaller tube diameters imply smaller thermal power, so, even though the adiabatic flame temperature at a given equivalence ratio further rises for these two mixtures, these curves of 80% and 100% are not always above the others curves. The tip temperature for these flames is mainly related to the conductive heat transfer through the burner. Let's now analyse how the tip temperature changes with equivalence ratio ϕ, for a fixed fuel composition. Considering the 60% and 80% H_2 mixtures particularly, but also the 100% H_2, the tip temperature rises with increasing equivalence ratio. This trend is in accordance with literature results, see Bollinger et al. [9]. However this is not the case for the 0,20,40% H_2 concentration mixture. It can be seen that these curves peak at around $\phi \simeq$ 1.2-1.3. This is probably due to the fact that these mixtures have a very small laminar flame speed at high equivalence ratio, consequently the flow rates and thermal power at flashback conditions are small. In other words the reason for the peaks in tip temperature is not related to the fact that the adiabatic flame temperature is decreasing as the mixture gets richer, but to the fact that the burner is able to transfer heat very effectively because of the high conductivity of the copper burner and the thermal power of the flame decreases with decreasing laminar flame speed s_l. Indeed, the adiabatic flame temperature is more than 5 times higher than the combustor tip temperature also in the case of lowest adiabatic flame temperature. Said that, seems reasonable to assume that this drop in temperature is related to the smaller thermal load. Figure 5.2b shows a comparison between data from Bollinger et al. [9], where copper tubes with internal diameters of d_i = 14.17, 10.30 mm were used, with the data obtained in the present work for a copper tube with diameter d_i = 20.06 mm. The differences between these measurements can be associated with the differences in the thickness and diameter of the tubes. Comparing the results for the tube with d_i = 14.17 to those for d_i = 10.30 mm, it is seen that the one with the smaller cross sectional area gets warmer. This is in accordance with what has been observed previously, the tip temperature is strongly influenced by the amount of heat that is transferred by conduction through the cross sectional area of the burner, defined as $\pi d_i t_h$.

5.1.3. Comparison of the flashback propensity of cooled and uncooled tube burners

As shown by Duan et al. [13], the tip temperature strongly affects flashback propensity. This is also confirmed by the results of the present measurements. Figures 5.3a and 5.3b show how flashback propensity, in terms of bulk velocity and critical velocity gradient, is affected by the burner tip tem-

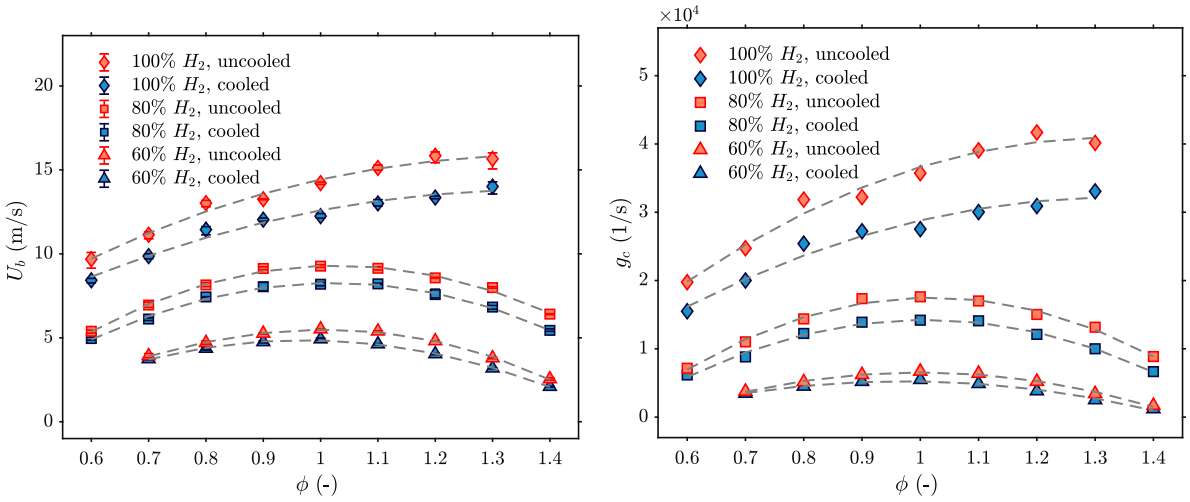

(a) Bulk velocity at flashback conditions for the cooled and uncooled burner configuration, as a function of equivalence ratio for different H_2 content in the fuel.

(b) Critical velocity gradient at flashback conditions for the cooled and uncooled burner configuration, as a function of equivalence ratio for different H_2 content in the fuel. configurations.

Figure 5.3: Bulk velocity at flashback conditions for the cooled and uncooled burner configuration (a). Critical velocity gradient at flashback conditions for the cooled and uncooled burner configuration.

perature. As reported in table 4.2, only the fuels with 60%, 80%, 100% hydrogen concentration have been considered in this comparison. Both figures indicate that the differences in flashback propensity between the cooled burner and the uncooled burner are small at leaner conditions, when tip and adiabatic flame temperature are lower. As the H_2 content in the fuel increases the distance between the curves increases. This indicates that hydrogen rich fuel are strongly affected by the combustor tip temperature. An explanation for this is that the stabilization mechanism of these turbulent jet flames is heat loss. By cooling the tip the heat transfer from the flame to the combustor increases, this causes the flame to be anchored further downstream from the tube burner tip. Similarly, when H_2 concentration in the fuel increases, the adiabatic flame temperature will increase together with the deviation between the cooled and uncooled configuration.

5.1.4. Flashback propensity compared with literature

Figures 5.4a and 5.4b show a comparison of the results obtained in the present investigation with those in the literature. The fuel consists of 100% H_2 and the burners were all cooled. Khitrin et al. [33] have reported on bulk velocities and critical gradients for turbulent jet flames in tube burners with internal diameters of 18, 25.8 and 38 mm, see figure 5.4a, while the critical velocity gradient data in figure 5.4b are taken form Eichler et al. [17], who used a tube burner with an internal diameter of 40 mm. Even though there is some scatter in the data, a clear trend can be observed. In particular the data obtained in the present investigation are the 20.06 mm tube burner ones and these match quite well with the 18 mm tube burner data from Khitrin et al. [33]. These data can be compared even though the diameters of the tubes are different. Indeed it was shown in figure 3.5a section 3.3.2 that the influence of diameter on flashback is weak for turbulent flames. An additional remark can be made regarding to the fully development of the flow. The length of the tube burners employed by Khitrin et al. [33] was 80 cm and there are not information about the 'cold' flow characterization. On the contrary Eichler et al. [17] measured with PIV and compute with models the velocity profile of the non reacting mixture at the tube outlet, showing that the mean velocity profile of the unreacted mixture resemble a fully developed flow. Similarly in the present investigation the mean velocity profile at the tube outlet has been measured by means of PIV and compared to other experimental data in order to show that the flow is fully developed.

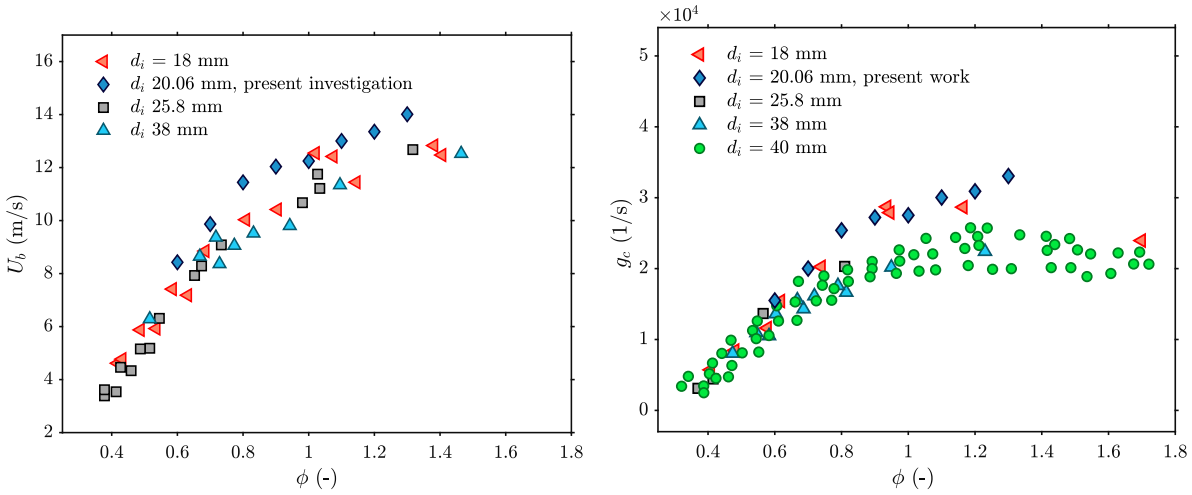

(a) Bulk velocity at flashback conditions of premixed turbulent jet flames for cooled burners. The data relative to the 20.06 mm inner diameter tube burner are form the present work while the 18, 25.8, 38 mm ones are taken from[33]

(b) Critical velocity. A cooled tube has been employed as a burner in all the shown investigation. 40 mm inner diameter tube data are from [17], 18, 25.8,38 mm from [33], 20.06 from the present study.

Figure 5.4: Comparison with literature of (a) bulk velocity and (b) critical velocity gradient at flashback conditions of premixed turbulent jet flames for cooled burners.

5.2. Results for experiment 2: validation of non reacting flow fields at pipe exit

This section is about the validation and characterization of the non-reacting isothermal flow at the pipe exit. Flow field statistics in the form of the mean velocity profile in axial direction $\overline{u}$, Reynolds normal stresses in axial and radial direction $\overline{u'u'}$, $\overline{v'v'}$ and the Reynolds shear stress $\overline{u'v'}$, were determined with PIV for all the three burners. All these quantities are normalized with the flow bulk velocity U_b. For each burner we selected a Reynolds number that is close to the Reynolds number of the jet flames considered in the next section. Table 4.4 provides information on the experimental conditions.

Figure 5.5a compares the axial velocity profiles measured for the three burners to the LDA data of Tummers et al. [60]. These velocity profiles have been taken 0.1 diameter downstream the tube outlets. This was done because the PIV results very close to the pipe exit are inaccurate. Comparison of the Reynolds normal stresses $\overline{u'u'}/U_b^2$ and $\overline{v'v'}/U_b^2$, in figures 5.5b and 5.6b, also show good agreement between the results. In figures 5.6b and 5.5b we can notice that close to the pipe wall r/d = ± 0.5, our results are lower than the values measured by Tummers et al. [60]. This is inherently associated with our measurement technique. In fact, the stagnant surrounding air was not seeded and therefore it could not be measured.

Finally, figure 5.6a shows the Reynolds normal stress for the radial direction $\overline{v'v'}$. From these results two conclusions can be drawn. The first is that the three jet flows considered in this study are very similar and can therefore be compared one another. The second is that these flows are fully developed turbulent pipe flow.

5.3. Flame angle calculation

This section shows how we define the cone angle of the investigated flames. It was shown before in section 2.1.2 that the change in velocity magnitude across the flame front is related to the cone angle and that the gas expansion related to the heat produced by the exothermic reaction affects only the velocity component normal to the flame front. The flame cone angle has been used by Hoferichter et al [29], in the sense that it is one of the main parameters used to predict flashback in

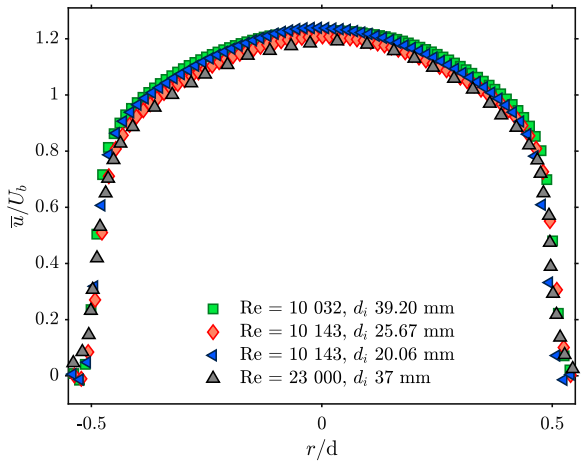

(a) Profile of the mean axial velocity component $\overline{u}$ measured at 0.1 d_i downstream of the tube exit. The data with Re $\simeq 1.0 \times 10^4$ were measured with PIV in the present research while the data for Re $\simeq 2.3 \times 10^4$ were measured with LDA by Tummers et al. [60].

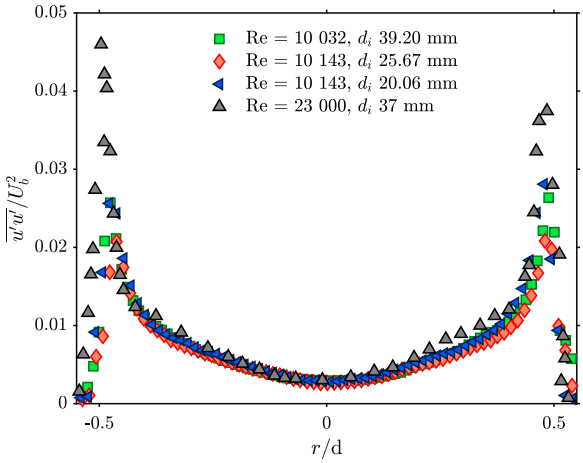

(b) Reynolds normal stress in axial direction $\overline{u'u'}$ measured at 0.1 d_i downstream of the tube exit. The data with Re $\simeq 1.0 \times 10^4$ were measured with PIV in the present research while the data for Re $\simeq 2.3 \times 10^4$ were measured with LDA by Tummers et al. [60].

Figure 5.5: Profile of the mean axial velocity component $\overline{u}$ and Reynolds normal stress in axial direction $\overline{u'u'}$ measured at 0.1 d_i downstream of the tube exit. The data with Re $\simeq 1.0 \times 10^4$ were measured with PIV in the present research while the data for Re $\simeq 2.3 \times 10^4$ were measured with LDA by Tummers et al. [60].

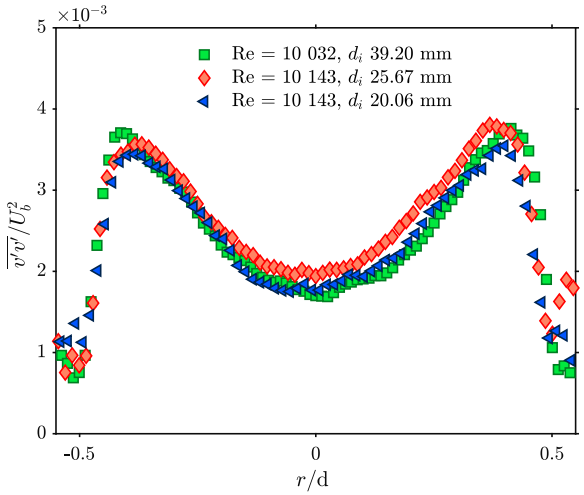

(a) Reynolds normal stress in radial direction $\overline{v'v'}$ measured at 0.1 d_i downstream of the tube exit. The data with Re $\simeq 1.0 \times 10^4$ were measured with PIV in the present research while the data for Re $\simeq 2.3 \times 10^4$ were measured with LDA by Tummers et al. [60].

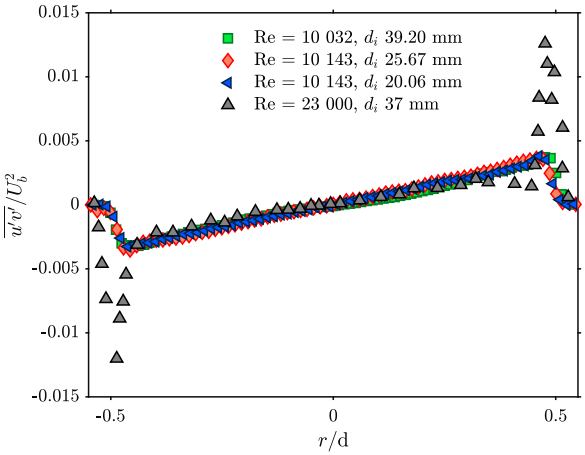

(b) Reynolds shear stress $\overline{u'v'}$ measured at 0.1 d_i downstream of the tube exit. The data with Re $\simeq 1.0 \times 10^4$ were measured with PIV in the present research while the data for Re $\simeq 2.3 \times 10^4$ were measured with LDA by Tummers et al. [60].

Figure 5.6: Reynolds normal stress in radial direction $\overline{v'v'}$ and Reynolds shear stress $\overline{u'v'}$ measured at 0.1 d_i downstream of the tube exit. The data with Re $\simeq 1.0 \times 10^4$ were measured with PIV in the present research while the data for Re $\simeq 2.3 \times 10^4$ were measured with LDA by Tummers et al. [60].

	Burner tube internal diameter ID (mm)	**Re**	**Lab T (°)**	**Bulk velocity (ms^{-1})**	**Air flow rate (nl/min)**	**Images #** (-)	**Image rate (Hz)**	**Pulses ΔT (μs)**
Jet 1	20.06	9650	21.5	7.39	130	5000	50	40
Jet 2	25.67	9850	21.5	5.90	170	5000	50	45
Jet 3	39.20	10 040	22	3.95	265	5000	50	110

Table 4.4:Characterization of the non reacting flows utilized to validate the velocity field at the pipe outlet in experiment 2.

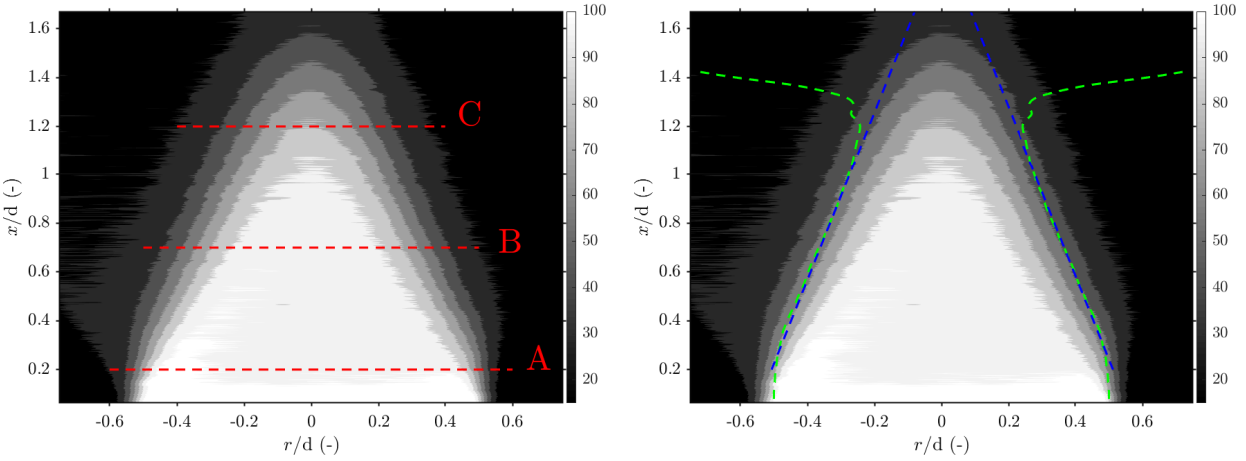

(a) Average flame signal intensity. The signal intensity along lines A, B and C are shown in figure 5.8

(b) (Average flame front surface (green curves) and linearised average flame front (blue lines).

Figure 5.7: (a) Average flame signal intensity, (b) average flame front surface indicated with green curves and linearised average flame front indicated with blue lines.

Bunsen flames and it has been found to be strongly related to the onset of the instability.
By means of the Mie-scattering measurement it is possible to accurately determine the instantaneous flame front location, as was discussed in section 4.2.2 and shown in figure 4.4a. In that figure, 4.4a, the cold core of the flame is characterized by higher seeding density while thermal expansion accelerates the gas just downstream of the flame front causing a sharp drop in seeding density. The average signal intensity is then obtained from 5000 instantaneous images and is shown in figure 5.7. Figure 5.8 shows the average signal along the three lines indicated by A, B and C in figure 5.7a. The

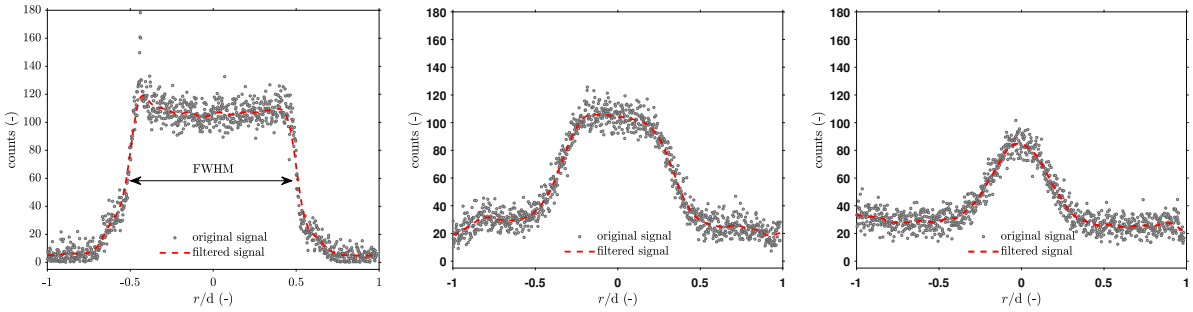

(a) (A) Mean signal strength along a line at 0.2 diameters downstream of the tube outlet. The red dashed line denotes the mean signal strength after filtering.

(b) (B) Mean signal strength along a line at 0.7 diameters downstream of the tube outlet. The red dashed line denotes the mean signal strength after filtering.

(c) (C) Mean signal strength along a line at 1.2 diameters downstream of the tube outlet. The red dashed line denotes the mean signal strength after filtering.

Figure 5.8: Mean signals strength along a line at 0.2, 0.7 and 1.2 diameters downstream of the tube outlet. The red dashed line denotes the mean signals strength after filtering

raw average signals along these lines, have then been filtered with a simple multistep filter in order to reduce the scatter and to produce a smooth curve. The full width half maximum (FWHM) is then used as a measure for the width of the flame cone. By applying this procedure to the data the green curve, which shows the shape of the flame front, in figure 5.7b is obtained. The flame cone angle can then be computed by fitting a straight line to the green curve. The blue curve in figure 5.7b denotes the least squares fitted lines.
Results concerning the compute cone angles are shown in table 5.1.

	Burner tube internal diameter, d_i (mm)	**Re (-)**	**Equivalence ratio, ϕ (-)**	**Bulk velocity u_b (ms^{-1})**	**Fuel composition (-)**	**Flame cone angle α_c (-)**
Flame 1	20.06	11310	0.8	11.24	100 % H_2	41.6°
Flame 2	20.06	13315	0.8	13.24	100 % H_2	39.6°
Flame 3	25.67	13310	0.6	9.91	100 % H_2	38.6°
Flame 4	25.67	12005	0.6	8.94	100 % H_2	34.5°
Flame 5	25.67	16139	0.6	12.02	100 % H_2	31.3°
Flame 6	39.20	10557	0.8	4.47	60 % H_2	40.6°
Flame 7	39.20	13353	0.8	5.65	60 % H_2	39.6°
Flame 8	39.20	11310	0.6	4.91	80 % H_2	38.6°
Flame 9	39.20	13805	0.6	6.00	80 % H_2	31.3°

Table 5.1: Characterization of the premixed flames investigated in experiment 3 to study the flame statistics at different conditions.

5.4. Results of experiment 3: measurement of the reacting flow field

In this section the statistics of some lean premixed turbulent jet flames are analyzed. The aim of this section is to see how Reynolds number (Re), H_2 content in the fuel (H_2%) and equivalence ratio (ϕ) affect the flashback propensity of the flame.
Table 4.5 shows the characteristics of the nine flame that were considered in this study. The results of six of them have been selected and will be presented here, these are: flames 1, 2, 3, 4, 5 and 6. Flames 1, 4 and 6 are very close to flashback conditions. Flame 2 has been compared to flame 3. These flames are characterized by a very similar Reynolds number and both have a fuel composition of 100% H_2, but the equivalence ratios are different. Flame 4 and 5 have the same equivalence ratio and fuel composition, but the Reynolds numbers are different. Finally flame 1 and 6 are also compared. The flames are both close to flashback conditions and have the same equivalence ratio, but the fuel compositions are different. Flame 1 and flame 6 have 100% and 60% H_2 content in the fuel respectively. The selected statistical quantities for the analysis are the mean velocity field, the Reynolds normal stress in radial direction ($\overline{v'v'}$) and in axial direction ($\overline{u'u'}$). These quantities are scaled with U_b, while the radial coordinate is scaled with the tube inner diameter d_i.

Effect of Reynolds number: flame 4 vs flame 5 Flames 4 and 5 both used the 25.67 mm inner diameter burner, the equivalence ratio is ϕ = 0.6 and the fuel composition is 100% H_2. The difference between the two flames is the bulk velocity U_b which leads to different Reynolds numbers, i.e. 12 005 for flame 4 and Re 16139 for flame 5. Moreover flame 4 is very close to flashback, its bulk velocity is 2% higher than the bulk velocity at which flashback occurs, while U_b of flame 5 is 35 % above the flashback limit.
When comparing figures 5.9a, 5.9c, 5.9e with 5.9b, 5.9d and 5.9f, respectively, it can be seen that flame 4, which is close to flashback, is shorter, meaning that the cone angle is bigger than that in flame 5. This difference in cone angle leads on average to a higher acceleration of the flow across the flame front, as can be seen in figures 5.9a and 5.9b by considering the colormap in the region just above the flame front. Flame 4 has a bigger region where the velocity magnitude increase (ratio of local velocity and bulk velocity) is 1.4, while flame 5 has a smaller ratio, around 1.3 in a much smaller region. Figures 5.9e and 5.9f, compare the intensity of the Reynolds normal stress in axial direction $\overline{u'u'}$ for flame 4 and 5 respectively. It can be clearly seen that the intensity of $\overline{u'u'}$ in the region above the flame front is relatively high in flame 4. Furthermore in flame 4 the intensity of $\overline{u'u'}$, starts to increase considerably at around a distance of 1.2 d_i from the outlet, while its increase for flame 5 is at around 1.6 d_i. These effects, caused by the different bulk velocities, can probably be related to the difference in cone angles. Consider the kinematic of a Bunsen flame, see section 2.1.2, at the tube outlet the unreacted gas mean velocity component is axially directed. Once the

mixture reaches the flame front, the reaction occurs and the exothermic process expand the gas. This expansion results in an increase of the velocity component normal to the flame front. It follows from a simple one-dimensional balance equation that the increase in velocity has to be equal to the density ratio, or temperature ratio, between the burned and unburned mixture. Now, this analysis is very simplified and holds for one dimensional cases, so considering a flat flame front. Nevertheless, the results of the analysis are qualitatively correct for our case, in the sense that a larger angle (or shorter cone) results in a larger increase in velocity magnitude across the flame front.
The high values of the turbulence fluctuations in correspondence to the flame front can be explained by considering that the instantaneous flame front is sometimes located above and sometimes below the average location of the flame front. In other words, when for instance the instantaneous flame front is located below the average location, there will be burned gases with a relatively high velocity at the average flame front location. With the same reasoning, the opposite situation occurs when the instantaneous flame front is located above the average location. In other words the intermittency between reacted/unreacted gases causes high values of the Reynolds normal stress $\overline{u'u'}$. A higher velocity increase also leads to higher flame front fluctuations due to the stronger flame flow interaction associated with hydrodynamic instability, see section 2.4. Consequently, flame 4 is characterized by higher values of the Reynolds normal stress, both for the axial and normal direction, 5.9c, 5.9d and 5.9e, 5.9f. Finally, another aspect that might cause stronger interaction could be the location at which the flames are anchored. Indeed Flame 4 is anchored closer to the tube outlet, this might causes a stronger interaction between the flame and the flow, since the flow approaching the flame has less space to adapt to change in pressure imposed by the flame front.

Effect of equivalence ratio: flame 2 vs flame 3 Flames 2 and 3 both have the same fuel (100 % H_2) and very similar Reynolds number, i.e. Re = 13316 for flame 2 and Re = 13308 for flame 3. The main difference between the two flames is the different equivalence ratio, i.e. ϕ = 0.6 for flame 2 and ϕ = 0.8 for flame 3. In order to obtain a very similar Reynolds number, flame 2 uses a burner with an inner diameter of 20.06 mm, while the inner diameter for flame 3 is 25.67 mm.
When comparing figures 5.10a, 5.10c, 5.10e with 5.10b, 5.10d, 5.10f it can be seen that the average cone angles of the two flames are very similar, i.e. 39.6° for flame 2 and 38.6°, for flame 3. Both flames are at conditions slightly above the stability limit. More precisely, flame 2 has a bulk velocity that is 17 % higher than the bulk velocity at which flashback occurs, while flame 3 has a bulk velocity that is 10 % above the flashback limit.
In the effort of explaining the differences between these two flame we have again to consider the hydrodynamic instability. The hydrodynamic instability depends on the velocity magnitude increase across the flame front. In turn, this increase is a function of burned to unburned gas density ratio and cone angle. Burned to unburned gas density ratio depends on fuel composition and equivalence ratio, while the cone angle depends on the flow field flame speed balance (for a given mixture composition and equivalence ratio, cone angle could be write as function of U_b). The fuel composition for these two flames is the same, cone angles are also very similar while ϕ is different. Given these considerations we would expect flame 2 (which has an higher equivalence ratio) to exhibit a larger velocity increase across the flame front. However, the comparison between figure 5.10a and 5.9f does not show that (ratio between flame temperature and ambient temperature is 7.4 and 6.3 for flame 2 and 3 respectively). A possible explanation for this could be that the leaner flame shows some effect of the thermal diffusive instability, see section 2.3. Indeed, flame 3 has a smaller Lewis number and it is characterized by negative a Markstein length. Effectively flame 3 burning velocity is enhanced by the instability that manifest itself when the flame is stretched [30]. Furthermore, considering flame 3, some differential diffusion effects might also lead to differences between the local equivalence ratio and the average equivalence ratio. However, comparing figures 5.10c with

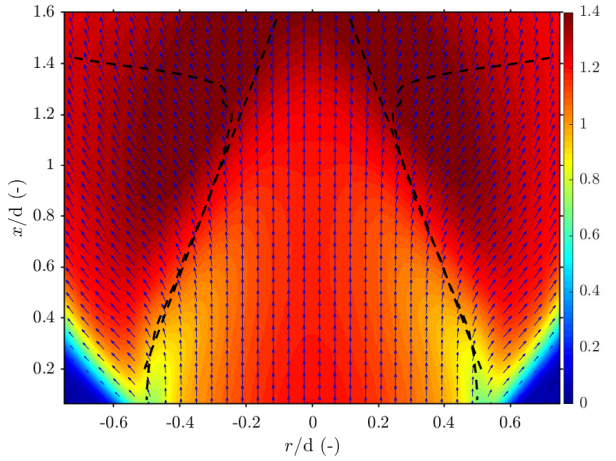

(a) Flame 4. Mean Velocity field $\overline{u}(r,x)/U_b$ for Re 12005

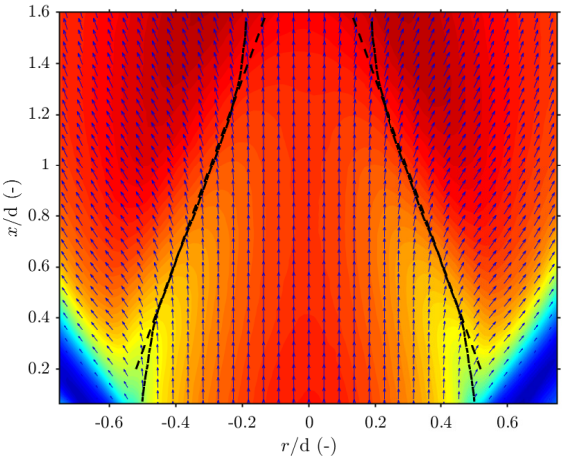

(b) Flame 5. Mean Velocity field $\overline{u}(r,x)/U_b$ for Re 16139

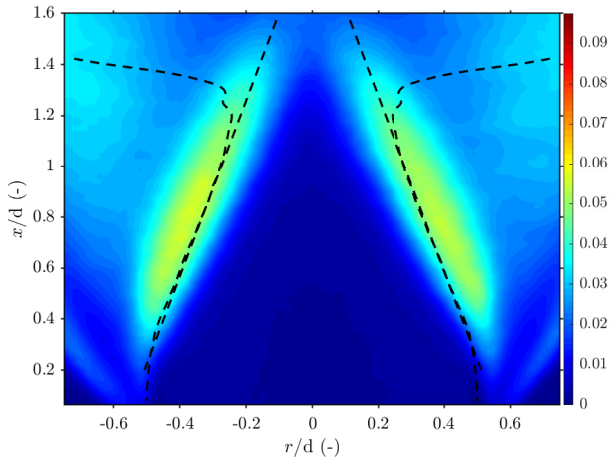

(c) Flame 4, Reynolds normal stress for the radial direction $\overline{v'v'}/U_b^2$ for Re 12005

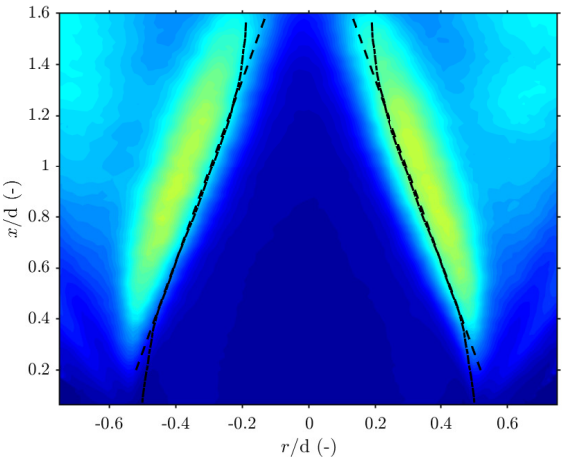

(d) Flame 5, Reynolds normal stress for the radial direction $\overline{v'v'}/U_b^2$ for Re 16139

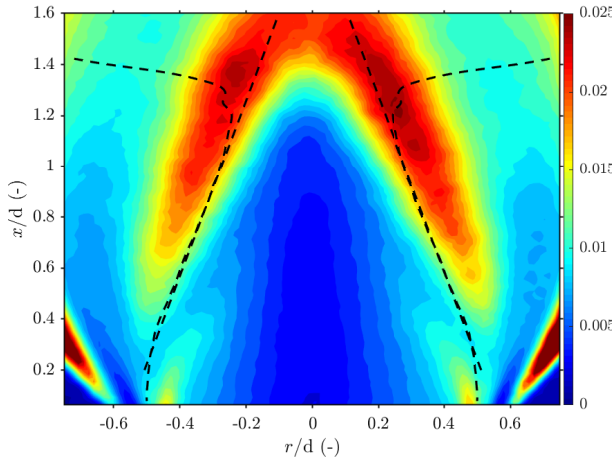

(e) Flame 4, Reynolds normal stress for the axial direction $\overline{u'u'}/U_b^2$ for Re 12005

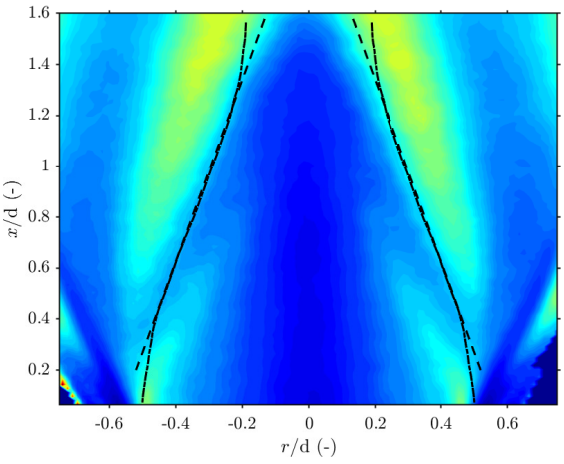

(f) Flame 5, Reynolds normal stress for the axial direction $\overline{u'u'}/U_b^2$ for Re 16139

Figure 5.9: Comparison of mean Velocity field $\overline{u}(r,x)/U_b$, Reynolds normal stress in the radial direction $\overline{v'v'}/U_b^2$ and Reynolds normal stress in the axial direction $\overline{u'u'}/U_b^2$ of flame 4 and flame 5, which are characterized be same composition and equivalence ratio, but different Reynolds number.

5.10d and 5.10e with 5.10f emerges that the richer flame shows higher turbulence Reynolds stress both in the axial and radial direction. This is in agreement with the fact that flame 2 is characterized by a bigger density ratio across the flame front, consequently bigger velocity magnitude increase and stronger effect of the hydrodynamic instability, which causes a strong flame-flow interaction that leads to a bigger oscillation of the flame front around its average location.
Another interesting fact that emerges from the comparison, flame 3, the leaner one characterized by smaller Markstein length, has higher $\overline{v'v'}$ and $\overline{u'u'}$ in the neighbourhood of the rim at the burner outlet. This might be related to the fact that, in accordance with equation 2.9, flame 3 is more sensitive to stretch effects which cause the increase in burning velocity.

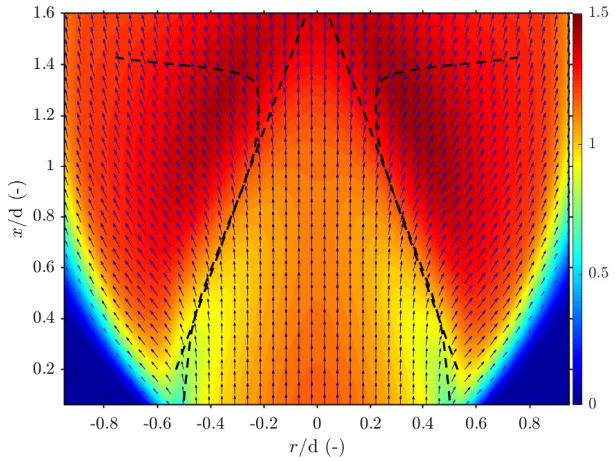

(a) Flame 2. Mean Velocity field $\overline{u}(r,x)/U_b$ for $\phi = 0.8$

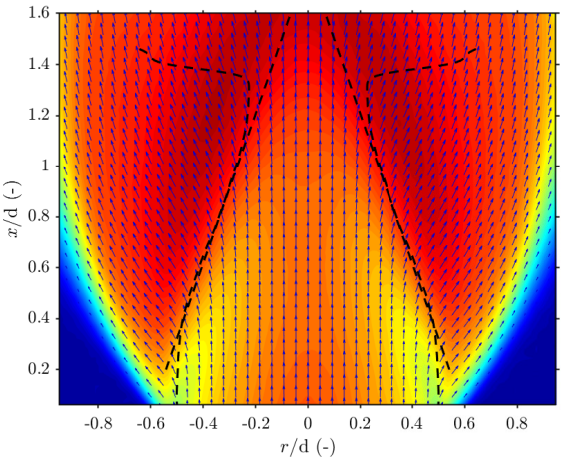

(b) Flame 3. Mean Velocity field $\overline{u}(r,x)/U_b$ for $\phi = 0.6$

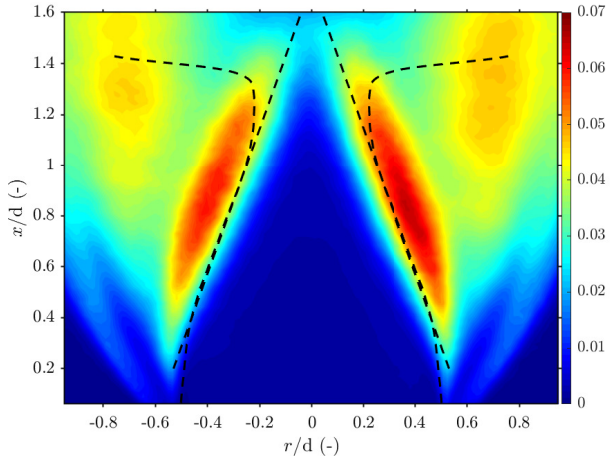

(c) Flame 2. Reynolds normal stress for the radial direction $\overline{v'v'}/U_b^2$ for ϕ =0.8

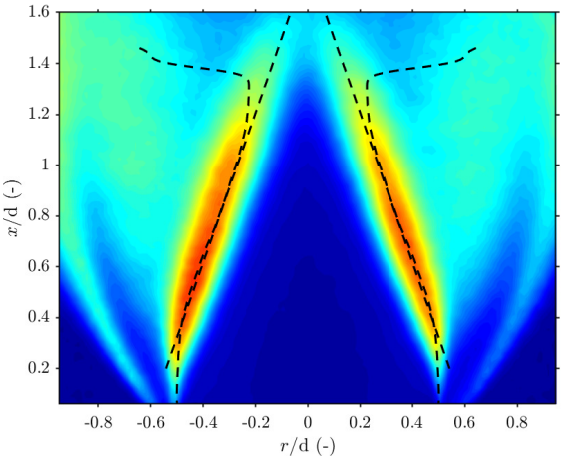

(d) Flame 3. Reynolds normal stress for the radial direction $\overline{v'v'}/U_b^2$ for $\phi = 0.6$

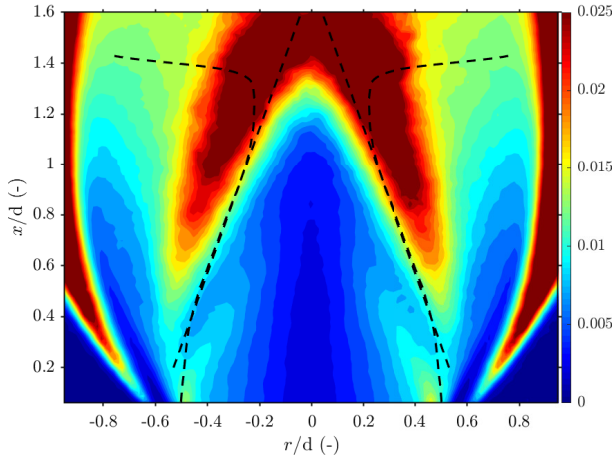

(e) Flame 2. Reynolds normal stress for the axial direction $\overline{u'u'}/U_b^2$ for $\phi = 0.8$

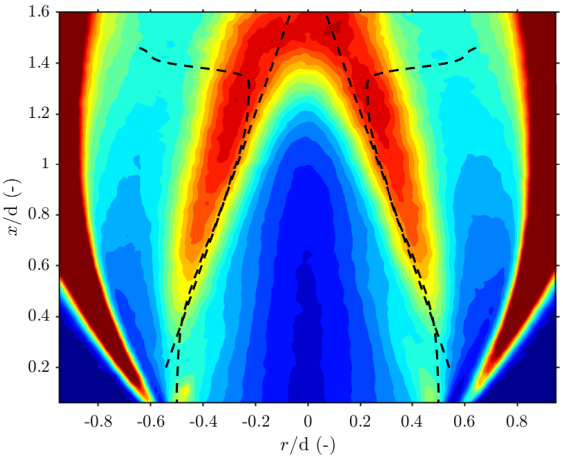

(f) Flame 3. Reynolds normal stress for the axial direction $\overline{u'u'}/U_b^2$ for $\phi = 0.6$

Figure 5.10: Comparison of mean Velocity field $\overline{u}(r,x)/U_b$, Reynolds normal stress in the radial direction $\overline{v'v'}/U_b^2$ and Reynolds normal stress in the axial direction $\overline{u'u'}/U_b^2$ of flame 2 and flame 3, which are characterized be same composition and Reynolds number, but different equivalence ratio.

Effect of hydrogen concentration: flame 1 versus flame 6 Flames 1 and 6 have the same equivalence ratio, flame 1 Reynolds number is Re = 11 310 and flame 6 Reynolds number is 10 557. Furthermore both flames are very close to flashback conditions. More precisely bulk velocity of flame 1 is 2 % above flashback U_b and the bulk velocity of flame 6 is 3 % above flashback limit. Flame 1 has a fuel concentration of 100% H_2, while flame 6 has a fuel concentration of 60% H_2 and 40% DNG. Furthermore flame 1 is characterized by a cone angle of 41.6° and a temperature ratio across the flame front of 7.4, while flame 6 has a cone angle of 40.6 ° and a temperature ratio of 6.9.
Comparing figures 5.11a and 5.11b the velocity magnitude increase is very similar for the two flames. Furthermore, it can be seen that, in the neighbourhood of the burner rim, flame 1 has more pronounced low velocity pockets than flame 6. This suggests that, when using pure H_2 as a fuel, the flame experiences a different flame flow interaction. The values of the Reynolds normal stress in radial direction $\overline{v'v'}$ are slightly higher for flame 1 than for flame 6, see figures 5.11c and 5.11d. Figures 5.11e and 5.11f compare the Reynolds normal stress in axial direction $\overline{u'u'}$. Flame 6 shows much higher values of this quantity and in general higher than all the other H_2 flame considered. We can try to explain this fact as a consequence of the thermal diffusive instability, that was described in section 2.3. In general, Bunsen flames that are characterized by a non unity Lewis number can show a behaviour called tip-opening effect [42]. In particular, consider a lean laminar H_2 premixed flame and consider the flame front to be negatively curved, as it is at the tip of a Bunsen flame. There is heat diffusing from the reaction zone to the preheat zone, while the incoming unburned mixture diffuses towards the reaction zone. Less than unity Lewis number means that mass diffusion is predominant over thermal diffusion, when the flame curvature is negative, it causes to have locally a leaner mixture and some enthalpy of reaction is lost. The tip of a Bunsen lean H_2 flame is then characterized by a weaker burning rate. When the radius of curvature is sufficiently small the reaction does not occur any more and is possible to see this tip-opening effect. Our flames are turbulent, nevertheless this phenomenon that is clearly observed in H_2 premixed laminar flames could be the reason why flame 1 has a weaker normal Reynolds stress in axial direction.

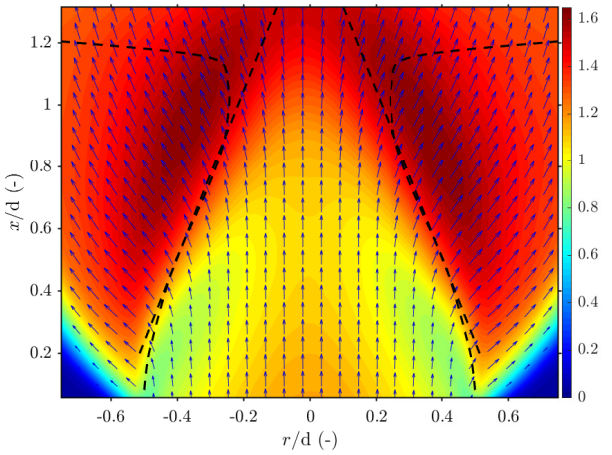

(a) Flame 1. Mean Velocity field $\overline{u}(r,x)/U_b$ for 100% H_2 concentration.

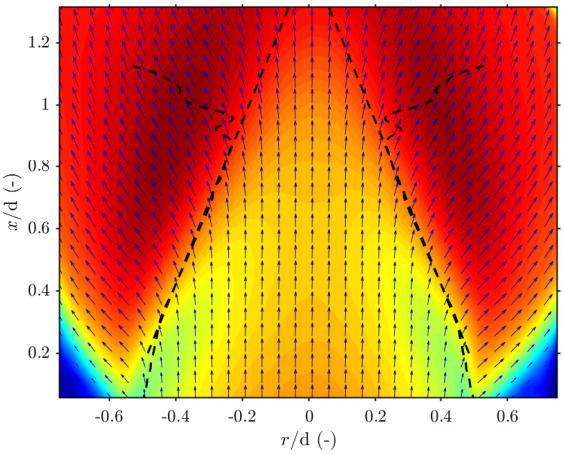

(b) Flame 6. Mean Velocity field $\overline{u}(r,x)/U_b$ for 60% H_2, 40% DNG concentration.

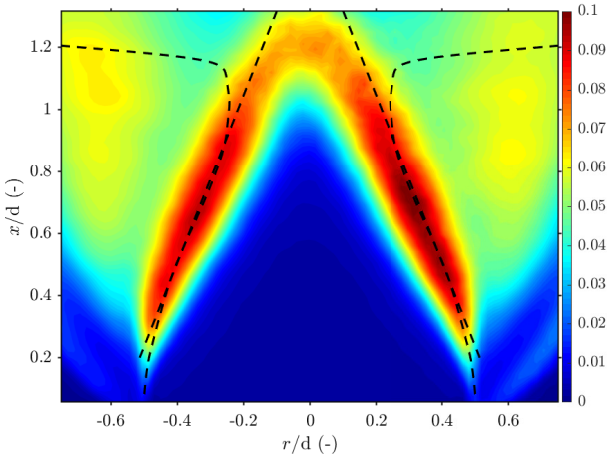

(c) Flame 1. Reynolds normal stress for the radial direction $\overline{v'v'}/U_b^2$ for 100% H_2 concentration.

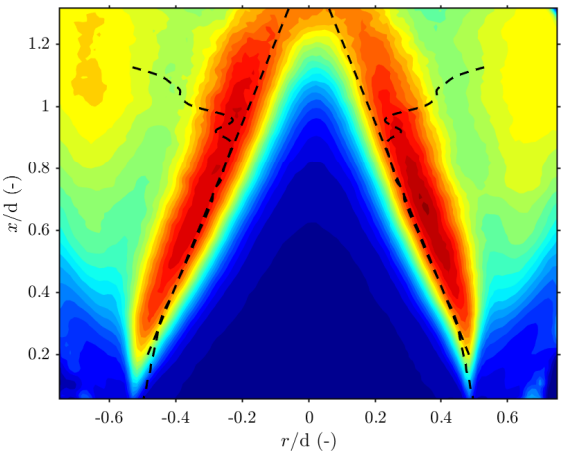

(d) Flame 6. Reynolds normal stress for the radial direction $\overline{v'v'}/U_b^2$ for 60% H_2, 40% DNG concentration.

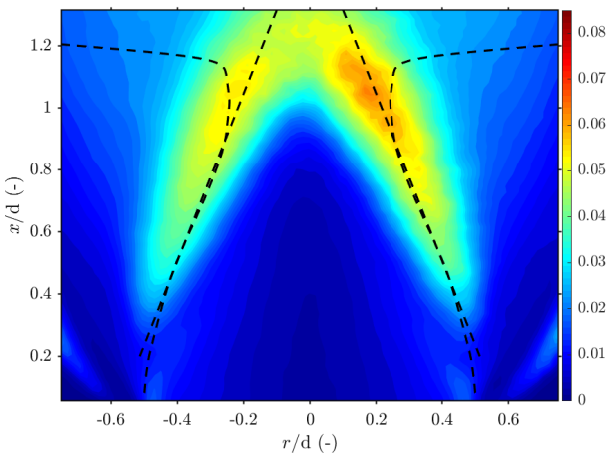

(e) Flame 1. Reynolds normal stress for the axial direction $\overline{u'u'}/U_b^2$ for 100% H_2 concentration.

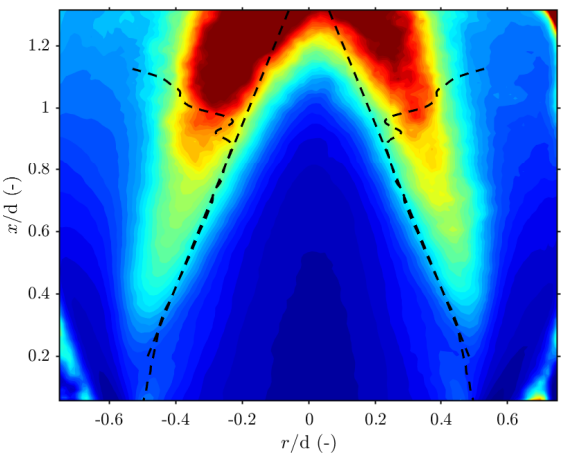

(f) Flame 6. Reynolds normal stress for the axial direction $\overline{u'u'}/U_b^2$ for 60% H_2, 40% DNG concentration.

Figure 5.11: Comparison of mean Velocity field $\overline{u}(r,x)/U_b$, Reynolds normal stress in the radial direction $\overline{v'v'}/U_b^2$ and Reynolds normal stress in the axial direction $\overline{u'u'}/U_b^2$ of flame 1 and flame 6, which are characterized be same equivalence ratio and Reynolds number, but different fuel composition.

5.5. Experiment 4: Visualization of the flashback

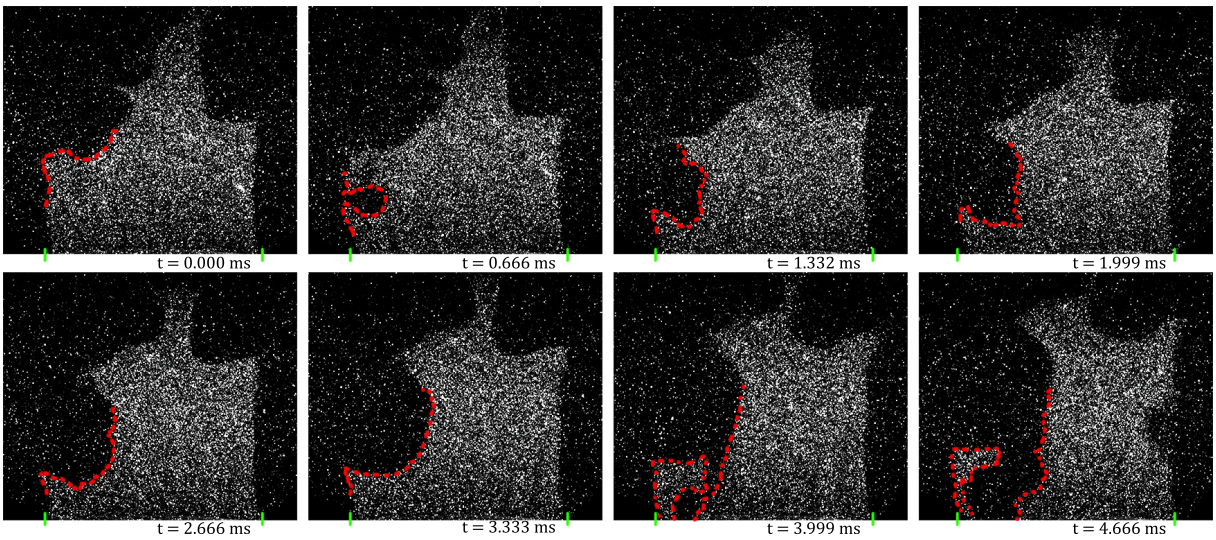

Figure 5.12: Time evolution of DNG premixed jet flame flashback, visualized by means of Mie-scattering. The Δt between each flame is 0.666 ms. The flame has a Re number of about 5000, and an equivalence ratio of $\phi = 0.9$. In the figure the inner wall of the tube burner outlet are indicated with two green marks on the bottom edge of each frame. Furthermore the flame front in locations of interest is also marked with a red dashed line.

This section presents the results of the visualization of the flashback event for two different flames, i.e. (1) a 100% H_2 lean flame ($\phi = 0.6$) at a Reynolds number of Re $\simeq$ 11 800 and (2) an almost stoichiometric 100% DNG flame ($\phi = 0.9$) at a Reynolds number of Re $\simeq$ 5000. The visualization is done using the Mie-scattering technique described in section 4.2.2, which allows to identify the instantaneous flame front location. Instantaneous velocity fields obtained by means of PIV will also be shown. The aim of this experiment is to identify the mostly relevant physical mechanisms for the instability occurrence and to determine if there are substantial differences between the flashback phenomenon for the two different flames.
The techniques used in this experiment (Mie-scattering and PIV) have certain limitations, because flashback has a stochastic nature and it is strongly three-dimensional. Mie-scattering and PIV are planar and for this reason it is not possible to assure with 100% confidence where the phenomenon started. However the experiments have been repeated multiple times, with around 25 realizations for each flame. Thanks to this, some experience and understanding were developed, which allowed to understand when the instability onset was sufficiently close to the measurement plane. Boundary layer flashback visualization has already been carried out by Baumgartner et al. [6]. However, they considered a different geometry, i.e. a channel combustor, purposely designed with an asymmetric wall aiming to induce flashback on that side of the channel.
The results of the visualization will be presented in the form of two graphs, each showing eight sequential snapshots of the Mie-scattering intensity and the corresponding velocity field obtained from PIV. The snapshots have been selected such that the first frame represents the beginning of the flashback phenomenon and the last frame shows the flame inside the tube burner. For clarity, in each frame the inner diameter has been indicated with two vertical marks at the base of the figure. Furthermore, the position of the flame front has been highlighted in the locations of interest.

5.5.1. Flashback dynamics

Figure 5.12 shows the DNG flashback as visualized by the Mie-scattering experiment. The time interval between each frame is 0.666 ms. The sequence shows the development of the flame front location in time. It can be seen that a flame bulge that first happens in the second frame moves to-

wards the axis while consuming the incoming unreacted mixture. While the flame front propagates through the mixture, it is also advected downstream by the flow. The size of the bulge drastically grows in time. It also flattens out in time. This might be related to the combined effect of thermal-diffusive and hydrodynamic instabilities, as discussed in section 2.4, where it can be seen from the solution of equation 2.13, shown in figure 2.6, that mixtures characterized by positive Markstein length (DNG and most hydrocarbons) are able to dump out big wave number disturbances. Indeed when the fuel is characterized by a positive Markstein length the thermal-diffusive instability has a stabilizing effect. In the second last frame of figure 5.12, it can already be seen that the flame succeeds in travelling upstream and it is able to enter the burner. In the last frame this is even more clear since a wide low particle density area emerges from the tube outlet. Figure 5.13 shows the ve-

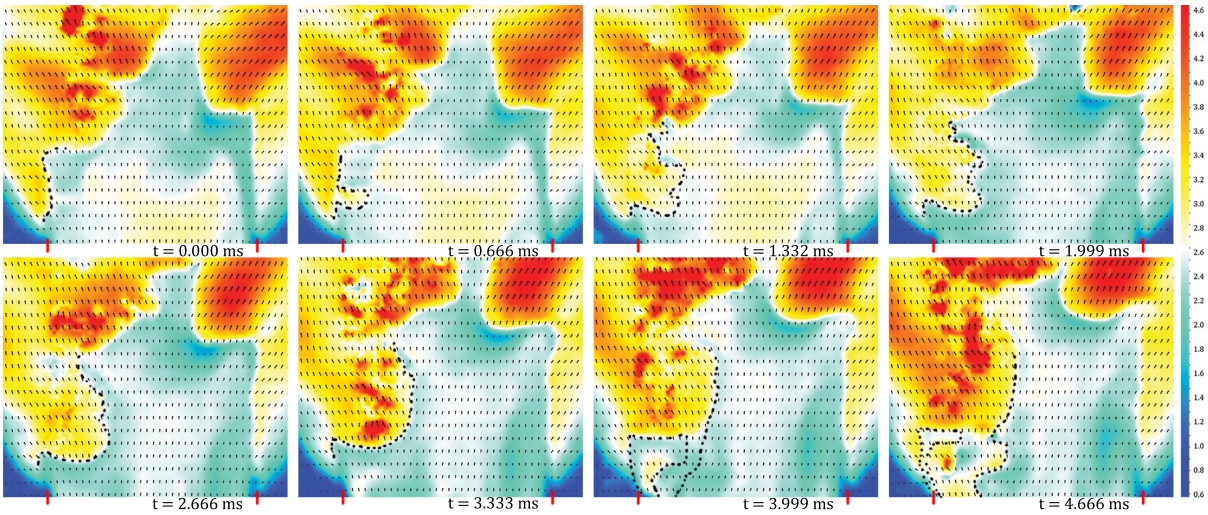

Figure 5.13: Time evolution of velocity fields of the DNG premixed jet flame during flashback, as determined by of PIV. The time difference Δt between each frame is 0.666 ms. In each subfigure the inner wall of the tube burner is marked with two red lines at the bottom edge of each frame. The flame front in locations of interest is marked with a black dashed line.

locity fields related to the raw Mie-scattering images of figures 5.12. It is interesting that regions of high velocity are located just above the burner outlet in the last two frames. This confirms the occurrence of thermal expansion due to the flame which is located just below the high velocity pockets. Figures 5.14 and 5.15 illustrate the flashback for the 100% H_2 flame. The flashback phenomenon develops qualitatively in the same way as in the DNG flame. However, the flame bulge growth is different. In this case the flame front at flashback location is characterized by more irregularities; it is not as smooth and flat as in the case of the DNG flame. Indeed, the Markstein length of the lean hydrogen flame is negative, which causes the small wavelength disturbances to have a positive growth rate, see figure 2.6 in section 2.4. For these flames all disturbances are unconditionally unstable up to very large wavelengths [39]. Another substantial difference is that in the H_2 flame, flashback event takes place in about 1 millisecond which is almost 5 times less than the time required for the flashback of the DNG flame. Hydrogen flame speed grows drastically with flame stretch. This is related to the mixture Markstein length and Lewis number. As shown in equation 2.11 in section 2.3, the lean hydrogen mixture burning velocity can drastically increase with stretch. In the last three frames of figure 5.15, in particular in the third last, a low velocity pocket is clearly visible just upstream of the flame front. We will develop the observation more in depth, but before doing so we note that flashback is not really occurring inside the thin boundary layer on the tube wall. This can be seen from the last two frames of figures 5.12 and 5.14, in which patches of high density seeding are located just above the burner rim, and is in accordance with what has been observed by Baumgartner et al. [5]. This indicates that the flame has not reached the tube inner wall, but has travelled inside the burner at some distance from the inner wall. To explain this observation, attention will now be focused on

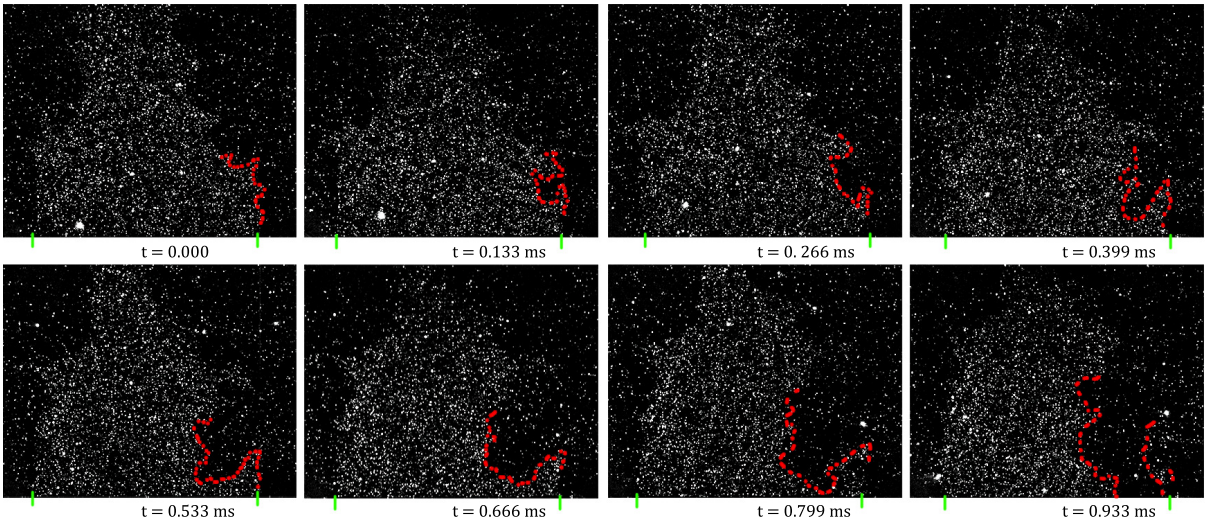

Figure 5.14: Time evolution of the flashback of the H_2 premixed jet flame, visualized by means of Mie-scattering. The time difference between each frame is 0.133 ms. In each subfigure the inner wall of the burner is marked with two green marks at the bottom edge. The flame front, in locations of interest, is marked with a red dashed line.

the effect of the adverse pressure gradient due to the flame presence.

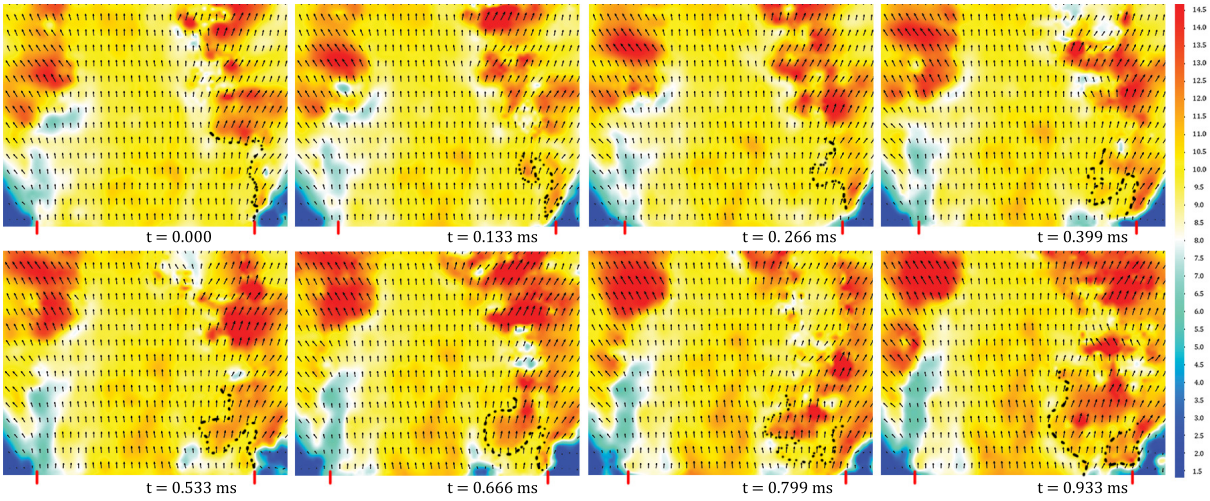

Figure 5.15: Time evolution of velocity fields during flashback of the H_2 flame as determined from PIV. The time difference between each frame is 0.133 ms. In each subfigure the inner wall of the burner is marked with two red lines at the bottom edge of each frame. The flame front in locations of interest is marked with a black dashed line.

5.5.2. Flame induced adverse pressure gradient

Figure 5.16 (right side) show a low velocity pocket just upstream the flame front location which is easily identified by looking at the velocity gradient or from the corresponding Mie-scattering image located in the left part of the figure. Focusing on the low velocity region it can clearly be seen that the velocity vectors diverge and decrease in magnitude just upstream of the flame front. The deflection of the velocity vector is then related to the presence of the flame front. This kind of flame flow interaction can be observed frequently in the PIV data for both the Hydrogen and DNG flames.
The pressure rise just upstream the flame front has been computed in a DNS investigation by Gruber et al. [24], and it depends on the velocity magnitude increase across the flame front and on its curvature and orientation. In their study, Gruber et al. [24] investigates a flame anchored in

a boundary layer, while in the present work the flame flow interaction occurs relatively far from a wall, approximately 1.5 diameters downstream the burner outlet.

To support the previously done observations an effort in computing the adverse pressure gradi-

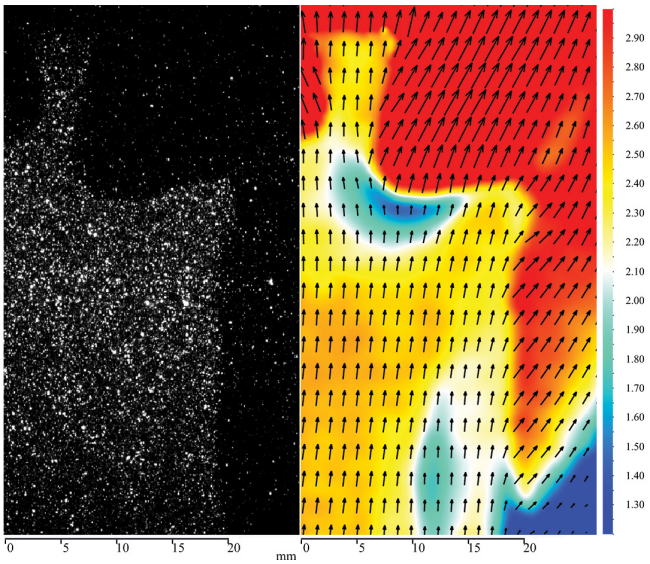

Figure 5.16: In this picture we can see raw data relative to half DNG jet flame on the left side and the respective PIV computed vector field on the right side. The picture shows a flame bulge in the top part, just below the flame front. From the colormap representation and the vector field is possible to see the effect of the adverse pressure gradient on the incoming flow, caused by the D-L instability. Just ahead of this low velocity pocket the vectors diverge and the velocity decreases.

ent has been done. To do so the Navier-Stokes equations in cylindrical coordinates has been considered. In particular the flow was assumed to be incompressible and isothermal and the viscous terms were neglected since our investigation is limited to regions sufficiently far from the wall. The equation of motions have already been presented in section 2.5.2 as equations 2.22, 2.23 and 2.24. The momentum equation in axial direction, equation 2.23, is now made dimensionless by introducing dimensionless coordinates x^* and r^*, dimensionless velocity component u^* and v^* and dimensionless pressure p^*.

$$x^* = \frac{x}{D}; \quad r^* = \frac{r}{D}; \quad u^* = \frac{u}{u_b}; \quad v^* = \frac{v}{u_b}; \quad p^* = \frac{p}{\rho u_b^2}. \tag{5.1}$$

After neglecting the viscous terms, the simplified dimensionless form of the continuity equation and the momentum balance in axial direction read,

$$\frac{\partial \overline{u^*}}{\partial x^*} + \frac{1}{r^*}\frac{\left(\partial r^* \overline{v^*}\right)}{\partial r^*} = 0 \tag{5.2}$$

$$\underbrace{\overline{u^*}\frac{\partial \overline{u^*}}{\partial x^*}}_{\substack{\text{Advection}\\ \text{axial}\\ \text{direction}}} + \underbrace{\overline{v^*}\frac{\partial \overline{u^*}}{\partial r^*}}_{\substack{\text{Advection}\\ \text{radial}\\ \text{direction}}} = - \underbrace{\frac{\partial \overline{p^*}}{\partial x^*}}_{\substack{\text{Pressure}\\ \text{gradient}\\ \text{axial}\\ \text{directon}}} - \underbrace{\frac{\partial \overline{u'^* u'^*}}{\partial x^*}}_{\substack{\text{Reynolds}\\ \text{stress}\\ \text{gradient}\\ \text{axial}\\ \text{direction}}} - \underbrace{\frac{1}{r^*}\frac{\partial\left(r^* \overline{u'^* v'^*}\right)}{\partial x^*}}_{\substack{\text{Reynolds}\\ \text{shear stress}\\ \text{gradient}\\ \text{radial}\\ \text{direction}}}. \tag{5.3}$$

Equation 5.3 further simplifies when we consider the terms along the centerline of the burner. The velocity component in radial direction is zero, $v = 0$. The Reynolds shear stress gradient in radial

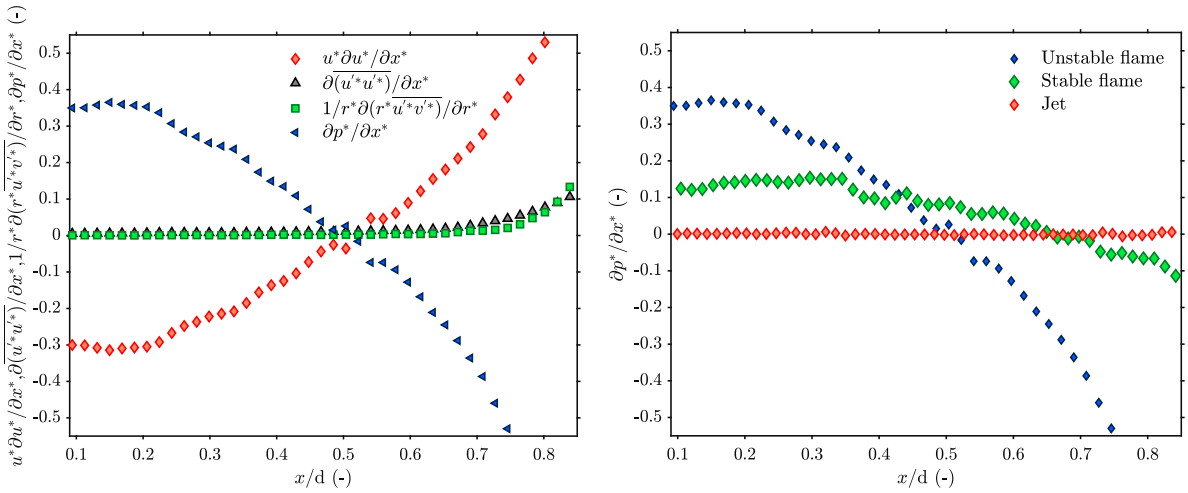

(a) Terms of the simplified momentum balance equation in axial direction. Namely, the advection term, the Reynolds normal stress, the Reynolds shear stress and the pressure gradient.

(b) Pressure gradient in axial direction of a "stable" flame, an "unstable" flame and of a jet.

Figure 5.17: (a) Terms of the simplified momentum balance equation in axial direction. (b) Comparison of the adverse pressure gradient of a "stable" and an "unstable" flame and of a jet.

direction can be rewritten in the following way,

$$-\frac{1}{r^*}\frac{\partial\left(r^*\overline{u'^*v'^*}\right)}{\partial x^*} = -\frac{\overline{u'^*v'^*}}{r^*} - \frac{\partial\overline{u'^*v'^*}}{\partial r^*}. \tag{5.4}$$

The first term on the right hand side of equation 5.4 is zero. We are then left with the following equation,

$$\overline{u^*}\frac{\partial\overline{u^*}}{\partial x^*} = -\frac{\partial\overline{p^*}}{\partial x^*} - \frac{\partial\overline{u'^*u'^*}}{\partial x^*} - \frac{\partial\overline{u'^*v'^*}}{\partial r^*}. \tag{5.5}$$

In order to compute each of these terms form the experimental data a finite central difference scheme with second order accuracy has been used.

Figure 5.17a shows each of the four terms of equation 5.5. Notice that the contribution of both the Reynolds stresses is close to zero, so that the pressure gradient balances the advection term in axial direction. The important result is that the pressure gradient is positive until a distance of about 0.5 inner diameter from the burner outlet. As expected, solving the momentum equation in axial direction 2.23 for an isothermal jet, it can be seen that the pressure gradient is zero at tube burner outlet. Indeed, figure 5.17b shows the pressure gradients as determined for the isothermal (non reacting) jet and for two flames; one close to flashback conditions and named "unstable" and the other "stable". This clearly indicates that the adverse pressure gradient is due to combustion. Furthermore, the adverse pressure gradient compared in figure 5.17b results are relative to two flames which are characterized by same fuel composition (100% H_2) and equivalence ratio (ϕ = 0.8). The difference between these two flames is the Reynolds number, which in this case means bulk velocity since the same tube burner was employed. The "unstable" flame is very close to flashback and shows a significantly higher adverse pressure gradient. This might be due to the fact that the "unstable" flame has a larger cone angle (41.6° versus 39.6° of the stable flame). The larger cone angle then causes larger velocity magnitude increase across the flame front and so the adverse pressure gradient is higher. At the same time, larger cone angle means smaller distance between the burner outlet and the average flame front.

In order to further investigate what is the effect of the distance between the average flame front location and the burner outlet, the change of the adverse pressure gradient with the burner tube radius has been computed. To do so equation 5.3 has to be considered and it is necessary to carefully

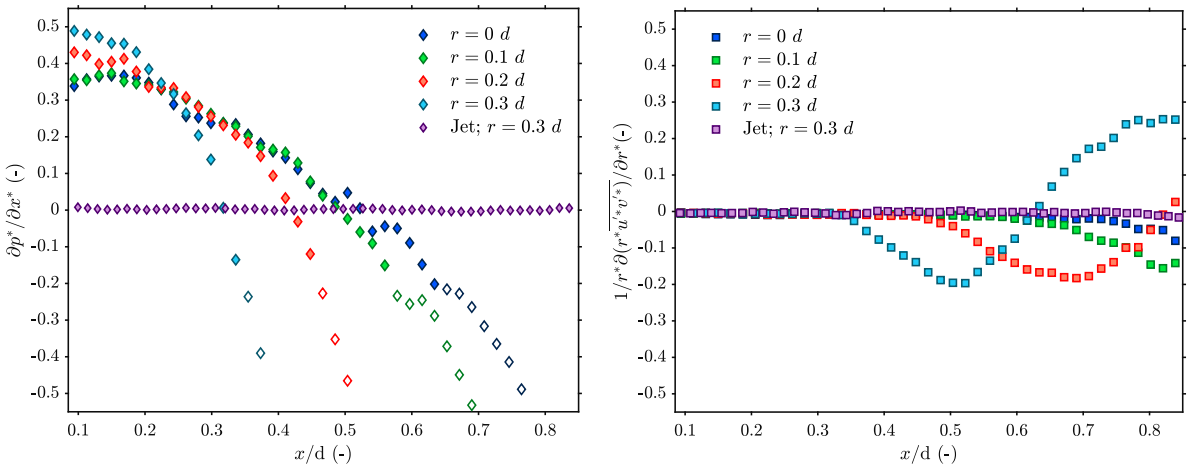

(a) Comparison of pressure gradient in axial direction of a flame. Each curve is computed at a different radial location.

(b) Change of the Reynolds shear stress gradient in radial direction as a function of the axial coordinate x, for a flame, at different radial locations, and for a jet flow at $r = 0.3d$.

Figure 5.18: (a) Comparison of pressure gradient in axial direction of a flame at different radial locations. (b) Change of the Reynolds shear stress gradient in radial direction as a function of the axial coordinate x, for a flame, at different radial locations, and for a jet flow at $r = 0.3d$.

define the region of the domain where equation 5.3 holds. In particular, in deriving equation 5.3 the viscous terms were neglected, which means that the equation does not hold in the near wall region. Also isothermal flow was assumed, which means that a sufficient distance has to be kept from the flame front in order to consider the density constant. The region of the flow field where the equation is valid has been determined by considering the Reynolds shear stress gradient in radial direction. The Reynolds shear stress gradient in radial direction contains information about both the turbulence fluctuations in radial and axial direction. Figure 5.18b shows the change of the Reynolds shear stress gradient in radial direction as a function of the axial coordinate x, for a flame, at different radial locations, and for a jet flow at $r = 0.3d$. As expected, closer we are to the burner wall and earlier the flame Reynolds shear stress deviates from the jet Reynolds shear stress. This is due to the fact that, moving in axial direction, the distance between the flame front average location and the burner outlet is smaller as we get closer to the rim. It is assumed that, if there are not turbulence fluctuations due to the flame front oscillations, the flow upstream the flame front can be considered to be isothermal and consequently the simplified momentum equation in axial direction 5.5 can be considered valid. From figure 5.18b then, equation 5.3 holds up to x/d $\simeq$ 0.35 at r = 0.3 d, up to x/d $\simeq$ 0.45 at r = 0.2 d, up to x/d $\simeq$ 0.6 at r = 0.1 d and up to x/d $\simeq$ 0.70 at r = 0 d.

The results in figure 5.18a show that closer we get to the wall and higher is the adverse pressure gradient. All the results in figure 5.18a belong to the same flame. As a consequence the difference in adverse pressure gradient moving in radial direction it is not related to a different average cone angle but has to depend on the distance between the average flame front location and the burner outlet. The highest value of the adverse pressure gradient is located close to the rim at r= 0.3 d, while the lowest value is found along the centerline. Previously, in section 3.3.1 it has been shown how the flame confinment affect the flashback propensity. In particular, Eichler et al. [17] shown the higher flashback propensity associated with confined flame. The results of figure 5.18a suggest that smaller is the distance from the tube outlet and the average flame front location and stronger is the effect of the burner walls that hampered the flow deflection leading to an even more higher retardation of the approaching flow.

In figures 5.12 and 5.14 the flashback was visualized for both the DNG flame and H_2 flame, it was seen that the flashback location is close to the tube inner wall, but outside the thin viscus layer. The velocity fluctuations in the buffer layer combined with the strong effect that the adverse pres-

sure gradient has on the incoming flow might explain why the transition mechanism occurs at this location.

5.5.3. Discussion on the flashback phenomenon

The instantaneous flame front location of a turbulent premixed flame changes in time as a function of the velocity fluctuations and of the local burning velocity. The velocity fluctuations can be related to the turbulent intensity of the flow while the local burning velocity depends on stretch. As a consequence of this two coupled effects, locally, the orientation of the flame front is sometimes perpendicular to the axial direction. In this case, the mixture experience the strongest acceleration through the flame front. The velocity magnitude increase across the flame front induces the adverse pressure gradient just upstream the flame front which leads to the flame-flow interaction. Indeed the flame deflects and retards the incoming flow, see figure 5.16. This interaction and dynamic of the flame has been observed experimentally for both stable and unstable flames, figures 4.4a and the left side of 5.16 show the instantaneous location of a stable and an unstable flame front, respectively. However, approaching the flashback onset, this interaction becomes stronger. The reason is that an unstable flame is closer to the tube burner outlet. The tube burner walls in fact, hampers flow deflection and retardation leading to an even stronger slowdown of the approaching flow. The effect of flow hampering can be captured by the value of the flame cone angle α_c. Indeed, bigger is α_c and closer is the average flame front to the tube burner outlet. Furthermore, for a give flame composition, α_c can be expressed as function of the bulk velocity. Thus, not only the lower bulk velocity induces bigger cone angle, it also cause the flame bulge to be advected more slowly allowing therefore a bigger growth. When these bulges grow close enough to tube burner wall, the hampering effect is sufficiently strong to induce flame flashback.

From the experimental evidence, see figure 5.12 and 5.14, the flashback phenomenon is qualitatively the same when lean hydrogen flame are considered. The reason why the event occurs more abruptly is that lean hydrogen flame are characterized by a negative Markstein length. This means that the flame stretch caused by the combined effect of turbulence fluctuations and adverse pressure gradient makes the hydrogen flame burning velocity higher, further enhancing the upstream propagation of the flame.

6

Conclusions and recommendations

In the present work, turbulent boundary layer flashback of premixed hydrogen/DNG air flames in tube burners has been investigated. The outcome of the results can be divided into three groups:

1. Flame regime maps.
2. Measurement of the time-average statistics of the reacting flow field.
3. Visualization of the flashback.

In the first group, flashback propensity for different mixture compositions and equivalence ratios has been studied experimentally at different burner conditions, e.g. cooled/uncooled.
In the second group, the statistics of premixed flames have been obtained by means of PIV and compared. These flames are characterized by different Reynolds numbers, equivalence ratios and hydrogen concentrations in the fuel.
Finally, flashback has been visualized with high spatial and temporal resolution PIV and Mie-scattering measurements.

Conclusions:

1. From the flame regime maps following conclusions can be drawn:
    - Higher hydrogen concentration in the fuel mixture leads to a higher flashback propensity.
    - The peak in flashback propensity is found at equivalence ratios where the burning flame speed is the highest.
    - The tip burner temperature strongly affects the flashback propensity. The uncooled burner configuration consistently shows the highest propensity for flashback.
2. For the time-average statistics of the reacting flow field, the effects of different Reynolds numbers, H_2 concentrations in the fuel and equivalence ratios have been compared.
    - When the same burner tube is employed and two different Reynolds number flames are compared, the actual parameter which makes the two Re different is the bulk velocity. At lower bulk velocity the flame is closer to flashback and is characterized by a bigger average cone angle. This leads to a higher acceleration of the flow across the flame front. The gas acceleration across the flame front is related to the hydrodynamic instability and causes a greater adverse pressure effect. Therefore, the flame characterized by a lower

Reynolds number shows stronger Reynolds normal stresses, both in the axial and radial direction. This result can also be related to the fact that this flame front average location, when compared to the flame with higher Reynolds number, is closer to the tube burner outlet.

- Comparing two flames, characterized by the same Reynolds number and equivalence ratio, but different H_2 concentration, is it seen that with increasing H_2 content the flame shows a stronger flame-flow interaction. Furthermore, it is noticed that the pure hydrogen flame shows a lower Reynolds normal stress in the axial direction. The explanation for this is the fact that hydrogen flames, because of the thermal diffusive instability, are characterized by sub-adiabatic conditions in the neighbourhood of the flame tip.
- When two flames, characterized by the same Reynolds number and H_2 concentration in the fuel but different equivalence ratio, are compared it can be seen that the one that has the higher equivalence ratio experiences a higher velocity magnitude increase across the flame front. This is due to the fact that the ratio between the density of burned and unburned gases is higher. This effect is observed when the Reynolds normal stresses in axial and radial direction are compared, however, from the comparison of the velocity magnitude increase of the two flame across the flame front no sharp difference can be seen. The explanation why no clear difference can be seen might be that the leaner flame suffers more the effects of the thermal-diffusive instability.

3. In the flashback visualization section a DNG-air and a H_2-air flame flashbacks have been compared.

   - The flashback mechanism occurring in the two flames is qualitatively the same.
   - The adverse pressure gradient is responsible for the flame flow interaction which causes the approaching flow to be deflected and retarded, eventually leading to flashback.
   - The strongest effect of the adverse pressure gradient is found to be when the flame front is locally perpendicular to the axial direction.
   - Because of the simultaneous effect of turbulence fluctuations and adverse pressure gradient flame bulges are created. When flashback onset conditions are approached these bulges occur closer to the burner outlet. When these bulges reach a location close enough to the burner outlet, the burner walls hamper the flow retardation and deflection. This allows the flame bulge to further travel upstream and to, eventually, cause flashback.
   - The main difference between the H_2 flame and DNG flame flashback is the duration of the phenomenon. It can be seen that flashback propensity of hydrogen flame is much stronger, in fact it takes approximately only one fifth of the time needed for the DNG flame.

Recommendation and further developments:

- It is recommanded to visualize the flashback phenomenon using a quartz tube in order to have insight on the flame propagation in the tube burner. This can be done by simply adding a quartz section of the same inner diameter to the existing tube burner.
- To better understand the effect of the adverse pressure gradient, it would be interesting to compute it for a confined burner geometry. This could be done by adding to the tube outlet a quartz tube with a larger inner diameter. Furthermore, a confined configuration is characterized by some recirculation zones at the location of change in cross sectional area. This would make the flame more stable allowing to investigate even leaner mixtures, where the effect of thermal-diffusive instability associated with hydrogen is expected to be stronger.

- Unburned gas preheating could be applied to compare the combined effect of thermal-diffusive and hydrodynamic instability. By doing so the burned/unburned density ratio of the gases could be decreased. This would reduce the hydrodynamic instability effect.
- A comparison between rich and lean H_2-air flames would allow assessing the effect of the Lewis number.
- Finally, for more extensive visualization of the flashback phenomenon tomographic PIV is required. In this way a clearer insight of the flashback phenomenon three-dimensionality could be obtained.

A

Dutch Natural Gas composition

Table A.1a shows the Dutch Natural Gas (DNG) and the air compositions, considered for the calculation of the mixuture properties and equivalence ratio. The same DNG composition used by Oldenhof et al. [44] has been adopted.

Mole percentage %	**Dutch Natural Gas**
CH_4	81.27
N_2	14.44
C_2H_6	3.73
Rest	0.6

(a) DNG composition in mole fraction

Mole percentage %	**Air**
N_2	78
O_2	21
Ar	1

(b) Air composition in mole fraction

Bibliography

[1] Bronkhorst High-Tech B.V. URL https://www.bronkhorst.co.uk/files/downloads/datasheets/el-flow/f-112ac.pdf.

[2] Carbon capture and storage (CCS). URL http://www.ccsassociation.org/what-is-ccs/.

[3] IEA (2019), "Renewables Information 2019". URL https://www.iea.org/reports/renewables-information-2019.

[4] Ad van Wijk. The Green Hydrogen Economy. Technical report, Noordelijke Innovation Board, 2018.

[5] G Baumgartner, L R Boeck, and T Sattelmayer. Investigation of the flame–flow interaction during flame flashback in a generic premixed combustion system by means of high-speed micro-PIV and micro-PLIF. In *16 th International Symposium on Flow Visualization*, number November 2015, 2014.

[6] Georg Baumgartner, Thomas Sattelmayer, and LR Boeck. Experimental Investigation of the Transition Mechanism From Stable Flame to Flashback in a Generic Premixed Combustion System With Image Velocimetry and Micro-PLIF Combined With Chemiluminescence Imaging. In David Wisler, editor, *ASME Turbo Expo 2015: Turbine Technical Conference and Exposition*, 2015. doi: 10.1115/1.4031227.

[7] M. Bellenoue, T. Kageyama, S. A. Labuda, and J. Sotton. Direct measuremrment of laminar flame quenching distance in a closed vessel. *Experimental Thermal and Fluid Science*, 27(3): 323–331, 2003. ISSN 08941777. doi: 10.1016/S0894-1777(02)00304-7.

[8] Ali Cemal Benim and Khawar J. Syed. *Flashback Mechanisms in Lean Premixed Gas Turbine Combustion*. 2014. ISBN 9780128008263. doi: 10.1016/C2013-0-18847-2.

[9] Loren E. Bollinger and Rudolph Edse. Effect of Burner-Tip Temperature on Flash Back of Turbulent Hydrogen-Oxygen Flames. *Industrial & Engineering Chemistry*, 48(4):802–807, 1956. ISSN 0019-7866. doi: 10.1021/ie50556a040.

[10] B. Boust, J. Sotton, S. A. Labuda, and M. Bellenoue. A thermal formulation for single-wall quenching of transient laminar flames. *Combustion and Flame*, 149(3):286–294, 2007. ISSN 00102180. doi: 10.1016/j.combustflame.2006.12.019.

[11] J F Foss C. Tropea, A. L. Yarin. *Springer handbook of experimental fluid mechanics*. 2007. ISBN 9783540251415.

[12] James F. Driscoll. Turbulent premixed combustion: Flamelet structure and its effect on turbulent burning velocities. *Progress in Energy and Combustion Science*, 34(1):91–134, 2008. ISSN 03601285. doi: 10.1016/j.pecs.2007.04.002.

[13] Zhixuan Duan, Brendan Shaffer, and Vincent McDonell. Study of Fuel Composition, Burner Material, and Tip Temperature Effects on Flashback of Enclosed Jet Flame. *Journal of Engineering for Gas Turbines and Power*, 135(12):121504, 2013. ISSN 0742-4795. doi: 10.1115/1.4025129.

[14] Rudolph Edse. Studies on burner flames of hydrogen-oxygen mixtures at high pressures. *Wright air development center technical report*, (52-9), 1952.

[15] Christian Eichler and Thomas Sattelmayer. Experiments on Flame Flashback in a Quasi-2D Turbulent Wall Boundary Layer for Premixed Methane-Hydrogen-Air Mixtures. *Journal of Engineering for Gas Turbines and Power*, 133(1):011503, 2010. ISSN 07424795. doi: 10.1115/1.4001985.

[16] Christian Eichler and Thomas Sattelmayer. Premixed flame flashback in wall boundary layers studied by long-distance micro-PIV. pages 347–360, 2011. doi: 10.1007/s00348-011-1226-8.

[17] Christian Eichler, Georg Baumgartner, and Thomas Sattelmayer. Experimental investigation of turbulent boundary layer flashback limits for premixed hydrogen-air flames confined in ducts. *Journal of Engineering for Gas Turbines and Power*, 134(1):1–8, 2012. ISSN 07424795. doi: 10.1115/1.4004149.

[18] B. Fine. The flashback of laminar and turbulent burner flames at reduced pressure. *Combustion and Flame*, 2(3):253–266, 1958. ISSN 00102180. doi: 10.1016/0010-2180(58)90046-4.

[19] Burton Fine. Further Expeiments on The Stability of Lamina and Turbulent Hydogen-Air Flames at Reduced Pessures. Technical report, NACA TN 3977, 1957.

[20] Burton Fine. Effect of Initial Temperature on Flash Back of Laminar and Turbulent Burner Flames. *Industrial & Engineering Chemistry*, 51(4):564–566, 1959. ISSN 0019-7866. doi: 10.1021/ie50592a044.

[21] Raymond Friedman and W. C. Johnston. The wall-quenching of laminar propane flames as a function of pressure, temperature, and air-fuel ratio. *Journal of Applied Physics*, 21(8):791–795, 1950. ISSN 00218979. doi: 10.1063/1.1699760.

[22] W. K. George. Processing of Random Signals. In *In Proceeding of the Dynamic Flow Conference*, pages 757–793, 1978.

[23] W G Gottenberg, D R Olson, and H W Best. Turbulence Combustion *. 1962.

[24] A. Gruber, J. H. Chen, D. Valiev, and C. K. Law. Direct numerical simulation of premixed flame boundary layer flashback in turbulent channel flow. *Journal of Fluid Mechanics*, 709:516–542, 2012. ISSN 00221120. doi: 10.1017/jfm.2012.345.

[25] Joseph Grumer and Margaret E. Harris. Temperature Dependence of Stability Limits of Burner Flames. *Industrial & Engineering Chemistry*, 46(11):2424–2430, 1954. ISSN 0019-7866. doi: 10.1021/ie50539a057.

[26] Hermann Schlicting. *Boundary-layer theory*. 7th edition, 1979.

[27] Vera Hoferichter. *Boundary Layer Flashback in Premixed Combustion Systems*. PhD thesis, 2017. URL `https://mediatum.ub.tum.de/doc/1336042/1336042.pdf`.

[28] Vera Hoferichter, Christoph Hirsch, and Thomas Sattelmayer. PREDICTION OF CONFINED FLAME FLASHBACK LIMITS USING BOUNDARY LAYER SEPARATION THEORY. In *Turbomachinery Technical Conference and Exposition*, pages 1–15, 2016.

[29] Vera Hoferichter, Christoph Hirsch, and Thomas Sattelmayer. Analytic prediction of unconfined boundary layer flashback limits in premixed hydrogen–air flames. *Combustion Theory and Modelling*, 21(3):382–418, 2017. ISSN 17413559. doi: 10.1080/13647830.2016.1240832. URL `http://dx.doi.org/10.1080/13647830.2016.1240832`.

[30] Zuohua Huang, Yong Zhang, Ke Zeng, Bing Liu, Qian Wang, and Deming Jiang. Measurements of laminar burning velocities for natural gas-hydrogen-air mixtures. *Combustion and Flame*, 146(1-2):302–311, 2006. ISSN 00102180. doi: 10.1016/j.combustflame.2006.03.003.

[31] Alireza Kalantari and Vincent McDonell. Boundary layer flashback of non-swirling premixed flames: Mechanisms, fundamental research, and recent advances. *Progress in Energy and Combustion Science*, 61:249–292, 2017. ISSN 03601285. doi: 10.1016/j.pecs.2017.03.001.

[32] Alireza Kalantari, Elliot Sullivan-Lewis, and Vincent McDonell. Flashback Propensity of Turbulent Hydrogen–Air Jet Flames at Gas Turbine Premixer Conditions. *Journal of Engineering for Gas Turbines and Power*, 138(6):061506, 2015. ISSN 0742-4795. doi: 10.1115/1.4031761.

[33] L. N. Khitrin, P. B. Moin, D. B. Smirnov, and V. U. Shevchuk. Peculiarities of laminar- and turbulent-flame flashbacks. *Symposium (International) on Combustion*, 10(1):1285–1291, 1965. ISSN 00820784. doi: 10.1016/S0082-0784(65)80263-6.

[34] C.K. Law. *Combustion Physics*. Cambridge University Press, Cambridge, 2006. doi: 10.1017/CBO9780511754517.

[35] Bernard Lewis and Guenther von Elbe. Stability and Structure of Burner Flames. *The Journal of Chemical Physics*, 11(2):75–97, 1943. ISSN 0021-9606. doi: 10.1063/1.1723808.

[36] T Lieuwen. *Unsteady Combustor Physics*. Cambridge University Press, Cambridge, 2012. doi: 10.1017/CBO9781139059961.

[37] Yu-Chun Lin, Salvatore Daniele, Peter Jansohn, and Konstantinos Boulouchos. Turbulent Flame Speed as an Indicator for Flashback Propensity of Hydrogen-Rich Fuel Gases. *Journal of Engineering for Gas Turbines and Power*, 135(11):111503, 2013. ISSN 0742-4795. doi: 10.1115/1.4025068.

[38] Moshe Matalon. Intrinsic Flame Instabilities in Premixed and Nonpremixed Combustion. *Annual Review of Fluid Mechanics*, 39(1):163–191, 2007. ISSN 0066-4189. doi: 10.1146/annurev.fluid.38.050304.092153.

[39] Moshe Matalon. COMBUSTION THEORY, 2017. URL `https://cefrc.princeton.edu/sites/cefrc/files/combustion-summer-school/lecture-notes/2017{_}Matalon{_}All{_}combined.pdf`.

[40] Philippe Mathieu. *The IPCC special report on carbon dioxide capture and storage*. 2006. ISBN 9608758424.

[41] L.A. Meyer and R.K. Pachauri. Climate Change 2014 Synthesis Report. Technical report, Intergovernmental Panel on Climate Change, Geneva, Switzerland, 2014.

[42] M. Mizomoto and H. Yoshida. Effects of Lewis number on the burning intensity of Bunsen flames. *Combustion and Flame*, 70(1):47–60, 1987. ISSN 00102180. doi: 10.1016/0010-2180(87)90158-1.

[43] Frans T.M. Nieuwstadt, Bendiks J. Boersma, and Jerry Westerweel. *Turbulence: Introduction to theory and applications of turbulent flows*. 2016. ISBN 9783319315997. doi: 10.1007/978-3-319-31599-7.

[44] E. Oldenhof, M. J. Tummers, E. H. van Veen, and D. J.E.M. Roekaerts. Ignition kernel formation and lift-off behaviour of jet-in-hot-coflow flames. *Combustion and Flame*, 157(6):1167–1178, 2010. ISSN 00102180. doi: 10.1016/j.combustflame.2010.01.002. URL `http://dx.doi.org/10.1016/j.combustflame.2010.01.002`.

[45] N. Peters. Combustion Theory, 2010.

[46] Philip A.E. Pogge von Strandmann, Kevin W. Burton, Sandra O. Snæbjörnsdóttir, Bergur Sigfússon, Edda S. Aradóttir, Ingvi Gunnarsson, Helgi A. Alfredsson, Kiflom G. Mesfin, Eric H. Oelkers, and Sigurður R. Gislason. Rapid CO 2 mineralisation into calcite at the CarbFix storage site quantified using calcium isotopes. *Nature Communications*, 10(1):1–7, 2019. ISSN 20411723. doi: 10.1038/s41467-019-10003-8.

[47] Stephen B. Pope. *Turbulent Flows*. Cambridge University Press, 2000. ISBN 9780511840531. doi: https://doi.org/10.1017/CBO9780511840531.

[48] P. Popp and M. Baum. Analysis of wall heat fluxes, reaction mechanisms, and unburnt hydrocarbons during the head-on quenching of a laminar methane flame. *Combustion and Flame*, 108(3):327–348, 1997. ISSN 00102180. doi: 10.1016/S0010-2180(96)00144-7.

[49] A. E. Potter and A. L. Berlad. A THERMAL EQUATION FOR FLAME QUENCHING. Technical report, 1955.

[50] R. J. Adrian and J. Westerweel. *Particle Image Velocimetry*. 2012. doi: 10.1017/S0001924000006734.

[51] G. A. Richards, M. M. McMillian, R. S. Gemmen, W. A. Rogers, and S. R. Cully. Issues for low-emission, fuel-flexible power systems. *Progress in Energy and Combustion Science*, 27(2):141–169, 2001. ISSN 03601285. doi: 10.1016/S0360-1285(00)00019-8.

[52] Antonio L. Sánchez and Forman A. Williams. Recent advances in understanding of flammability characteristics of hydrogen. *Progress in Energy and Combustion Science*, 41:1–55, 2014. ISSN 03601285. doi: 10.1016/j.pecs.2013.10.002. URL `http://dx.doi.org/10.1016/j.pecs.2013.10.002`.

[53] T Sattelmayer. Influence of the Combustor Aerodynamics on Combustion Instabilities From Equivalence. 125(January 2003):11–19, 2019. doi: 10.1115/1.1365159.

[54] Brendan Shaffer, Zhixuan Duan, and Vincent McDonell. Study of Fuel Composition Effects on Flashback Using a Confined Jet Flame Burner. *Journal of Engineering for Gas Turbines and Power*, 135(1):011502, 2012. ISSN 0742-4795. doi: 10.1115/1.4007345.

[55] Brendan Shaffer, Zhixuan Duan, Vincent McDonell, Georg Baumgartner, and Thomas Sattelmayer. Influence of Burner Material, Tip Temperature, and Geometrical Flame Configuration on Flashback Propensity of H 2 -Air Jet Flames . *Journal of Engineering for Gas Turbines and Power*, 136(2):021502, 2013. ISSN 0742-4795. doi: 10.1115/1.4025359.

[56] Shell. Sky scenario. URL `https://www.shell.com/energy-and-innovation/the-energy-future/scenarios/shell-scenario-sky{%}0A`.

[57] E. F.C. Somerscales. *Fluid dynamics*, volume 18, chapte. 1981. ISBN 0124759602. doi: 10.1201/9781315215228-11.

[58] J. Sotton, B. Boust, S. A. Labuda, and M. Bellenoue. Head-on quenching of transient laminar flame: Heat flux and quenching distance measurements. *Combustion Science and Technology*, 177(7):1305–1322, 2005. ISSN 00102202. doi: 10.1080/00102200590950485.

[59] L. Tay-Wo-Chong, T. Komarek, M. Zellhuber, J. Lenz, C. Hirsch, and W. Polifke. Influence of Strain and Heat loss on Flame Stabilization in a Non-Adiabatic Combustor. *European Combustion Meeting*, pages 1–6, 2009.

[60] Mark J. Tummers, Jeroen Jacobse, and Sebastiaan G.J. Voorbrood. Turbulent flow in the near field of a round impinging jet. *International Journal of Heat and Mass Transfer*, 54(23-24): 4939–4948, 2011. ISSN 00179310. doi: 10.1016/j.ijheatmasstransfer.2011.07.007. URL `http://dx.doi.org/10.1016/j.ijheatmasstransfer.2011.07.007`.

[61] John A. Turner. Sustainable Hydrogen Production. *Sustainable Hydrogen Production*, 305 (August):1–479, 2016. doi: 10.1016/b978-0-444-64203-5.00001-0.

[62] J. Warnatz, U. Maas, and R. W. Dibble. *Combustion: Physical and Chemical Fundamentals, Modeling and Simulation, Experiments, Pollutant Formation.* Springer, 2nd edition, 1999.

[63] Jerry Westerweel and Fulvio Scarano. Universal outlier detection for PIV data. *Experiments in Fluids*, 39(6):1096–1100, 2005. ISSN 07234864. doi: 10.1007/s00348-005-0016-6.

[64] Frank M White and I Corfield. *Viscous Fluid Flow*. New York, 3 edition, 2006.

[65] Kurt Wohl. Quenching, flash-back, blow-off- theory and experiments. *Symposium (International) on Combustion*, 4(1):68–89, 1953.